Elucidating the Mechanosensitive Properties of Fibronectin Using Surface-Initiated Assembly

Submitted in partial fulfillment of the requirements for

the degree of

Doctor of Philosophy

in

Biomedical Engineering

John M. Szymanski

B.S., Materials Science & Engineering, Johns Hopkins University

Carnegie Mellon University
Pittsburgh, PA

September, 2015

ACKNOWLEDGMENTS

The past 5 years have been a time of great personal and academic growth and it would not have been possible without the help and support of many. Firstly, I would like to sincerely thank my advisor, Dr. Adam Feinberg. By setting and maintaining high expectations and standards, I have developed into the scientist that I am today. I am grateful for the opportunity to engage in a diverse set of intellectually challenging projects and for the opportunity to present my work at many conferences. Joining the Regenerative Biomaterials and Therapeutics Group led by Dr. Feinberg in its infancy was the best professional decision I have made to date.

I also want to thank current and past members of the Regenerative Biomaterials and Therapeutics Group. Specifically, I want to acknowledge Quentin Jallerat and Dr. Yan Sun for their help as co-first authors in the development of the Patterning-on-Topography method. Additionally, I would like to acknowledge Dr. Rachelle Palchesko, Amrita Sahu, and Mengchen Ba who worked with me as co-first authors on two different manuscripts that are not discussed in this thesis. I also want to acknowledge Kairui Zhang who helped immensely in the development the fibronectin fiber straining technique discussed in Chapter 3. Finally, I want to thank the other group members, specifically TJ Hinton, Rebecca Duffy, Ivan Batalov, Prarthana Patil, and Alkis Tsamis for the constant support and fruitful discussions.

I would like to thank my committee members—Dr. Yu-Li Wang, Dr. Kris Dahl, and Dr. Lance Davidson—for taking the time out of their busy schedule to be on my thesis committee. I am particularly grateful for their valuable feedback throughout my graduate career.

My funding sources have made this work possible and for that I am truly grateful. The Biomechanics in Regenerative Medicine NIH T32 Training Grant led by Dr. Savio-Woo and Dr. James Antaki, has not only funded my work but, through monthly meetings, exposed me to the broader field of biomechanics outside of my own research. I would also like to personally thank Diann DeCenzo who was responsible for organizing all of the BiRM-related activities. Additionally, I am grateful for receiving the John and Claire Bertucci Graduate Fellowship, which has provided additional funding for my thesis

research. Lastly, I would like to acknowledge the NIH Director's New Innovator Award which was awarded to Prof. Feinberg and has provided support for the work presented here.

I want to acknowledge all of my friends and family as well as my graduate student colleagues in the Department of Biomedical Engineering. Their constant support has helped maintain a positive morale throughout this entire process.

I cannot thank my parents—John, Sr and Helen Szymanski—enough for the endless love, support, and encouragement not just in graduate school but throughout my life. The sacrifices they have made—whether it be driving all over New England every weekend for baseball tournaments or simply being available to talk on the phone at any hour of the day—have played a major role in becoming who I am today and I hope to make them proud with this work.

Finally, I want to thank my fiancée, Dr. Natasha Loghmanpour. She has been a constant source of support, encouragement, and motivation. I am significantly happier when I am with her and I do believe that trickles down into every other aspect of my life, including research.

ABSTRACT

The extracellular matrix (ECM) plays an integral role in many biological processes such as embryonic development, wound healing, homeostasis, and even disease progression. While the physical and chemical properties of the ECM are known to influence cell behavior and modulate gene expression, emerging evidence suggests that ECM proteins also have mechanosensitive properties. Specifically, the ECM protein fibronectin (FN) undergoes strain-dependent conformational changes that modulate it's self-assembly as well as binding to a number of ligands including transmembrane integrin receptors, growth factors, and other ECM proteins. The goal of this thesis is to investigate how strain affects the structural and biological properties of FN nanofibers assembled through a surface-initiated assembly technique (SIA).

First, atomic force microscopy (AFM) was used to morphometrically track the micro- and nanoscale structures of FN nanofibers during large deformations associated with the SIA process. While there were significant changes in length, width, and thickness during this process, the nanofiber volume remained constant suggesting that they behaved as incompressible materials over these strain ranges. In addition, AFM at high resolution revealed that there were distinct morphological differences within the nanostructure of FN nanofibers in pre- and post-release states. Next, the FN nanofibers were uniaxially strained to track how the structural morphology of FN nanofibers from fully contracted to highly strained states. The structure of fully contracted FN nanofibers was predominantly comprised of large, isotropically-oriented nodules that became progressively smaller with increasing strain. At maximum strain, the nanostructure was highly aligned and contained small nodules in a 'beads-on-a-string' arrangement. Finally, a Patterning-on-Topography (PoT) method was developed to investigate how FN strain affects C2C12 adhesion and α_5 integrin activation. Using this approach, it was found that while a decrease in FN density likely promoted less cell spreading and α_5 integrin expression, the observed behaviors were further enhanced by FN in a highly strained state. Collectively, the work presented in this thesis demonstrates how the SIA and PoT can be leveraged to study the mechanosensitive properties of

FN to ultimately progress our knowledge for how cells are capable of dynamically manipulating and responding to the ECM particularly during tissue morphogenesis and disease progression.

TABLE OF CONTENTS

LIST OF FIGURES

CHAPTER 1:

Introduction

1.1. Introduction and Motivation

The extracellular matrix (ECM) has long been recognized for its role in providing structural support to cells residing within our tissues. However, it has become increasingly clear that chemical composition and physical properties of the ECM play a multifunctional role in embryonic development[1-6], homeostasis[7], and in numerous diseases such as cancer[8,9] and fibrosis[10,11]. Cell adhesion to the ECM controls the bi-directional flow of information that ultimately plays a role in cell migration, proliferation, differentiation, and apoptosis[12-14]. Understanding the nature of these cell-ECM interactions and, more precisely, how researchers can leverage the chemical and physical properties of the ECM to elicit specific cellular responses is paramount towards the development of new therapeutic strategies to treat disease as well as foster the growth of new tissue.

While the chemical properties of many ECM components have been well studied, the physical properties of the extracellular environment can also have a pronounced effect on cell behavior and gene expression. For example, modulation of the rigidity[15,16], topography[17,18], and geometry[19-21] of the cell microenvironment can influence cell adhesion[20-22], migration[23-25], and differentiation[15,26,27]. By understanding the relationship between cells and these physical properties, researchers have been able to make significant progress in the development of engineered tissues as well as enhance our understanding of disease progression.

The cells within our tissues *in vivo* are rarely within a static microenvironment. One mechanism to accommodate for a dynamically changing microenvironment has been through the use of mechanosensitive proteins that are present both within and outside the cell. These mechanosensory units allow cells to transduce a variety of mechanical forces into biochemical signals. Perhaps the best-characterized of these systems are mechanosensitive ion channels in the cell membrane[28,29]. Forces derived from a variety of inputs such as osmotic pressure gradients and cell swelling promote the activation of these ion channels. Inside the cell, the focal adhesion proteins vinculin and talin have both been shown to exhibit mechanosensitive properties during the assembly and maturation of focal

adhesions[30,31]. Finally, the extracellular matrix protein, fibronectin (FN), is a large multimodular protein that undergoes force-induced conformational changes to regulate self-assembly[32-35], integrin receptor interactions[36-39], growth factor binding[40], collagen interactions[41], and bacterial adhesion[42]. Since FN is a major component of the ECM during critical biological processes such as embryonic development[43,44], wound healing[45-47], and disease progression[48-50], understanding the mechanosensitive properties is critical for elucidating the role FN for the formation of healthy tissue as well as the progression of diseased tissue. The purpose of this chapter is to introduce our current understanding of the FN structure, its mechanosensitive properties, and how researchers are using a variety of techniques to study these properties in cell culture and in cell-free environments.

1.2. FN Structure

FN is a large, multimodular, disulfide-linked ECM glycoprotein that exists in the plasma and is assembled into a fibrillar matrix in many tissues throughout all stages of life. FN is composed of three different types of modular domains termed FN type I, II, and III that are all β-sheet motifs (Fig. 1.1a). The 15 FN III domains that comprise the central region of monomeric FN (Fig. 1.b) are unique in that they lack an intramodule disulfide bond making them mechanically weaker than the FN I and FN II domains [51,52]. Therefore, through the application of cell-generated forces, the FN III domains are capable of unfolding into a number of intermediate conformations[53]. Although the 15 different FN III domains all have similar seven-stranded β-sheet structures, there is high variability in their amino acid sequences. Steered molecular dynamics simulations have demonstrated that the large variably in amino acid sequences establishes a hierarchy of FN III domain stability[54].

Due to alternative splicing during transcription, up to 20 different FN isoforms can exist in humans that are separated into two major classes: plasma fibronectin (pFN) and cellular fibronectin (cFN)[55-57]. pFN is produced by hepatocytes in the liver[58] and is eventually secreted into the bloodstream

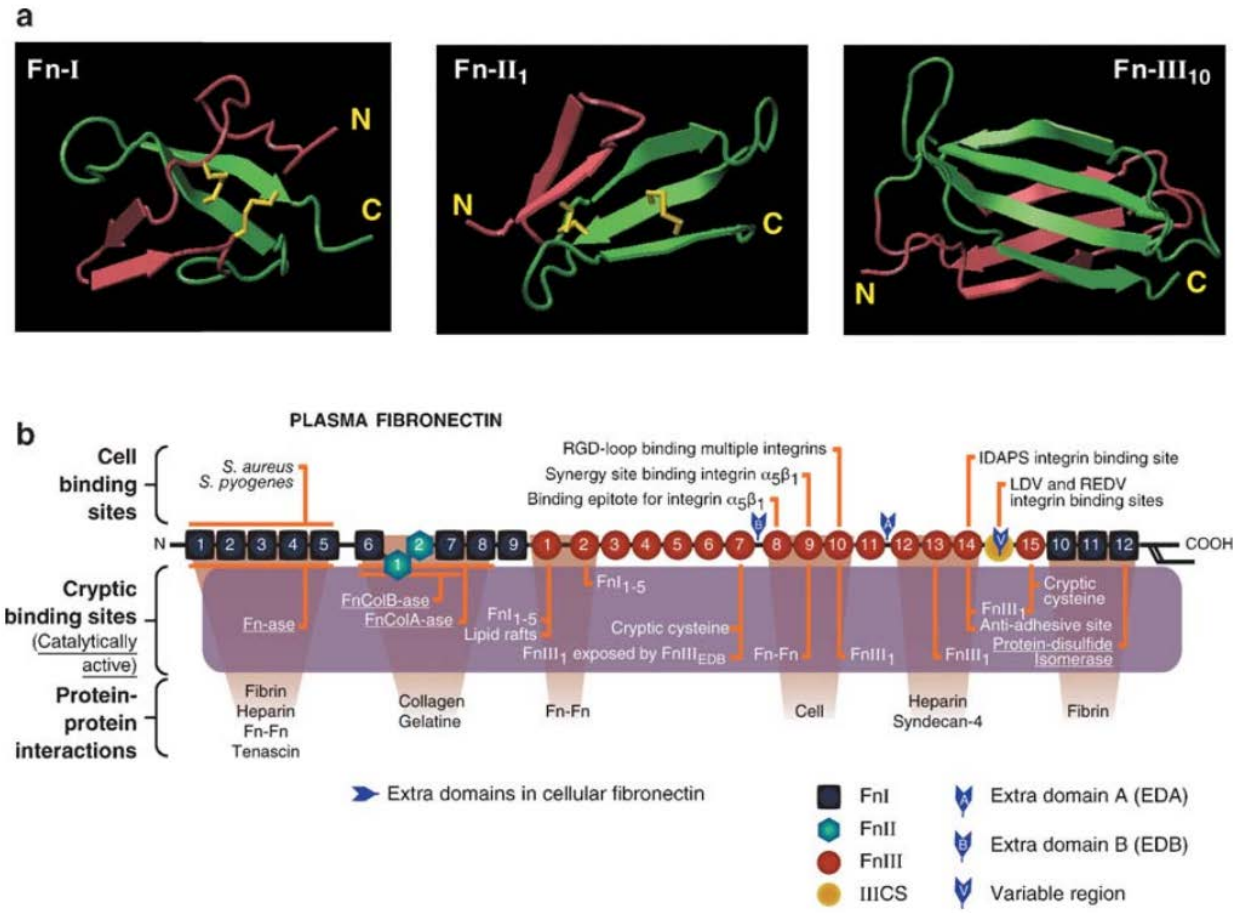

Fig. 1.1. The modular structure of FN. (a) Representative crystal structures of the FN I, FN II, and FN III domains. Each of the domains has high β-sheet contain (arrows) and only the FN III domains lack intramodule disulfide bonds (yellow). (b) The monomeric structure of pFN. Select sites for cell bind and FN-ECM interactions are shown as well as some of the identified cryptic binding sites. The blue arrows indicate where the extra domain B (between FN III_{7-8}), extra domain A (between FN III_{11-12}), and variable region (between FN III_{14-15}) would be located in other FN isoforms. Adapted from Vogel, 2006[59].

where it circulates at a relatively high concentration of ~300 μg/mL[60,61]. pFN has been suggested to play an important role in the coagulation cascade where it has been shown to stabilize platelet aggregates following vascular injury[62,63]. While pFN exists mostly in the plasma, recent evidence has shown that a significant fraction of pFN is also found within the fibrillar ECM of tissues[64]. cFN differs from pFN in that these isoforms can have none, one, or both extra FN III domains termed extra domain A (EDA) and extra domain B (EDB). While it has been suggested that the inclusion of these extra domains may affect cell adhesion[65,66], the complete role of these extra domains in tissues is not well understood. For example,

FN containing EDA and EDB variants are highly expressed around the vasculature during embryogenesis[67,68], yet mice lacking either EDA or EDB develop normally and are fertile[65,69]. In addition to being highly expressed around the vasculature during embryonic development, FN containing EDA and EDB has also been found at sites of inflammation, injury, and tumors[69-71]. Finally, in addition to the EDA and EDB domains, FN also contains an alternatively spliced variable (V) region that can be included in both pFN and cFN. In humans, there are five splice variants that differ in the amino acid length of the V region, namely: V_0, V_{64}, V_{89}, V_{95}, and V_{120}, where the subscript refers to the amino acid length. The V region has been shown to play a role in cell adhesion[72] and it affects FN dimer secretion, where FN dimers lacking a V region on both monomeric arms are degraded inside the cell[73]. Altogether, through structural and mechanical hierarchies established within FN via amino acid sequence variability and the inclusion of alternatively spliced domains underscores the importance of FN in a multitude of critical biological processes from vasculature formation during embryonic development to blood clotting. While new functions of FN continue to emerge, it is clear that a complete understanding of FN and its functions *in vivo* is still lacking.

1.3. Cell-FN Interactions

FN is well known for containing binding domains to a number of ligands including integrin[12,13,44,74,75] and syndecan receptors[76,77] on the cell membrane, growth factors[40,46,47,78,79], and ECM proteins such as collagen[34,41], fibrin[80], and heparin[81,82] (Fig. 1.1b). Probably the most well-known binding site associated with FN is the arginine-glycine-aspartic acid (RGD) tripeptide on the FN III_{10} domain. The RGD tripeptide is universally used for its ability to trigger cell adhesion via heterodimer integrin receptors on the cell membrane. A number of cell surface integrin receptors are capable of binding to the RGD motif on FN including $\alpha_v\beta_1$, $\alpha_v\beta_3$, $\alpha_v\beta_5$, $\alpha_v\beta_6$, $\alpha_v\beta_6$, and $\alpha_9\beta_1$[44,83]. In addition to these integrin receptors, the major FN-binding integrin is $\alpha_5\beta_1$, requires a neighboring synergy site on the FN III_9 domain for a high affinity adhesion[84-86]. Steered molecular dynamics simulations have demonstrated that force induced conformational changes in FN are capable of decoupling the synergy-RGD sites thereby preventing cell

adhesion via the $\alpha_5\beta_1$ integrin receptors[36]. Importantly, the use of different integrin receptors by cells has been shown to affect downstream FN fibrillogenesis processes[33,75], cytoskeletal assembly[12,87], and even proliferation and differentiation[39,88]. For example, Schiller et al was able to assign differences in the morphology of cellular focal adhesions, their signaling capacity, and the protein composition of their adhesomes to the activity of different integrin classes[87]. Additionally, fibroblasts expressing only α_v-class integrins were less spread and migrated slower than fibroblasts expressing only β_1-class integrins or both α_v and β_1-class integrins. In another study, Pankov et al demonstrated that while $\alpha_v\beta_3$ integrin receptors remain located within focal contacts and focal adhesions, the $\alpha_5\beta_1$ integrin receptors were observed to translocate and coincide with the formation of fibrillar adhesions. The translocation of the $\alpha_5\beta_1$ integrin receptors was also proposed to promote initial FN fibrillogenesis[75]. While integrin receptors are considered the dominant receptor for FN interactions, several studies have begun to elucidate the role of syndecan transmembrane heparin sulfate proteoglycans in FN-mediated cell adhesion, focal adhesion assembly, and FN matrix assembly[76,77,89,90]. Briefly, syndecan-4 and syndecen-2 trigger focal adhesion assembly and FN matrix assembly by activating focal adhesion kinase and a number of small GTPases such as RhoA[76,91]. Thus, it is clear that cells are capable of interacting with FN through a variety of receptors and specific receptors have been identified as critical components of signaling processes that regulate FN fibrillogenesis, proliferation, and differentiation.

1.4. FN Fiber Assembly in Tissues

Many cell types are capable of synthesizing and assembling a FN matrix in their microenvironment and insights into how cells are able to bind soluble FN dimers and assemble them into an insoluble, fibrillar form on the order of 5-1000 nm[92-94] has allowed researchers to further understand the dynamic properties of FN. Key steps in the FN fibrillogenesis (polymerization) process have been defined as: (1) cell binding to dimeric FN, (2) FN dimer extension and clustering, and (3) maturation into deoxycholate (DOC) detergent insoluble fibers through the establishment of sufficient FN-FN interactions (Fig. 1.2). As previously mentioned, FN is initially secreted as a disulfide linked dimer and this dimeric

form has been found to be essential for fibrillogenesis as monomeric FN was not able to support FN fiber formation[95,96]. The dimeric structure of FN is compact and stabilized through long range interactions between the FN III_{2-3} and FN III_{12-14} domains[97]. These long range interactions prevent the spontaneous assembly of FN, which would have catastrophic effects given pFN circulates in the bloodstream at relatively high concentrations. FN matrix assembly is therefore initiated when the FN dimers bind to the $\alpha_5\beta_1$ integrins via the synergy and RGD sites on the FN III_{9-10} domains[86,98](Fig. 1.2a). Experiments blocking integrin-FN interactions, primarily through the RGD site, resulted in the prevention of FN fibril formation[99,100]. Additionally, while $\alpha_5\beta_1$ integrins, through their interactions with the RGD and synergy sites, play a dominant role in FN fiber formation[101], loss of $\alpha_5\beta_1$ expression both in cell culture and in mice did not result in a loss of FN matrix assembly[32,102,103]. Instead, it was suggested that the α_v-class of integrin receptors are capable of initiating FN fiber assembly although these FN fibers were much shorter and thicker than FN fibers assembled through FN- $\alpha_5\beta_1$ integrin interactions[102,104].

Integrin engagement subsequently triggers cell-mediated contractility (Fig. 1.2b) resulting in the progressive unfolding of the FN dimers into an extended, fibrillar state[105-107]. The necessity for the application of cell-mediated contractile forces to unfold FN dimers has been demonstrated in multiple studies where FN matrix assembly was prevented through the disruption of cell-mediated contractile forces[32,108,109]. Moreover, integrin engagement with FN also promotes integrin clustering (Fig. 1.2c) thereby bringing many unfolded FN dimers into close proximity. Since many self-assembly sites within FN dimers have been found to be dependent on conformational changes, cell-mediated contractility forces unfold the FN dimers to expose these sites and integrin-mediated clustering of FN dimers ensure sufficient FN-FN interactions for the assembly of insoluble FN fibers (Fig. 1.2d). FN fibrils are initially soluble in deoxycholate (DOC) detergent[110], but through the continued deposition of FN dimers, the FN fibers thicken, elongate, and, through the formation of many strong, noncovalent FN-FN interactions[111], are eventually irreversibly converted into DOC insoluble fibers[60,112]. While the physiological significance of DOC soluble and DOC-insoluble forms of FN fibers is still under investigation, these two different

forms likely contribute to the complex chemical and physical properties of the ECM in both healthy and diseased tissue.

1.5. Fibronectin Fibrillogenesis in a Cell-Free Environment

Through studies involving cell-mediated FN matrix assembly, researchers have identified that inducing conformational changes that expose cryptic self-assembly sites is critical to enabling fibrillogenesis in a cell-free environment. This is important because studying the properties of FN in the ECM of tissues and cell culture can be challenging because there is a heterogeneous distribution in the size and density of FN fibers and they are typically integrated into an ECM that contains many other components. Early work demonstrated that fibrillogenesis is possible through the use of denaturants and reducing agents[113,114]. More recently, fibrillogenesis was demonstrated using force-based assembly techniques where the mechanical tension generated underneath expanding dipalmitoyl phosphatidylcholine lipid monolayers[107] and by dewetting superhydrophobic surfaces[115,116] was sufficient to promote FN fiber assembly. Similarly, the shear forces associated with drawing a sharp tip out of a concentrated FN solution[41,42,117-120] were also found to trigger FN fiber assembly (Fig. 1.4).

Instead of using force to induce FN conformational unfolding, researchers have also utilized protein-surface interactions. This material driven assembly approach has been demonstrated using a number of different materials, including polysulfonate, poly(ethyl acrylate) (PEA), and surfaces with grafted hydroxyl, methyl, and amine groups[38,39,88,121,122]. The interesting feature of this technique is that FN fibrils adopt different conformations depending on the hydrophobicity and charge of the surfaces. However, the fibrils formed using material-driven approaches are permanently bound to the surface. Based on the key parameters of the material-driven techniques was the development of surface-initiated assembly (SIA) technique (Fig. 1.3) where the FN nanofibers were capable of being released from their substrate[123,124]. In this method, protein-surface interactions trigger the unfolding of FN dimers onto topographically patterned PDMS stamps (Fig. 1.3a-c) and, unlike other material-driven techniques, the

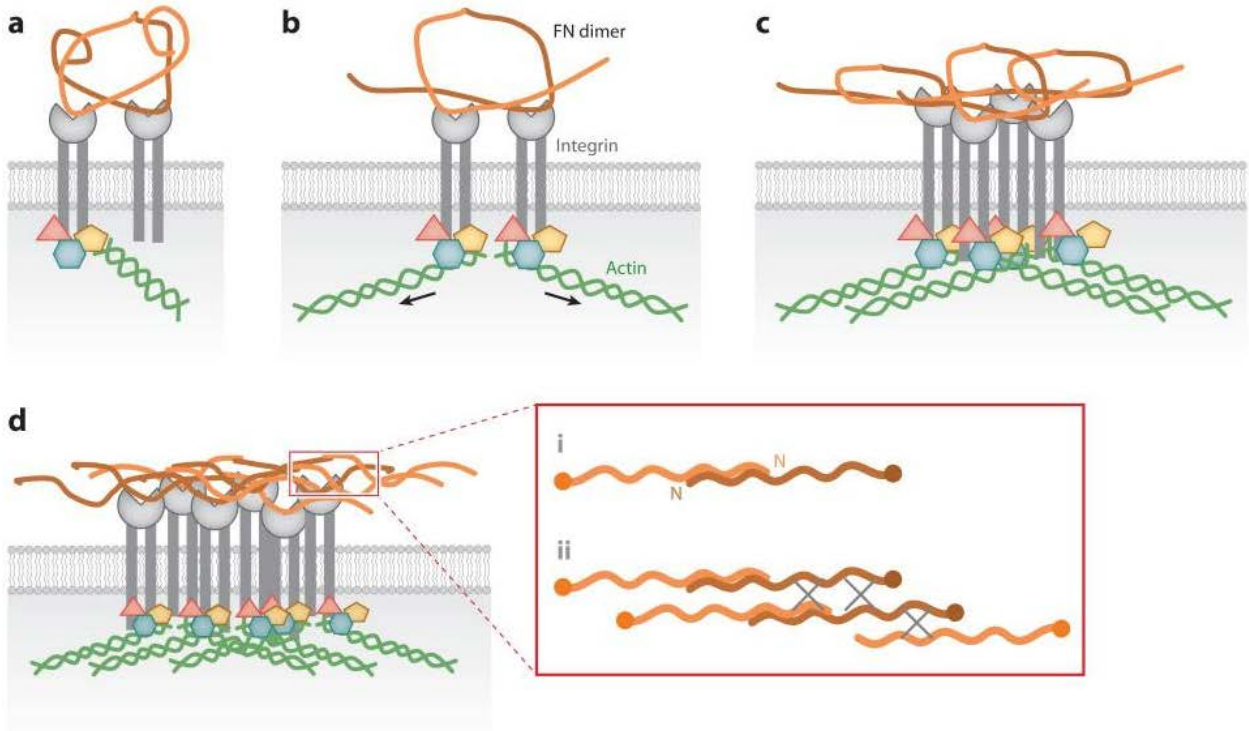

Figure 1.2. The FN matrix assembly process. (a) Initiation of FN matrix assembly is triggered by the binding of FN in a dimeric, compact form to mainly $\alpha_5\beta_1$ integrin receptors. Each monomeric arm of the FN dimer is color coded with a different shade of orange. Integrin engagement triggers (b) actin-mediated contractile forces and (c) integrin clustering to bring more FN dimers into close proximity as they are progressively unfolded. (d) Integrin clustering and exposed cryptic self-assembly sites promote FN-FN interactions and eventually, formation of a DOC-insoluble FN fiber. Gray "X" indicates interactions between adjacent, unfolded FN dimers. Adapted from Singh et al, 2010[35].

FN dimers are transferred in a partially unfolded state to a dissolvable poly(N-isopropylacrylamide) (PIPAAm) substrate (Fig. 1.3d-f). Triggering the dissolution of PIPAAm nondestructively releases assembled, insoluble FN fibers from the surface and into solution where they can be manipulated and mechanically, structurally, and biologically characterized (Fig. 1.3g).

Altogether, this toolbox of strategies to synthetically assemble and manipulate micro- and nanoscale FN fibers has allowed researchers to begin to identify key structural, mechanical, and biological properties of FN. As these techniques continue to develop we envision the ability to better understand how cells can mechanically manipulate FN fibers to expose cryptic sites and alter their bioactivity.

1.6. Studying the Mechanosensitive Properties of FN

Using the approaches described above, significant progress has been made in elucidating the structural, mechanical, and biological properties of FN both in cell-free environments and in cell-generated FN matrices. Using force-based assembly techniques, Vogel and coworkers pulled micrometer size FN fibers out of a concentrated FN solution and deposited them onto stretchable[120] and microfabricated surfaces[119] to measure their mechanical properties (Fig. 1.4a-c). Using stretchable substrates, the FN fibers could withstand 5- to 6-fold extensions[120]. However, when deposited across microfabricated channels and strained using a MEMS tip, the FN fibers could withstand up to 8.6-fold extensions (760% strain) demonstrating the remarkable extensibility of FN fibers (Fig. 1.4d-g). Because the MEMS tip could measure applied forces, it was also shown that the stress-strain behavior of FN fibers is highly nonlinear[119]. Furthermore, given sufficient time between consecutive strains, the FN fibers were found to completely recover their mechanical properties on initial strains up to 200%. In addition to measuring the mechanical properties, these force induced assembly approaches also permitted the investigation into how strain was affecting the bioactivity of FN fibers. Specifically, it was found that strain modulates the binding activity of bacterial adhesion peptides[42], the exposure of cryptic binding sites[119], sites for collagen interactions[41].

The mechanical properties were also studied using calibrated microneedles to apply uniaxial loading to FN fibers prepared using SIA[125]. In this study, it was confirmed that FN fibers can support over 8-fold extensions. Using 2-state and 8-chain network models it was further shown that FN fibers undergo three strain-dependent regimes that correlate to conformational unfolding, domain unfolding, and strain stiffening. Importantly, the FN fibers no longer exhibited elastic behavior beyond the conformational unfolding regime (up to 2-fold extensions) which is lower than what was observed using force-based assembly techniques in combination with MEMS tips[119]. These results suggest that while FN is highly extensible, different fabrication strategies may lead to the FN fibers with different mechanical and possibly structural properties.

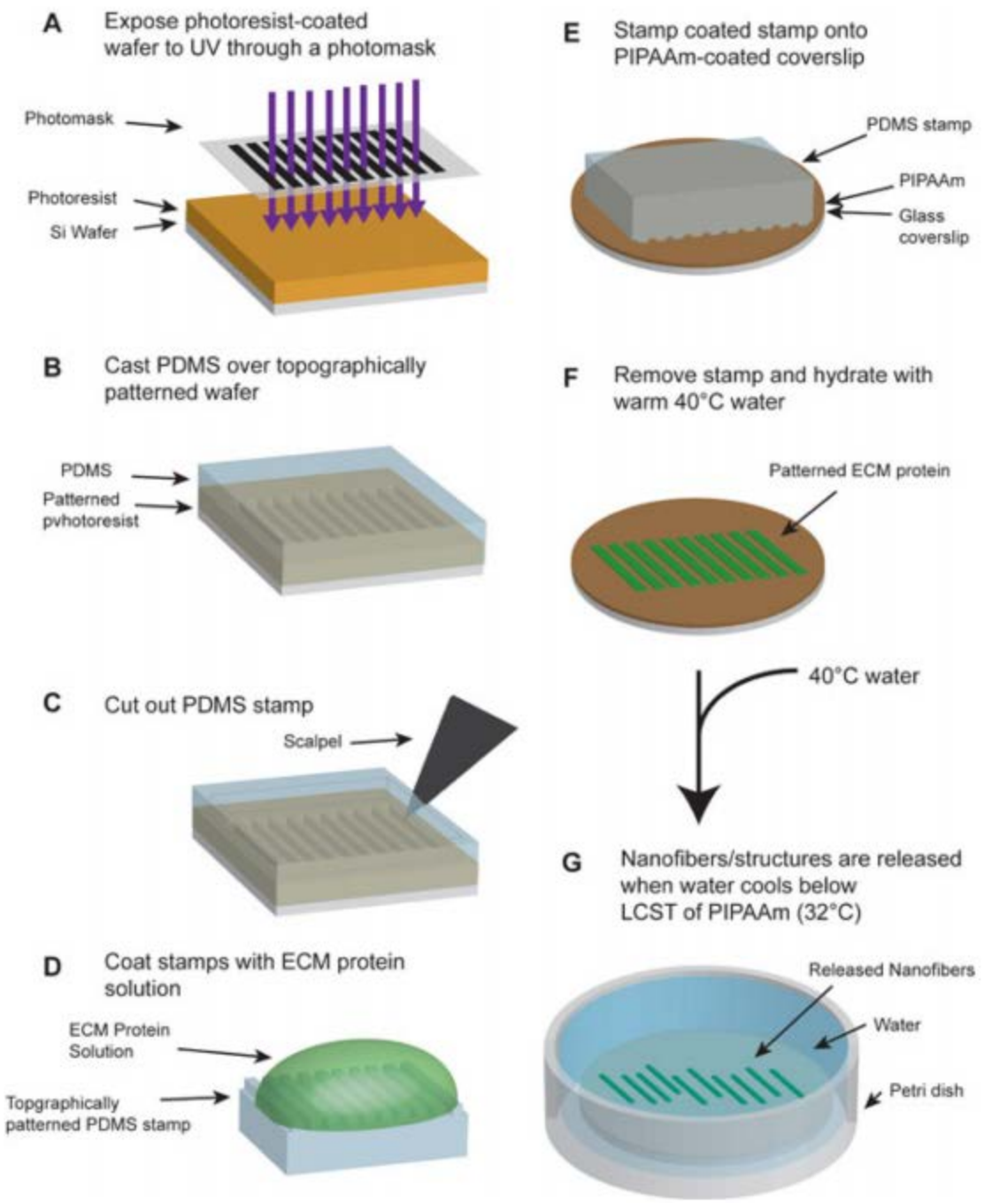

Fig. 1.3. **The surface-initiated assembly process**. (A) A silicon wafer is spincoated with SU8 negative photoresist and exposed to UV light through a photomask. Non-exposed regions are developed away leaving a topographically patterned master mold. (B) PDMS prepolymer is cast over the master mold, cured and (C) cut out of the master mold. (D) The stamp can then be incubated with an ECM protein (FN) solution, rinsed, dried, and then (E) brought into conformal contact with a PIPAAm-coated coverslip. (F) The stamp is removed and (G) the coverslip is hydrated with 40 °C distilled water and cooled below the lower critical solution temperature of PIPAAm (~32°C). Transition below the LCST triggers the dissolution of PIPAAm and release of assembled, insoluble FN nanofibers and nanostructures into solution. Adapted from Szymanski et al, 2014[124].

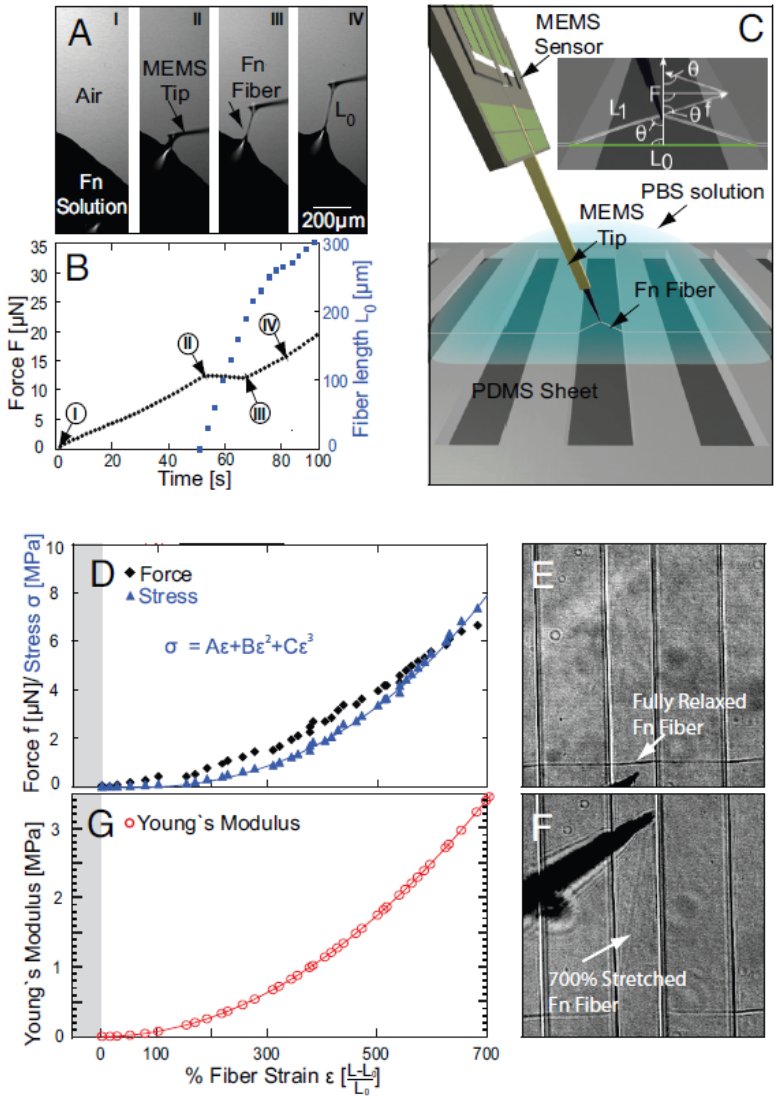

Fig. 1.4. Force induced assembly of micrometer scale FN fibers. (A) A MEMS force sensing tip was brought into contact with a concentrated FN solution and pulled back with a constant speed of 8 µm/s. (B) The pullout force and the fiber contour length were monitored as the tip was retracted from the FN solution. (C) The FN fibers were deposited across microfabricated trenches in a PDMS sheet. Following rehydration in PBS, the FN fibers were mechanically stretched in the axis of the trenches. (D) The force-strain and stress-strain curves were generated based on the MEMS force sensor, the assumption of a constant cross-sectional area and optical images of the FN fibers in a (E) relaxed state and in a (F) strained state. The Young's modulus was determined based on the slope of the stress-strain curve. Adapted from Klotzsch et al, 2009[119].

The mechanical properties of individual FN III domains were also studied using atomic force microscopy (AFM)[126-128]. This was accomplished by grafting engineered polypeptides containing different FN III domains to a gold substrate. The polypeptides were "grabbed" by an AFM tip through adsorption and stretched for distances up to several hundred nanometers. The resulting force-extension curves enabled the elucidation of the forces required to unfold each FN III domain. Specifically, the weakest FN III domain (FN III_{10}) was found to unfold with forces as low as ~40 pN whereas the most stable FN III domains (FN III_1 and FN III_2) were found to unfold after the application of 200 pN. Molecular dynamics simulations have suggested that the mechanical mismatch between FN III domains is likely due to high amino acid sequence variability[36]. These results have suggested that this mechanical hierarchy of the different FN III domains provides a mechanism for which cells can control the exposure of different cryptic binding sites.

Material-driven fibrillogenesis techniques have enabled the structural characterization of the nanoscale FN fibrils that form on different surface chemistries[122,129-131] and ultimately how differences in structural conformation influence cell adhesion, particularly via integrin-FN interactions, and differentiation[37-39,121,131]. For example, Nelea et al demonstrated the negatively charged polysulfonate surfaces are capable of disrupting the ionic interactions the hold FN dimers in a compact formation leading to the formation of nanoscale FN fibrils. These fibrils had a nodular nanostructure which was proposed to be the overlap of adjacent, unfolded FN dimers. These results also suggested how negatively charged groups on the cell membrane may assist in FN fiber assembly by promoting the disruption of the compact, dimeric FN structure. Additionally, Salmeron-Sanchez et al have shown that FN forms elaborate fibrillar networks when adsorbed onto PEA but not poly(methyl acrylate) (PMA) substrates. When C2C12 cells were seeded on both FN adsorbed PEA, PMA, and control collagen substrates, myogenic differentiation was highest on the PEA substrates[121]. Furthermore, modulation of surface chemistry was shown to influence specific integrin-FN interactions which led to downstream changes gene expression, alkaline phosphatase enzymatic activity, matrix mineralization in osteoblast cell cultures[39]. These results

provide compelling evidence for how the conformation of FN can alter its bioactivity leading to changes in cell adhesion, gene expression, and differentiation. However, since these FN structures are permanently "pinned down" by protein-surface interactions it is difficult to measure how the structure of FN fibers may be dynamically changing.

Since significant progress has been made on FN fibers synthetically assembled in a cell-free environment, it is import to determine how closely these synthetic FN fibers recapitulate the structure, arrangement, mechanical, and biological properties of FN fibers generated by cells. To study the properties of cell-generated FN fibers, initial work utilized electron microscopy (EM) to identify the structure of FN dimers[132,133] and cell-generated FN fibers[94,134]. Using EM, Erickson and coworkers identified that FN dimers are highly flexible but have a contour length on the order of ~130 nm with diameter on the order of 2-3 nm[133]. Expanding electron microscopy studies towards cell-generated fibers, Chen et al identified that FN fragments (Fig. 1.5a-c) and FN fibers (Fig. 1.5d and e) both have nodular and smooth morphologies, where the nodule diameter was ~12 nm[94]. The nodular and smooth morphologies were found to exist along the same fiber, leading to the conclusion that the smooth regions of the fibers were under cell-mediated tension. This further suggests that cells are capable of modulating the morphology of FN arranged into fibers. Finally, through the use of site-specific monoclonal antibodies, it was shown that the heparin binding domain of FN was buried in smooth fibers but exposed in nodular regions. Thus, these early studies confirm that cell-generated tension is capable of modulating the structure of FN fibers which ultimately regulates the exposure of bioactive domains.

Over the past decade there has been investigation into the extent at which FN fibers can be mechanically manipulated and unfolded by cell-generated forces. Using chimeric cells that secreted FN containing green fluorescent protein, it was shown that broken FN fibrils contracted by about ¼ of their

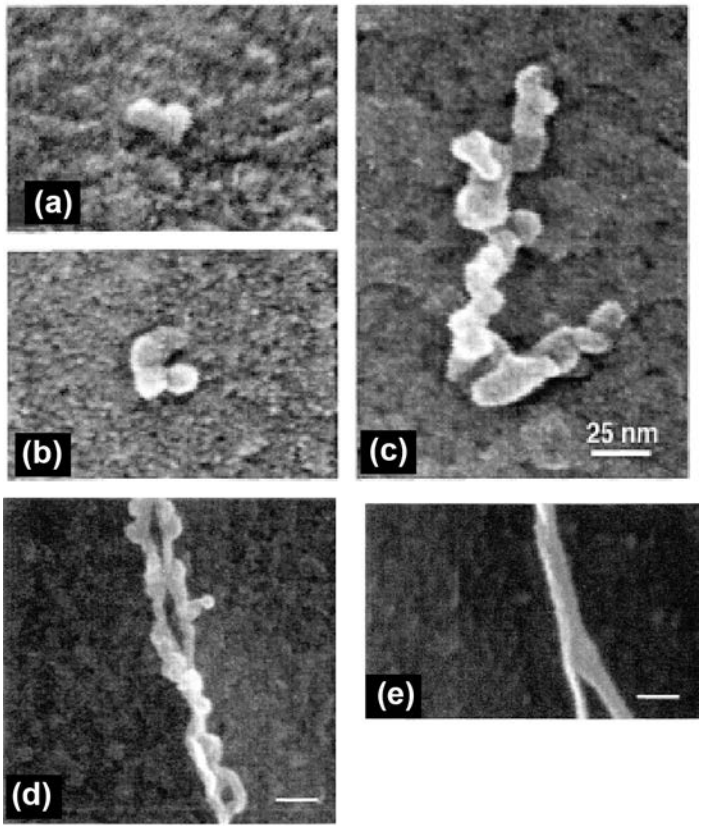

Fig. 1.5 High-resolution scanning electron microscopy images of FN fragments, dimeric FN, and FN assembled by cells. FN fragments that were (a) 85 kDa and (b) 180 kDa in size were imaged using scanning electron microscopy. These FN fragments only contain FN III and have a nodular morphology. (C) A scanning electron microscopy image of a FN dimer. High resolution electron microscopy images were also acquired for FN fibers generated by human foreskin fibroblasts. Electron microscopy indicated that FN fibrils exist in (d) nodular and (e) smooth conformations even along the same FN fiber. Scale bars are 25 nm. Adapted from Chen et al, 1997[94].

initial length suggesting that they were under a stretch of at least four times their resting length[135]. Further, by strategically labeling specific sites with donor and acceptor fluorophores, Smith et al was able to use Forster Resonance Energy Transfer (FRET) to measure FN III domain separation and presumably unfolding for FN fibers assembled by fibroblasts in culture. From these FRET experiments, it was shown that FN fibers exist in many different conformations in cell culture and some of the fibers are strained to the point of FN III domain separation and unfolding[136]. This FRET-based approach was also applied to demonstrate that preadipocytes exposed to tumorigenic factors produced an ECM with FN in a more

unfolded state compared to control cells[137]. These results suggest that, while the 8-fold extensions obtained in cell-free experiments have yet to be identified in cell-generated ECMs, FN can exist in multiple strained states that ultimately has an effect on its biological properties.

1.7. Thesis Organization

The goal of this thesis is investigate how FN fiber strain affects the structural and biological properties of FN. Through the modification and development of new methodologies, this thesis provides new insight into how the nanostructure of FN nanofibers dynamically changes as a function of strain and how these conformational changes might play a role in C2C12 myoblast adhesion and integrin expression. This thesis is arranged into three chapters followed by a concluding chapter.

1.7.1. Chapter 2: Engineering Monodisperse FN Nanofibers to Measure the Mesoscale Mechanical Behavior of Fibronectin

While FN fibers have been shown to be highly extensible both in cell culture and in cell-free environments a complete chemo-mechanical characterization of these fibers is still incomplete. The goal of this chapter is to track FN nanofiber morphology over large strains associated with a SIA release process. Since it is difficult to track individual FN nanofibers throughout the SIA release process, phase contrast microscopy was used to confirm that FN nanofibers were indeed monodisperse in both pre- and post-release states. Using AFM, I found that despite significantly large changes in FN nanofiber length, width, and thickness, the volumes of the FN nanofibers in both pre- and post-release states remained constant suggesting that they behaved as incompressible materials for these strain ranges. Finally, by increasing the resolution of the AFM imaging I was able to correlate the observed changes in FN nanofiber length, width, and thickness with conformational changes within the nanostructure. These results provide insight into how conformational changes allow FN fibers to withstand large deformations. This work is currently in review by the journal *Scientific Reports*.

1.7.2. Chapter 3: Elucidating the Strain-Dependent Structural Changes of Fibronectin Nanofibers

Understanding how the conformation of FN molecules dynamically changes in response to a variety of forces is paramount for developing a mechanism for the exposure of cryptic binding sites within FN fibers. While current techniques enable the mechanical characterization of FN fibers that are ~5 μm in diameter, it is difficult to directly measure how applied forces dictate conformational changes within their nanostructure. Moreover, other methods enable the structural characterization of surface adsorbed FN fibrils yet these fibrils are permanently pinned to the surface. The goal of this chapter was to investigate how the nanostructure of FN fibers dynamically changes as a result of strain. This was accomplished by releasing FN nanofibers using SIA, straining them, and immobilizing them in the strained state. Because the nanofibers were ~1 cm in length, I developed an approach to label the FN nanofibers with FN-based fiduciary marks. This enabled a precise measurement of strain along the length of the nanofibers. Finally, high resolution AFM analysis revealed strain-dependent molecular conformations within the nanostructure of the fibers. These results provide unique perspective into how the nanostructure of FN fibers dynamically changes as a function of strain.

1.7.3. Chapter 4: Development of a Patterning-on-Topography Method to Measure the Effect of Fibronectin Strain on C2C12 Myoblast Adhesion

Current approaches to study the mechanically-induced activation or deactivation of FN binding sites, including force-based assembly and SIA techniques, are typically limited to using of small molecules and peptides since the FN fibers are only ~5 μm in diameter. Because of their small dimensions, they do not represent an optimal cell culture substrate. Even FN fibers prepared using SIA significantly decrease in width, particularly when uniaxially stretched. Additionally, approaches using surface-adsorbed FN are limited to studying the cell behavior on only a few discrete FN conformations. Therefore the goal of this chapter was twofold. The first was to develop and modify a technique that enabled FN to be strained in a controllable manner while also maintaining a wide geometrical area to represent an ideal cell culture substrate. This was accomplished through the development of a Patterning-on-Topography (PoT) technique which is an extension of SIA. In this approach, the swelling and

dissolution of PIPAAm “pushes” FN between well-defined micro-ridges. The strain imposed on FN as it is pushed between the micro-ridges can be modulated by increasing or decreasing the micro-ridge aspect ratio. Importantly, the FN can be engineered as 1 cm x 1cm sheets making the FN-coated micro-ridges ideal cell culture substrates where the micro-ridge tops contain unstrained FN and the trenches between micro-ridges contain strained FN. The second goal of this chapter was to use PoT to investigate whether FN strain can affect C2C12 myoblast adhesion and integrin expression. I hypothesized that FN strain-induced deactivation of the synergy-RGD site coupling would decrease cell spreading and α_5 integrin expression. Unexpectedly, I found that strain imposed on the FN sheets promoted a decrease in the FN surface coverage. While decreasing surface coverage was found to contribute to a decrease in cell spreading, I also found that FN strain prompted further decreases in cell spreading area and α_5 integrin expression compared to unstrained controls. These results provide unique insight into how mechanically-induced conformational changes in FN may influence cell behavior. The work based on the development of PoT was published in *Nature Methods*, 12(2), 134-136. This work was the result of contributions from Quentin Jallerat, Yan Sun, and myself in which we are all co-first authors. The latter part of this chapter is currently unpublished.

CHAPTER 2:

Engineering Monodisperse Nanofibers to Measure the Mesoscale Mechanical Behavior of Fibronectin

2.1. Abstract

Cells are capable of sensing and responding to the chemical and physical properties of their microenvironment. Despite significant progress in understand how rigidity, geometry, and topology in the cell microenvironment can affect cell behavior both *in vivo* and *in vitro*, a complete understanding of the chemo-mechanical properties of many ECM proteins is still lacking. In this study, we used a surface-initiated assembly (SIA) technique in order to provide new insight into the elastic behavior of FN nanofibers over large dimensional changes in length, width, and thickness. We found that when initially patterned onto a poly(N-isopropylacrylamide) (PIPAAm) substrate, the FN nanofibers have a nanostructure comprised of interconnected, partially unfolded constituent molecules. When released from the PIPAAm substrate via thermally triggered dissolution, the FN nanofibers rapidly contracted in solution and ultimately, we observed large, approximately 3.3-fold and 9-fold changes in length and width, respectively. Despite these large dimensional changes, the volume remained conserved suggesting that the FN nanofibers were behaving as incompressible materials over these strain ranges. Furthermore, we found that there were distinct morphological differences within the nanostructure of nanofibers in pre-release and post-release states. FN nanofibers in a pre-release state had a nanostructure that was fibrillar and isotropic whereas the nanostructure of FN nanofibers post-release contained elliptically shaped nodules on the order of several hundred nanometers. In summary, we found that FN nanofibers prepared using SIA were able to undergo large deformations while maintaining constant volume and this process was largely driven by morphological changes within the nanostructure.

2.2. Introduction

The extracellular matrix (ECM) is a heterogeneous, fibrillar network that plays a multifunctional role in development, wound healing, maintaining homeostasis and disease progression[8,12,19,138,139]. Fibronectin (FN) is a ubiquitous ECM protein that is a major component of the provisional matrix established during both embryonic development and wound healing[43,140]. An important function of FN during these processes is to provide sites for cell adhesion, sequester growth factors, and act as a template for the assembly of other ECM components[34,78,141]. Specifically, FN contains binding domains for cell surface receptors such as integrins and syndecans, collagen, heparin, and self-assembly[34,35,76]. Some of these sites are cryptic and require conformational changes of the secondary and/or tertiary structure in order to become exposed. In cell culture, cell generated forces are capable of unfolding FN from a globular compact state to an extended state to trigger FN polymerization. Understanding how cells mechanically manipulate FN fibrils to modulate the exposure of cryptic domains is critical in developing a mechanistic model of ECM mechanobiology.

The challenge of studying the mechanical and structural properties of FN fibers synthesized and assembled by cells is primarily due to the large heterogeneity in the length and diameter of these fibers. Additionally, FN represents only a fraction of the many molecules that comprise the ECM in tissues. Therefore, several methods have emerged to synthetically assemble FN fibers in a cell-free environment with the common theme of inducing conformational changes to expose cryptic self-assembly sites. These methods include the use of denaturants[113,114], protein-surface interactions[121,122,130,131], and surface tension at the air-liquid interface[105,120]. Altogether, these studies confirm that, by inducing the exposure of cryptic self-assembly sites, it is possible to polymerize FN into fibers in a cell-free system.

In this study, we used a surface-initiated assembly (SIA)[123] technique to engineer monodisperse FN nanofibers and, in combination with AFM, tracked the nanofiber morphology over large strains associated with the assembly process. Since previous work using tensile testing has demonstrated that FN fibers exhibit elastic behavior over specific strain ranges[125], we hypothesized that FN nanofibers would

exhibit elastic, incompressible behavior from the as-patterned, fibrillar state to the fully contracted, post-release state. We propose that this is primarily due to distinct morphological changes within the nanostructure. To accomplish this, we engineered short FN nanofibers that were initially patterned as 50 μm long and 20 μm wide rectangles such that the entire nanofiber could fit within the AFM scan area. Using AFM, we found that the nanofibers were indeed monodisperse and that the nanofiber volume was conserved between extended, pre-release and contracted, post-release states suggesting elastomeric behavior. At higher resolution, we found that FN nanofibers in a pre-release state exhibited a fibrillar nanostructure whereas the nanostructure of FN nanofibers post-release was comprised of elliptically-shaped nodules. While not identical to cell-generated FN fibers, our results provide insight into how strain-dependent changes in molecular conformation may underlie the mechanobiology of FN in the native ECM.

2.3. Materials and Methods

2.3.1. FN Nanofiber Fabrication.

FN nanofibers were prepared as described previously[123,124]. Briefly, poly(dimethylsiloxane) (PDMS) stamps patterned with 50x20 μm raised rectangles were fabricated by first spincoating glass wafers with SPR 220.3 positive photoresist (Microchem). The photoresist was then exposed to UV light through a photomask and developed using MF-319 developer (Microchem). A negative of the patterned photoresist wafer was formed by casting PDMS prepolymer (Sylgard 184, Dow Corning) over it and curing it in an oven at 65° C for 4 hours. The cured PDMS was then peeled off the glass wafer and 1 cm^2 stamps were cut out.

Prior to use, the PDMS stamps were sonicated in a 50% ethanol solution for 30 minutes and then dried under a stream of nitrogen. The stamps were then incubated with FN (BD Biosciences) at a concentration of 50 μg/mL in ddH_2O water for 30 minutes, washed to remove excess FN, and then dried under stream of nitrogen. FN coated PDMS stamps were then brought into conformal contact of PIPAAm coated coverslips for 10 minutes to create arrays of 50 x 20 μm FN rectangles on the PIPAAm surface. The PIPAAm coated coverslips were prepared by spincoating a 10% PIPAAm (Polysciences Inc.) in 1-butanol (w/v) solution. Upon removal of the stamps, the quality of the FN rectangles on the PIPAAm was inspected using phase contrast microscopy. The FN patterns were released from the PIPAAm surface by adding warm, ~40° C, ddH_2O and allowing the temperature to gradually drop below the LCST of PIPAAm resulting in the dissolution of the PIPAAm layer and the non-destructive release of the nanofibers. To test detergent solubility, the nanofibers were released in either a solution containing 2% (w/v) sodium dodecyl sulphate dissolved in ddH_2O or a solution containing 2% (w/v) sodium deoxycholate dissolved in ddH_2O.

2.3.2. Measuring Dynamic Changes in Nanofiber Morphology.

The FN nanofiber release was monitored optically using phase contrast microscopy and time-lapse images were captured using a Photometrics CoolSnap ES digital camera (1392 x 1040 pixels) at a frame rate of 1 fps. The contour length of 15 nanofibers was measured pre-release (-77 and -23 sec), at the initiation of release (0 sec), and post-release from the PIPAAm surface (4, 30, 60, 90, 120, 150, 180, 210, 240, 600, 1500, and 7200 sec) using ImageJ (National Institutes of Health)[142].

2.3.3. Atomic Force microscopy of Nanofiber Morphology.

AFM (MFP3D-Bio, Asylum Research) was used to analyze the nanostructure and quantify the morphology of FN nanofibers both pre-release and post-release. The FN nanofibers were scanned in air using AC mode with AC160TS cantilevers (Olympus Corporation). Nanofibers in a pre-release state were scanned on the PIPAAm surface whereas FN nanofibers post-release were first immobilized in the post-release state back onto the glass coverslip. They were then washed three times with ddH_2O to remove the dissolved PIPAAm, and then dried in a 65° C oven. FN nanofibers pre-release were scanned with a scan size of 512 x 512 lines over a scan area of ~52 μm x 52 μm and FN nanofibers post-release were scanned with a scan size of 512 x 512 lines over a scan area of ~15μm x 15 μm. High-resolution AFM images were obtained using a scan size of 1024 x 1024 lines over a scan area of 3 μm x 3 μm for the nanofibers pre-release (zoomed in to a 500x500 nm area after acquisition) and 2x2 μm for nanofibers post-release.

2.3.4 Data Analysis and Statistical Methods.

To accurately quantify FN nanofiber morphology, the AFM height signal of each nanofiber was first processed to ensure the background surface was flat and centered at 0 nm. To accomplish this, the FN nanofibers in the image were masked and the non-masked area was subject to a 1st order planefit and a 2nd order flattening. The width at five transverse locations and contour length for ten nanofibers were then measured using the IGOR Pro software environment. FN nanofiber volume and thickness were also measured using the IGOR Pro software environment. Briefly, each nanofiber was masked and the volume

was calculated by multiplying the height of each pixel within the mask by the area of the pixel. The total volume measured as the summation of all the pixel volumes within the nanofiber. Since thickness was heterogeneous along the length and width of the nanofibers, the average fiber thickness was quantified by dividing the volume of the nanofibers by its area. The Mann-Whitney rank sum test with $P<0.05$ was used for statistical analysis unless otherwise noted (Sigma Plot, Systat Software Inc.).

2.4. Results

2.4.1. Fabrication of Monodisperse Nanofibers Using Surface-Initiated Assembly.

In this study, we modified a SIA technique to engineer short FN nanofibers that were 50 μm in length and 20 μm wide. Briefly, FN in its compact, solution conformation was incubated on a microfabricated PDMS stamp patterned with raised 50 μm long and 20 μm wide rectangles. Adsorption on the hydrophobic PDMS resulted in the FN dimers obtaining a partially unfolded conformation (Fig. 2.1a). FN was then transferred in the partially unfolded state to a PIPAAm surface through microcontact printing (Fig. 2.1b). Hydration in distilled water and reduction of the solution temperature below the lower critical solution temperature (LCST, ~32° C) of PIPAAm triggered its dissolution and the release of assembled, insoluble, and free-standing FN nanofibers (Fig. 2.1c).

We first used optical microscopy to track the dynamic morphological changes of the FN nanofibers during the release process. We then released FN nanofibers in distilled water and, upon dissolution of PIPAAm, the nanofibers rapidly contracted both lengthwise and widthwise (Fig.2.2a). This is consistent with previous reports of FN nanofibers formed using SIA[123,125]. These fibers remained stable in solution as insoluble fibers for at least several weeks. Next, to establish the maturity of the FN nanofibers whether the FN-FN interactions were covalent or non-covalent we released the FN nanofibers in 2% deoxycholate (DOC) and 2% sodium dodocylsulfate (SDS) solutions. DOC solubility represents the gold standard for assessing FN fiber maturity. McKeown-Longo and Mosher demonstrated that nascent FN fibrils assembled by cells are initially DOC soluble but they are converted to DOC insoluble fibers as they elongate, thicken, and establish sufficient FN-FN interactions[110,143]. Upon release in a 2% DOC solution, the FN nanofibers were observed to be insoluble suggesting there were sufficient FN-FN interactions to prevent DOC solubility. To assess whether the interactions were purely noncovalent, we released the FN nanofibers in a 2% SDS solution. SDS is commonly used in gel electrophoresis experiments where it unfolds proteins via disrupting noncovalent interactions while preserving the covalent bonds in the protein backbone[111,144,145]. When released in a 2% SDS solution, the FN nanofibers

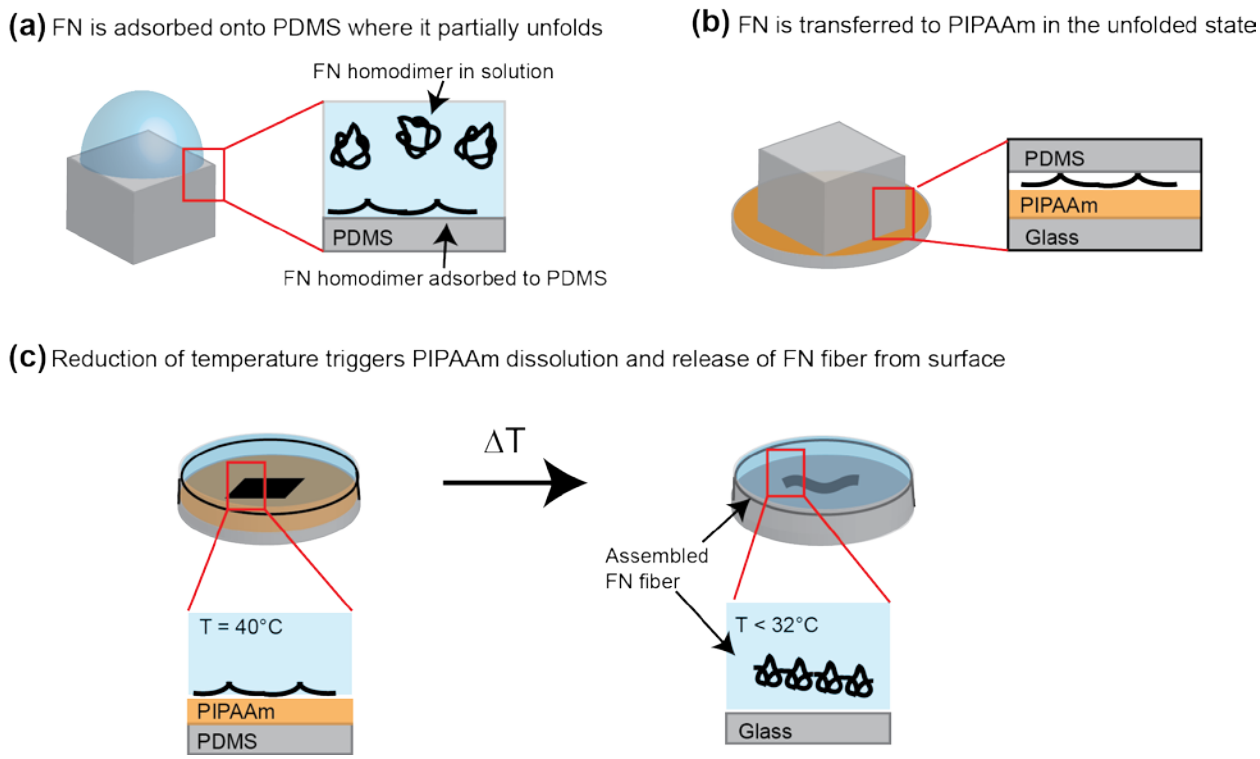

Fig. 2.1. A schematic of the surface-initiated assembly process. (a) FN homodimers in their solution conformation were adsorbed onto a hydrophobic PDMS stamp where they obtained a partially unfolded conformation. (b) The FN dimers were then transferred in the unfolded state to a PIPAAm surface via microcontact printing to create an array of patterned nanofibers. (c) The PIPAAm was hydrated at an elevated temperature and allowed to cool below its LCST resulting in the release of an assembled FN nanofiber.

rapidly dissolved into solution, even before reduction of the solution temperature. Review of the literature suggests that the immediate dissolution of the PIPAAm was due to the SDS raising the LCST of PIPAAm by disruption of critical noncovalent interactions responsible for maintaining the insoluble state of PIPAAm[146-148]. These results suggest that FN nanofibers engineered using SIA have sufficient FN-FN interactions to prevent DOC solubility, comparable to mature cell-assembled FN fibers. Furthermore, the rapid dissolution in SDS indicates that the FN-FN interactions were noncovalent.

Measuring the contour length of the FN nanofibers during the release process enabled quantification of the contraction kinetics (Fig. 2.2b). Results demonstrate that the nanofibers initially underwent a rapid contraction upon dissolution of PIPAAm follow by a slower rate of contraction over

the course of several hours until the final contracted length was reached. Prior work in the literature found that FN fiber contraction following uniaxial tensile testing could be fit to a double exponential curve and that the FN fibers contracted through a fast and slow regime[119,125]. Therefore, we fit the contour length as a function of time of nanofibers released using SIA to a double exponential curve ($r^2 = 0.99$),

$$l(t) = A_0 + A_1 e^{\frac{-t}{\tau_1}} + A_2 e^{\frac{-t}{\tau_2}}$$

where the parameters A_o, A_1, and A_2 represent the final contracted length, the decay amplitude, and the fitting parameter, respectively. FN nanofibers were found to have a fast contraction regime, τ_1, of 2.88 seconds and a slow contraction regime, τ_2, of 157.41s. These two rates suggest that FN nanofibers contract rapidly upon release to an intermediate conformation and over the course of several hundred seconds continue to slowly contract until the final post-release length is reached. Interestingly, the contour length of the nanofibers at each time point did not have a large variability suggesting that the nanofibers contracted in a similar manner. Elucidating the molecular mechanisms behind the two contraction regimes raises some important research questions although that is beyond the scope of this work.

Next, we compared the FN contour length in the as-patterned, pre-release state to the contour of the nanofibers post-release after their final contracted length was reached. We found that the nanofibers were initially patterned as 50.12 ± 0.41 μm in length, confirming that the nanofibers were initially monodisperse with <1% variation in length (Fig. 2.2c). Post-release, the nanofiber length stabilized at 14.15 ± 0.92 μm, approximately a 3.5-fold decrease in length from the pre-release state. We did not measure changes in width due to insufficient optical resolution of the phase contrast microscope although it is reasonable to assume the nanofibers decreased in width from the pre-release to post-release states.

2.4.2. High Resolution Analysis of Nanofiber Dimensional Changes Using Atomic Force Microscopy

Since the initial optical measurements of the FN nanofibers revealed that the nanofibers were monodisperse throughout the release process, we were able fully quantify the morphological changes using AFM without concern for significant fiber-to-fiber variability. Initial optical measurements

confirmed that the FN nanofibers were monodiserpse lengthwise (Fig. 2c), but we wanted to confirm this in all dimensions (Fig. 2.3). Each FN nanofiber (pre- and post-release) was measured at five transverse locations and then down the middle to measure the mean fiber width and contour length, respectively (Fig 2.3a and b). FN nanofibers pre-release were monodisperse in their planar dimensions with a length of 51.32 ± 0.19 μm and a width of 21.90 ± 0.24 μm (Fig. 2.3c, d, n=10). The nanofibers were then released by thermal dissolution of PIPAAm, allowed to fully contract in solution, dried onto a coverslip, and again scanned by the AFM. As expected, the FN nanofiber length and width significantly decreased to 15.57 ± 3.75 μm and 2.29 ± 0.78 μm, respectively (Fig. 2.3c, d). These dimensional changes correlate to approximately a 3.3-fold change in length and a 9-fold change in width. Additionally, the FN nanofibers were observed to anisotropically contract as the length:width nanofiber aspect ratio changed from a median value of 2.5 for nanofibers pre-release to a value of 6.6 for nanofibers post-release (Fig 2.3e).

This anisotropy is likely due to the rectangular shape of the FN nanofibers as FN squares contract symmetrically[149]. Because the AFM measurements were performed in air to maximize resolution, we also wanted to confirm that dehydration of the nanofibers did not affect the measured post-release dimensions. By comparing the contour length of FN nanofibers measured optically in solution (Fig. 2.2c) to those measured in air by AFM (Fig. 2.3c), we found that the two were statistically equivalent (Mann-Whitney Rank Sum Test, P=0.42). While dehydration did not have an effect on the nanofiber length, we cannot rule out the possibility that dehydration may affect other dimensions.

Although the FN nanofiber length and width significantly decreased, the nanofiber thickness was found to significantly increase (Fig. 2.3f). Pre-release, the nanofiber thickness was 4.33 ± 0.18 nm, consistent with what has been previously report for FN fibrils formed on polysulfonated surfaces as well as the diameter of partially unfolded FN dimers with secondary structure intact. Post-release, the nanofiber thickness increased to 114.65 ± 33.41 nm (Fig. 2.3f) with a variable maximum thickness ranging from 40 nm up to 400 nm (Fig. 2.3b). This large variability can be attributed to the nanofiber folding up on itself during the drying process. Despite significant morphological changes, the FN

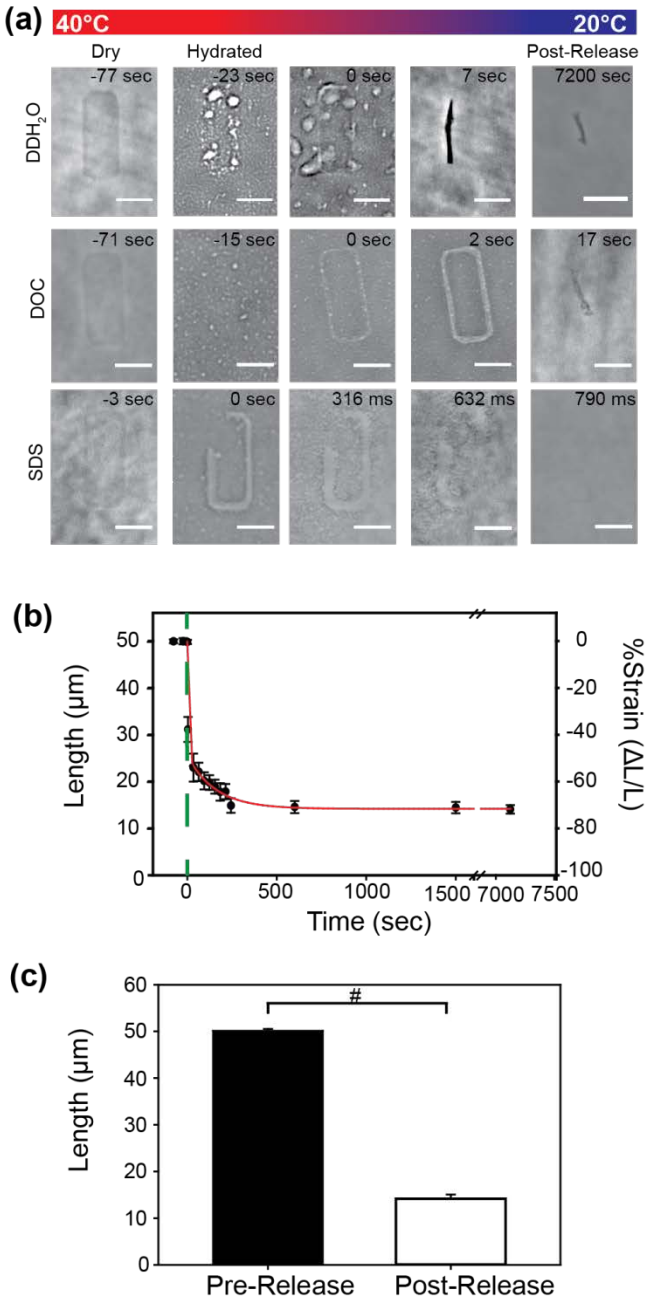

Fig. 2.2. Measuring the dynamic changes in FN nanofiber length during the release process. (a) Time lapse sequences of FN nanofibers released in DI water, DOC, and SDS. The times are relative to the initiations of the release from PIPAAm. (b) The contour length of FN nanofibers released in distilled water. The contour length as a function of time after release (green dashed line) was fit to a double exponential curve (r^2 = 0.99) with a rapid contraction regime τ_1 = 2.88 sec and a slower contraction regime, τ_2 = 157.41 sec. (c) Monodisperse nanofibers 50.12 ± 0.41in length pre-release contracted to a final length of 14.15 ± 0.92 µm, a 3.5-fold decrease in length from the pre-release state. Scale bars are (a) 20 µm, errors bars (b and c) are standard deviation and the symbol # indicates a statistically significant difference with $P < 0.05$.

nanofiber volume was statistically equivalent with a volume of 4.69 ± 0.34 μm^3 for nanofibers pre-release and 4.78 ± 0.59 μm^3 for nanofibers post-release (Fig. 2.3g, t-test, P=0.68). This suggests that the nanofibers behaved as incompressible materials with a Poisson's ratio of ~0.5[150]. Ideally, the measurement of Poisson's ratio would have involved the measurement of changes in length, width, and thickness but because the FN nanofibers folded over themselves after release we instead estimated Poisson's ratio by measuring the volume.

To validate whether FN nanofibers maintained incompressible behavior over small strains, we modified our approach to engineer FN nanofibers that were ~67 nm wide and 1 cm long. We labeled the FN nanofibers with FN-based fiduciary marks (See Chapter 3, Fig. 3.1) and uniaxially stretched them. FN nanofibers pre-release had a center-to-center fiduciary mark distance of 20.21 ± 0.68 μm (n=3, Fig. 2.4a). When released, strained, and immobilized for AFM imaging, we measured an average fiduciary mark center-to-center distance of 40.06 ± 8.68 μm (n=5, Fig. 2.4b) representing an average strain of 98.22% (See chapter 3 and Fig. 3.2 for more details on the measurement of strain). When we measured the volume of the FN segments between the fiduciary marks, we found that the volume decreased slightly from 3.86 ± 0.79 μm^3 to 3.38 ± 0.57 μm^3 (Fig. 2.4c) although there was no statistical difference between the two (P=0.35) suggesting that the FN nanofibers were again behaving as incompressible materials over this strain range. This is in agreement with the most biological tissues[151-154] although this is in direct contrast with the behavior of fibrin networks under tension. These fibrin networks were found to have an ~80% decrease in volume associated with strains upwards of 100%. This was found to be due to water expulsion and unfolding of the constituent fibrin molecules[155]. Further investigation is needed to determine whether volume conservation is lost in FN nanofibers due to protein unfolding.

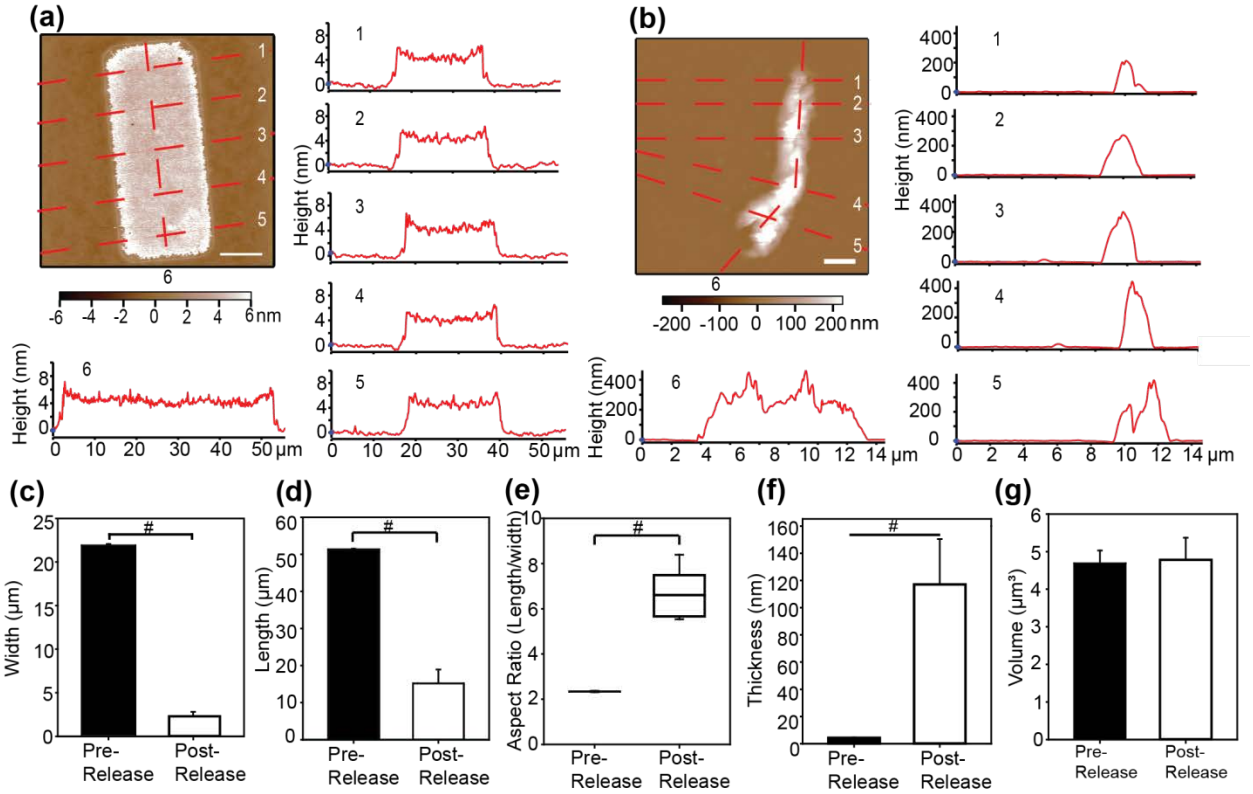

Fig. 2.3. Quantifying the morphology of 50 µm x 20 µm FN nanofibers in pre- and post-release states using AFM. (a) Pre-release and (b) post-release FN nanofibers were measured at five transverse locations to determine the width and longitudinally along the center to determine the contour length. (c) Nanofiber width was monodisperse and the nanofibers underwent a 9-fold change in length upon release. (d) Nanofiber length was also monodisperse and the nanofibers underwent a 3.3-fold change in length upon release. (e) The pre-release aspect ratio of the FN nanofibers significantly increased due to a larger contraction along the width of the nanofibers. (f) Unlike the length and width, the nanofiber significantly increased upon release. (g) Nanofiber volume was statistically equivalent between pre- and post-release nanofibers indicating that nanofibers were incompressible over this strain range. Scale bars are (a) 10 µm and (b) 2 µm and the symbol # indicates a statistically significant difference with $P < 0.05$.

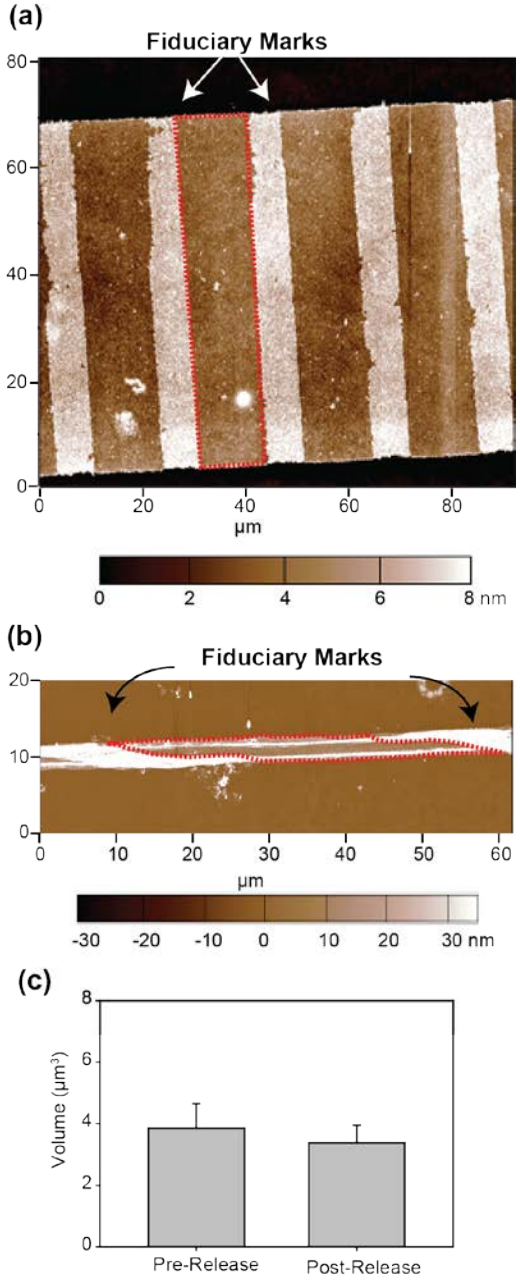

Fig. 2.4. Quantifying the volumetric changes in strained FN nanofibers. (a) An AFM scan of a ~67 nm wide FN nanofiber in a pre-release state on PIPAAm. (b) After being strained to ~98%, the FN nanofiber was immobilized in the strained state and scanned using AFM. (c) Quantification of FN nanofiber volume (measured within red dotted lines) indicates there was no statistical difference.

2.4.3. FN Nanofibers Pre- and Post-Release Exhibit Distinct and Different Nanostructures

Since the FN nanofibers have a nanoscale thickness (Fig. 2.3f), the molecular morphology of the FN nanofibers can be resolved using AFM at high resolution. An entire FN nanofiber pre-release was first scanned at low resolution (Fig. 2.5a) followed by a high resolution sub-region was scanned to reveal that the nanostructure was comprised of interconnected fibrils in an overall isotropic network (Fig. 2.5b). At this resolution, it was clear that multiple elongated fibrils formed an interconnected FN network with distinct points of intersection. The fibrils connecting these intersections were of interest because their nanometer scale suggested that they may be single FN dimers. The average diameter of these fibrils was found to be 5.72 ± 2.64 nm (n = 151, Fig. 2.5c) where fibrils as small as ~3 nm and as large as ~17 nm were also observed. Since the diameter of an unfolded FN dimer with secondary structure intact is ~2-3 nm[132,133], we attributed these different size regimes as containing single and multiple unfolded FN dimers in parallel. In summary, the nanostructure of FN nanofibers pre-release is comprised of an isotropic, interconnected network of FN fibrils where one or multiple partially unfolded FN molecules span between points of intersection.

FN nanofibers post-release were also scanned using AFM, first at low resolution (Fig. 2.5d) and then high resolution subsections were acquired from the edge (Fig. 2.5e) and interior (Fig. 2.5f) regions of the nanofiber. Unlike the nanostructure of FN nanofibers pre-release, the nanostructure of FN nanofibers post-release had no visible fibrils and instead had a distinct nodular structure. These elliptically-shaped nodules nodules had a major axis length of 173.69 ± 57.84 nm (n=239) and 254 ± 65.32 nm (n=102) for the interior and edge nodules, respectively (Fig. 2.5g). Similarly, the minor axis length of the nodules was 117.15 ± 42.03 nm and 169.94 ± 49.40 nm for the interior and edge nodules, respectively (Fig. 2.5h). In both cases, these nodules were comparable to the nanostructure observed for FN fibers synthetically assembled using SIA[123] and those assembled on microfabricated surfaces[115], negatively charged surfaces[122]. However, the nodules in our engineered FN nanofibers were measurably larger than those previous studies and in the case of the FN nanofibers previously investigated using SIA, it is unclear

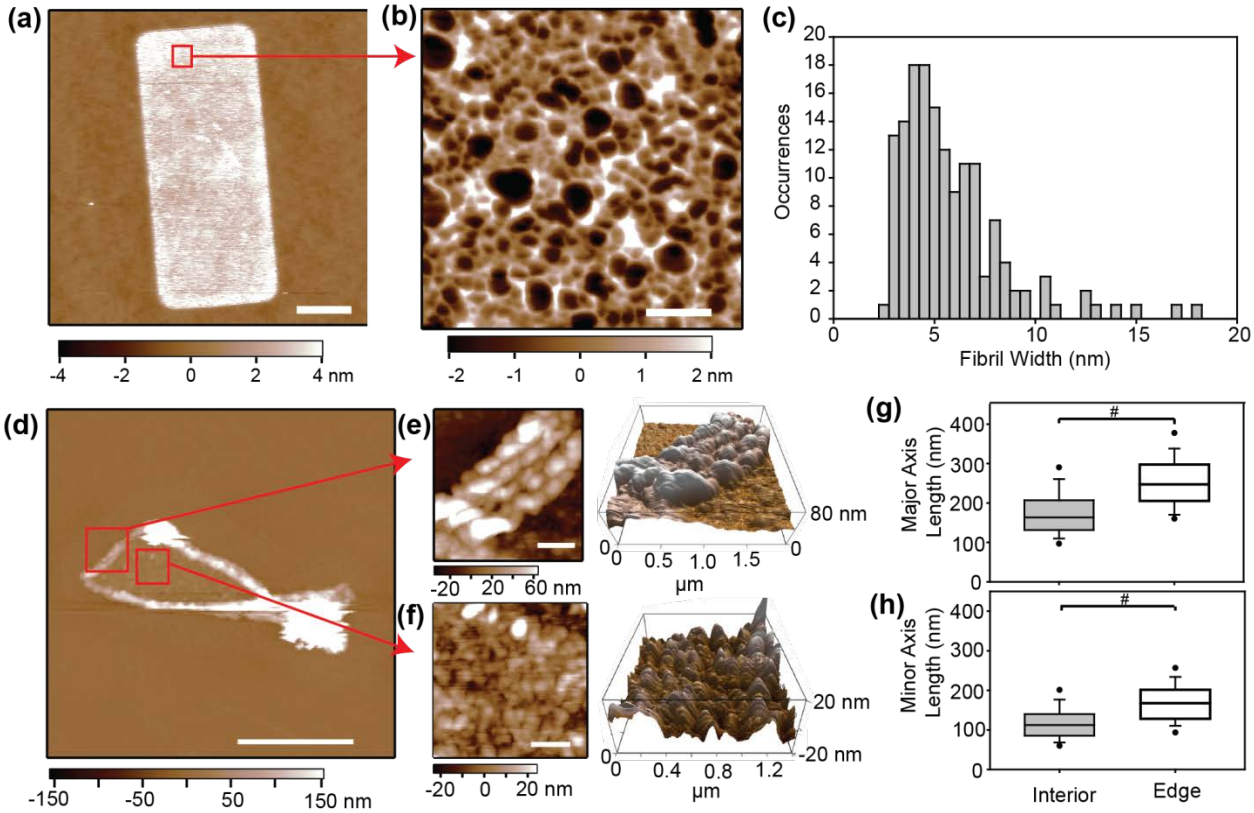

Fig. 2.5. The nanostructure of FN nanofibers pre- and post-release. (a) An AFM scan of an entire FN nanofiber pre-release. (b) A high resolution AFM scan of a subregion of (a) revealed a fibrillar nanostructure consisting of nodes interconnected by linear fibrils. (c) The widths of the linear fibrils connecting the nodes had an average diameter of 5.72 ± 2.64 nm although fibrils width diameters as small as ~3 nm and as large as ~17 nm were also observed. (d) An AFM scan of an entire FN nanofiber post-release. (e) The edge region contained elliptically-shaped nodules ~80 nm in height whereas (f) the interior region contained nodules that were smaller with a height of ~40 nm. The nodules in the edge region had a significantly large (g) major axis and (h) minor axis length than the nodules found in the interior region. Scales bars are (a) 10 µm, (b) 100 nm, (c) 5 µm, and (e and f) 500 nm. The symbol # indicates a statistically significant difference with $P < 0.05$.

whether they were allowed to fully contract in solution or by using shorter, 50 µm x 20 µm, FN nanofibers, we are enabling the nanofibers to more fully contract. To put these results in a physiological context, we reason that FN homodimers were able to partially unfold and obtain a fibrillar conformation in nanofibers pre-release, and, upon release, the dimers were able to refold in solution to a globular conformation. Since the nodules measured in the nanofibers post-release were much larger than single FN homodimers in a solution, globular conformation (~50 nm[156]) it is likely that the nodules contain many folded FN homodimers clustered together.

2.5. Discussion

In this study we used a SIA technique to engineer populations of monodisperse FN nanofibers that, in combination with AFM, allowed us to investigate the micro- and nanoscale morphological changes associated with large strains. Because the engineered FN nanofibers are not identical to cell generated FN fibers, detergent solubility provided insight into how the nanofibers used in this study might be similar to cell-generated fibers. In tissues and in cell culture, nascent FN fibrils are initially DOC soluble but become DOC insoluble as the number of FN-FN interactions increases[35,110]. Eventually, the FN fibers can become covalently crosslinked through disulfide isomerase activity[157,158] rendering them insoluble to SDS. We found that FN nanofibers release in a 2% (w/v) DOC solution (Fig. 2.2a) were capable of assembling and remaining insoluble in solution. Contrarily, when released in a 2% (w/v) SDS solution, the FN nanofibers rapidly dissolved. Altogether, this suggests that the FN nanofibers formed sufficient FN-FN interactions to prevent DOC solubility, however, these interactions were purely noncovalent as the nanofibers readily dissolved in SDS.

Because it is difficult to track individual nanofibers from thermally triggered release to AFM imaging, we first wanted to confirm that there was negligible fiber-to-fiber variability. Optical measurements of FN nanofibers in solution followed by higher resolution measurements using AFM allowed us to confirm that FN nanofibers engineered using SIA were indeed monodisperse. Moreover, by engineering nanofibers that were 50 μm long and 20 μm wide, we were able to image the entire nanofiber in both pre- and post-release states. This allowed us to quantify the nanofiber volume with nanometer-scale precision and demonstrate that, despite significant changes in length, width, and thickness, the FN nanofiber volume was conserved. Ultimately, this suggests that the FN nanofibers behaved as incompressible, materials[150] for the strains associated with the SIA process.

Using AFM at high resolution, we found that conformational changes within nanostructure were the driving force behind the large microscale changes in length, width, and thickness. Specifically, we found that FN nanofibers pre-release are comprised of an overall fibrillar network with the smallest

resolvable feature being linear fibrils with a diameter of ~3 nm (Fig. 2.5). This is consistent with the report diameter of FN dimers in an unfolded state without the loss of secondary structure[133]. This was further confirmed by Deravi *et al*, whom demonstrated representative peaks for β-sheet secondary structure using Raman spectroscopy for similar FN nanofibers[125]. In contrast, FN nanofibers post-release had a nanostructure comprised of elliptically-shaped nodules that were larger than what would be expected for single, globular FN dimers. While our experimental setup limited us to observing the nanostructure only at the pre-release and post-release states, we can infer that the partial unfolding of FN dimers pre-release was sufficient to expose cryptic self-assembly sites. At points of intersection, multiple unfolded dimers overlapped enabling the formation of FN-FN interactions. Post-release, interacting dimers refolded simultaneously in solution leading to the formation of a nodular structure where each nodule is at least several times larger than a single FN dimer in solution.

In summary, we demonstrated the ability to fabricate monodisperse FN nanofibers that can be used to study the mechanical and structural properties of FN as a function of strain. Using AFM, we found that despite significant changes in length, width, and thickness between nanofibers pre- and post-release, nanofiber volume remained conserved suggesting incompressible behavior over the strains observed. We found that the large microscale dimensional changes during the release process were driven by changes in the nanostructure of the FN molecular network from an unfolded, fibrillar structure pre-release to a nodular structure post-release. Altogether, our results provide insight into the mechanical behavior of insoluble FN nanofibers and how strain-dependent changes in molecular conformation may underlie the mechanobiology of FN in the native ECM.

CHAPTER 3:

Elucidating the Strain-Dependent Structural Changes of Fibronectin Nanofibers

3.1. Abstract

Fibronectin is an extracellular matrix (ECM) glycoprotein that plays an important role during many important biological processes such as wound healing, embryonic development and even disease. Since emerging evidence has demonstrated how FN contains mechanosensitive properties, many researchers have investigated how the application of force induces conformational changes within FN to expose otherwise cryptic binding domains. Due to inherent limitations associated with FN fiber fabrication strategies it has proven technically challenging to dynamically monitor how the nanostructure of FN fibers changes as a result of strain. Here, we used a modified surface-initiated assembly (SIA) technique to release fully assembled FN fibers onto PDMS supports, strain the FN fibers using micromanipulators, and subsequently immobilize them in the strained state for high resolution atomic force microscopy (AFM) imaging. Using this approach, we were able to track how the nanostructure changed within FN nanofibers from fully contracted to highly strained. In fully contracted FN fibers we observed large, isotropically-oriented nodules that became progressively smaller with increasing strain. At maximum strain, the nanostructure was highly aligned and contained small nodules in a 'beads-on-a-string' arrangement. In summary, we establish an approach to strain FN fibers and dynamically monitor how the nanostructure changes as a function of strain using AFM. Our results provide new insight into how strain can affect the morphology of the constituent FN molecules.

3.2. Introduction

Fibronectin (FN) is a ubiquitous extracellular matrix (ECM) glycoprotein that plays a major role in many biological processes including development, wound healing, and blood clotting[12,43,62,139]. In addition to providing binding sites for mammalian and bacterial cells[12,42], FN contains binding sites for other ECM components such as collagen, fibrin, heparin, growth factors, and self-assembly[34,78,80]. Some of these sites have been identified as cryptic and require conformational changes in the tertiary and/or secondary structure to become exposed. While these sites may become exposed by cleavage at specific sites, it is also believed that cells are capable of using contractility forces to unfold FN and expose cryptic sites[59,109]. Understanding how cells can manipulate and mechanically deform FN fibers to modulate the exposure of cryptic sites is critical for developing a mechanistic model of ECM mechanobiology and may underlie the importance of FN during many critical biological processes such as tissue formation and disease progression.

Due to the complexity of the native ECM, much attention has been placed on the development of synthetically assembled FN fibers in a cell-free environment to study the biological, structural, and mechanical properties of FN. There are currently a number of strategies—including the use of denaturants[113,114], protein-surface interactions[38,121,122], and surface tension at the air-liquid interface[42,120,136]—that all involve unfolding FN dimers from a compact, globular conformation to a partially unfolded, fibrillar conformation to ultimately expose cryptic self-assembly sites. The exposure of these sites enables the formation of synthetically assembled FN fibers. This body of work demonstrates that nano- and microscale FN fibers can be assembled in a cell-free environment as long as cryptic self-assembly sites are first exposed.

One of the more utilized strategies, termed force-induced assembly, relies on the shear forces associate with pulling a sharp tip out of a concentrated FN solution and through the air-liquid interface. Vogel and coworkers have demonstrated that these microscale FN fibers can then be deposited onto either stretchable substrates[42,120,159] or microfabricated substrates[41,119] to enable the characterization of their

mechanical properties. Using this approach, it was found that these microscale FN fibers can support strains upwards of 700%[119]. It was further demonstrated that FN fiber strain can modulate the exposure of cryptic FN cysteine residues[119], availability of bacterial adhesion sites[42], and FN-collagen interactions[41]. By strategically labeling specific sites with donor and acceptor fluorophores for FRET imaging, it was concluded that strain induced the unfolding of the FN III modules[120,136]. However, there are limitations associated with FRET measurements and a direct characterization of the FN nanostructure with AFM could only reveal sub-fiber features when scanning the regions where the fibers were fractured[120].

Material-driven fibrillogenesis relies on the use of protein-surface interactions to assemble nanometer-scale FN fibrils. This approach has been demonstrated using poly(ethylacrylate) (PEA)[121,130], poly(hydroxyethyl acrylate)[131] and polysulfonated[122] surfaces. In each case, the nanostructure of the fibrils was resolvable using scanning electron microscopy (SEM) and/or atomic force microscopy (AFM). These studies have provided insight into how surface chemistry can modulate the conformation of FN fibrils and how these conformational differences can affect cell behaviors including adhesion[38,131] and differentiation[121]. However, this approach is limited by the fact that these fibrils are permanently bound to the surface thereby prohibiting a dynamic structural and/or mechanical characterization of the FN fibrils.

Using high resolution cryo-SEM and stochastic optical reconstruction microscopy (STORM) there has been investigation into the structure of individual FN molecules as well as cell-generated FN fibers. Electron microscopy of individual FN molecules revealed FN dimers have a contour length between 120-160 nm and can exist in extended and flexible conformations[132]. When applied to of FN fibers produced in cell culture, electron microscopy revealed that FN fibers can adopt both nodular and smooth morphologies[94], and through the use of immunogold labeling of the extra domain A, it was shown that FN molecules have a regular arrangement[134] when assembled into 5-20 nm thick fibers.

Following the development of STORM super-resolution microscopy, it was shown the FN molecules arranged into fibers by cells have a mean end-to-end distance of ~133 nm in which there is a 30-40 nm overlap between the N-termini of adjacent FN dimers within the fiber[160]. These studies have

revealed the structural properties of cell-generated FN fibers and provide a good comparison to determine the physiological relevance of FN fibers assembled under cell-free conditions.

In this study, we modified a surface-initiated assembly (SIA, chapter 2) technique[123,124] to engineer 1 cm long, 50 μm wide FN nanofibers that could be released from a dissolvable poly(N-isopropylacrylamide) (PIPAAm) substrate, strained, and then re-immobilized for high resolution structural analysis. To accurately measure FN strain, we developed a method to label the FN fibers with FN-based fiduciary marks. Using this approach, we found the FN nanofibers engineered using SIA can withstand strains comparable to what has been previously reported for SIA[125] and other techniques[119,120]. Further, by immobilizing the FN nanofibers in the strained state we were able to track how the nanostructure changes as a function of strain. Our measurements reveal that fully contracted FN nanofibers are comprised of large, densely packed nodules that become smaller with increasing strain. Furthermore, at high strains, the nanostructure is comprised of highly aligned nodules in a 'beads-on-a-string' arrangement. Our findings provide unique insight into how the morphology of FN assembled into fibers can be modulated by strain.

3.3. Materials and Methods

3.3.1. PDMS Stamp Fabrication

FN nanofibers were prepared by slight modification of the approach discussed previously in chapter 2[123,124]. Briefly, poly(dimethylsiloxane) (PDMS) stamps patterned with either 1 cm long, 50 μm wide raised lines or 1 cm long, 10 μm wide raised lines were fabricated by first spincoating glass wafers with SPR 220.3 positive photoresist (Microchem). The photoresist was then exposed to UV light through a photomask and developed using MF-319 developer (Microchem). A negative of the patterned photoresist wafer was formed by casting PDMS prepolymer (Sylgard 184, Dow Corning) over it and curing it at 65° C for 4 hours. The cured PDMS was then peeled off the glass wafer and 1 cm^2 stamps were cut out.

3.3.2. Engineering FN Nanofibers with FN-Based Fiduciary Marks

FN nanofibers were tagged with fluorescently labeled, FN-based fiduciary marks (Fig. 3.1) by combining surface-initiated assembly[123,124] (SIA, see chapter 2) with a Patterning-on-Topography[161] (PoT, see chapter 4 for complete discussion of PoT) technique (Fig. 3.1). First, we cleaned PDMS stamps with 10 μm wide, 1 cm long raised features by sonication in a 50% ethanol solution for 30 minutes. Following sonication, the stamps were dried under a stream of nitrogen and then incubated with FN from human plasma (BD Biosciences) for 60 minutes at a concentration of 50 μg/mL in distilled water where 40% of the FN was conjugated to an Alexa Fluor 488 dye (Life Technologies). After incubation, the stamps were washed, dried under a stream of nitrogen and then brought into conformal contact with poly(N-isopropylacrylamide) (PIPAAm) coated coverslips for 15 minutes (Fig. 3.1a). The PIPAAm coated coverslips were prepared by spincoating a 10% PIPAAm (Polysciences Inc.) in 1-butanol (w/v) solution. Upon removal of the stamps, the fidelity of the transfer of the 10 μm wide FN lines to the PIPAAm coated coverslips was inspected using phase contrast microscopy.

Following microcontact printing, a second PDMS stamp with 50 μm wide and 1 cm long raised features was coated with a 50 μg/mL solution of FN dissolved in distilled water (Fig. 3.1b). The stamp was then washed to remove excess FN, dried under a stream of nitrogen and subsequently brought into conformal contact orthogonal to the PIPAAm coated coverslip containing the 10 μm wide FN lines (Fig. 3.1c). With the stamp still in conformal contact, the PIPAAm was hydrated with warm, 40° C, distilled water and allowed to cool below the LCST of PIPAAm thereby releasing the fluorescently labeled, 10 μm wide FN lines off of the PIPAAm onto the PDMS stamp which was pre coated with FN. The stamp was then removed, washed in distilled water, dried under a stream of nitrogen and then brought into conformal contact with a new PIPAAm coated coverslip for 10 minutes to create arrays of 1 cm x 50 μm FN lines with 10 μm wide and 10 μm spaced fiduciary marks (Fig. 3.1d).

3.3.3. FN Nanofiber Straining Experiments

To strain FN nanofibers, we first microcontact printed 1 cm long and 50 μm wide lines of FN that have been tagged with fiduciary marks as described above. Next, we prepared PDMS pads by casting PDMS prepolymer over a glass slide and curing it in an oven set to 65° C for 4 hours. Once cured we cut out 2 PDMS rectangles that were ~1 cm long and ~5mm wide and placed them at opposite ends on top of the FN nanofibers on PIPAAm. We then attached the PDMS pads to a pair of micromanipulators by applying a small drop of high strength epoxy (Devcon) to the top of the pads, bringing the manipulator tips in contact with the epoxy, and allowing the epoxy to harden for at least 30 minutes (Fig. 3.2a). Once the epoxy hardened, we triggered the thermal dissolution of PIPAAm by hydration and subsequent cooling below the lower critical solution temperature (LCST) of PIPAAm which led to the assembly and release of the nanofibers off of the PIPAAm and onto the PDMS pads. This resulted in FN fibers that were tethered at each end to a PDMS pad and freely suspended in between. The FN nanofibers were strained by moving the micromanipulators in opposite directions (Fig. 3.2.b) and subsequently immobilized back onto the coverslip once a given strain was reached. To calculate strain, we used the center-to-center fiduciary mark distance of a released and fully contracted FN nanofiber as the initial

length and the center-to-center fiduciary mark distance of the strained FN nanofibers as the final length. Strain experiments were performed on top of an inverted epifluorescent microscope (Eclipse Ti, Nikon Instruments) with mounted micromanipulators (Transferman NK2, Eppendorf).

3.3.4. Analyzing Nanofiber Structural Morphology Using AFM

AFM (MFP3D-Bio, Asylum Research) was used to analyze the nanostructure and quantify the morphology of FN nanofibers at low, intermediate, and high strain states. The FN nanofibers were scanned in air using AC mode with AC160TS cantilevers (Olympus Corporation). After each fiber was strained, it was immobilized back onto the coverslip, washed three times with distilled water to remove the dissolved PIPAAm, and then dried in a 40° C oven. The FN nanofibers were first scanned at low resolution with a scan area of 20 μm to 30 μm and a points and lines of 515 x 512. We then increased the resolution by decreasing the scan size to 3 μm x 3 μm with a points and lines of 1024 x 1024. For analysis, we used the high resolution 3 μm x 3 μm scans. The nodule size and the FN surface coverage were quantified using the IGOR Pro software environment (WaveMetrics) using the AFM height channel. To quantify surface coverage, we applied a mask to the fibrils within the nanostructure and measured the area occupied by the masked regions divided by the total area for the image. This was only performed on the high resolution, 3 μm x 3 μm to allow us to include the smallest fibrils within the mask. Nodule diameter was performed also using the IGOR Pro software environment. Briefly, a line was drawn over each nodule to generate a cross-sectional profile based on the height information of each pixel along the line. In these cross-sectional profiles, each nodule typically produced a peak. The width of each peak was measured to produce the diameter for each nodule.

3.4. Results

3.4.1. FN Nanofibers Can Withstand Over 7-Fold Extensions

The mechanical properties of FN fibers have been previously studied using microfabricated substrates in combination with MEMS force sensing tips[119] as well as with calibrated microneedles[125]. These studies both confirmed that FN fibers are capable of withstanding large, 8-fold extensions before failure. Specifically, with similar FN nanofibers prepared using SIA it was shown that these fibers undergo three strain-specific elongation regimes that correlate to conformational unfolding, domain unfolding, and strain stiffening. Since our main goal was to investigate how the nanostructure changes with strain, we engineered FN nanofibers that were 50 μm wide and 1 cm long to ensure that they would maintain a single layer without folding over during stretching. This ribbon-like morphology ensures we can resolve the nanostructure with high resolution. Further, unlike previous studies, which used MEMS tips and calibrated glass microneedles, we used PDMS pads in combination with micromanipulators to strain the FN nanofibers (Fig. 3.2a). Since the nanofibers were 1 cm long, out of the field of view of our microscope, we first developed a strategy to label the FN nanofibers with fluorescent, FN-based fiduciary marks so that we could accurately measure the nanofiber strain (Fig. 3.1). To do this, we combined SIA[123,124] with a modified Patterning-on-Topography (PoT) technique[161] by (1) microcontact printing 10 μm wide lines of fluorescently conjugated FN onto PIPAAm (Fig. 3.1a); (2) coating a second PDMS stamp with FN (Fig. 3.1b); (3) bringing the FN coated stamp into conformal contact and orthogonal to the 10 μm wide FN lines on PIPAAm (Fig. 3.1c); (4) dissolving the PIPAAm through hydration and reduction of the solution temperature below the LCST of PIPAAm (~32° C) to release the 10 μm wide lines onto the PDMS stamp; and (4) microcontact printing the FN-coated, PoT-printed PDMS stamp onto a new PIPAAm coated coverslip. The resulting FN nanofibers had 10 μm wide and 10 μm spaced fluorescent FN fiduciary markers (Fig. 3.1d). Next, to strain the FN nanofibers, we cut 1 cm long, 5 mm wide and 1 cm thick PDMS rectangles and placed them on each end of the FN nanofibers. We then

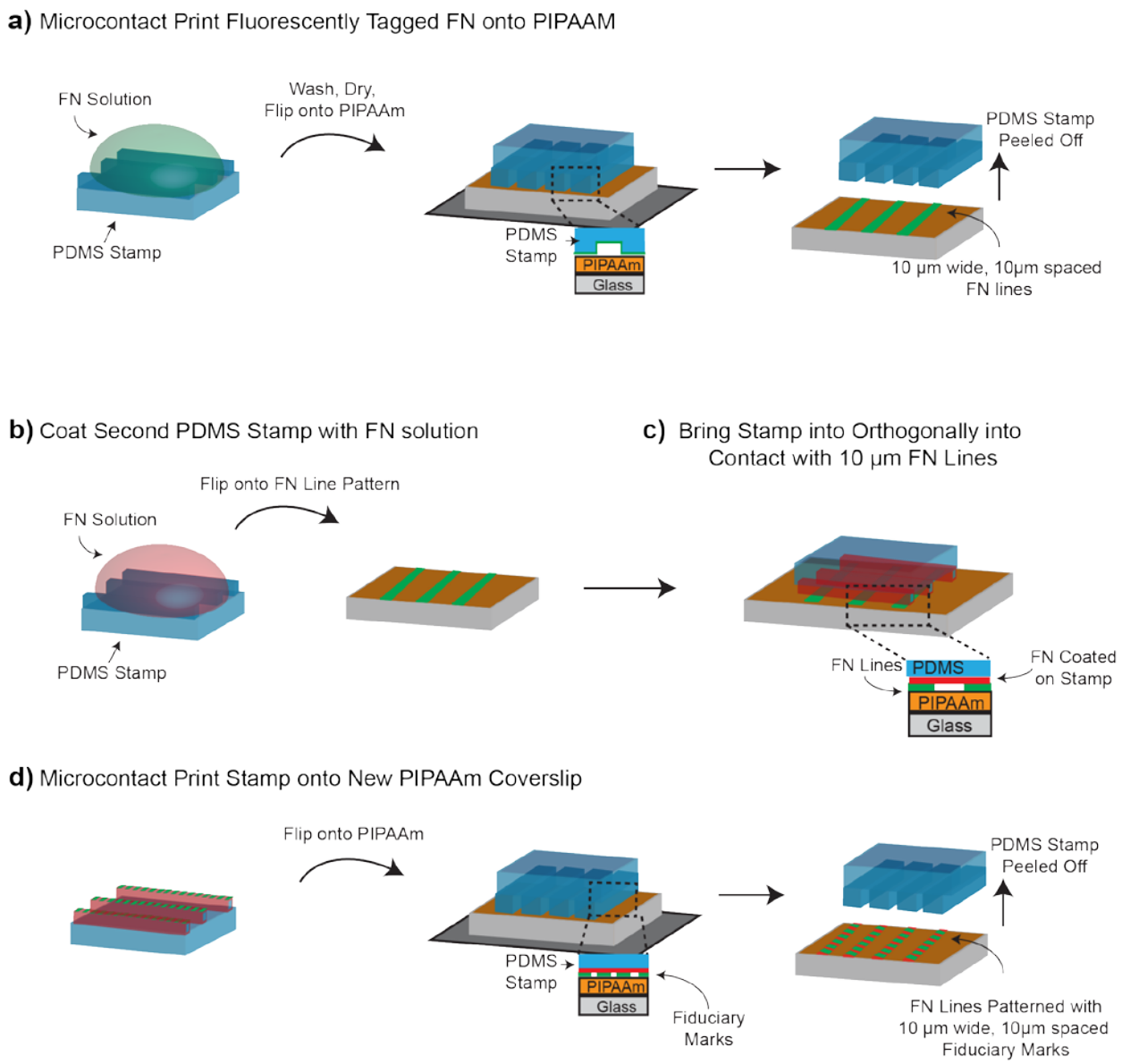

Fig. 3.1. Preparation of FN nanofibers with FN-based fiduciary marks. (a) 10 µm wide, fluorescently conjugated FN lines were first microcontact printed onto a PIPAAm coated coverslip. (b) A second PDMS stamp was coated with FN and (c) brought orthogonally into conformal contact with the 10 µm wide FN lines on PIPAAm. The 10 µm wide lines were released onto the FN coated stamp through the dissolution of PIPAAm. (d) The FN coated PDMS stamp with 10 µm wide FN lines adsorbed was then microcontact printed onto a new PIPAAm coated coverslip.

attached micromanipulator tips to the PDMS supports using epoxy glue and allowed it to harden (Fig. 3.2a). We subsequently released the FN nanofibers off of PIPAAm and onto the PDMS supports such that the fibers were freely suspended (Fig. 3.2b). Once the FN nanofibers were attached to the PDMS

supports, we used the micromanipulators to uniaxially strain the FN nanofibers. After a specific strain was reached, we immobilized the FN nanofibers in their strained state back down onto the coverslip by lowering the PDMS supports. Using AFM we were able to resolve the nanostructure of the FN nanofibers.

We have previously shown that, in the as-patterned pre-release state, the FN nanofibers are under an inherent pre-stress and undergo 3.3-fold decrease in length upon release (Fig. 2.2c, 2.3d). Therefore we first wanted to confirm that the 1 cm long, 50 μm wide FN nanofibers were under a similar pre-stress. To do this, we first measured the center-to-center distance of the fiduciary marks on FN nanofibers pre-release on the PIPAAm surface (Fig. 3.2c). We then only tethered one side of the nanofibers, released them through dissolution of PIPAAm and allowed them to fully contract in solution (Fig. 3.2d). From pre-release to post-release, the center-to-center distance of the fiduciary marks decreased from 20.10 ± 0.64 μm to 10.76 ± 0.48 μm, a ~2-fold change in length. Moving forward, we used the center-to-center distance of the fiduciary marks in the fully contracted FN nanofibers (10.76 μm) as the initial length when calculating strain.

With the FN nanofibers attached to the PDMS supports, we first simply lowered the nanofibers back down onto the coverslip. This correlated to center-to-center fiduciary mark distances of 16.87 ± 1.68 μm indicating a ~56% strain relative to the fully contracted state (Fig. 3.2e). Note that this distance doesn't fully match up with the fiduciary mark distance of FN nanofibers pre-release because the PDMS supports did not moved slightly inward instead of straight down. We then uniaxially strained the FN nanofibers to achieve fiduciary mark center-to-center distances of 51.33 ± 3.82 μm and 78.77 ± 2.56 μm correlating to 4.77-fold and 7.32-fold extensions, respectively (Fig. 3.2e). This is comparable to what previous studies involving FN fiber tensile testing using calibrated glass microneedles[125] and MEMS tips[119] to strain FN fibers.

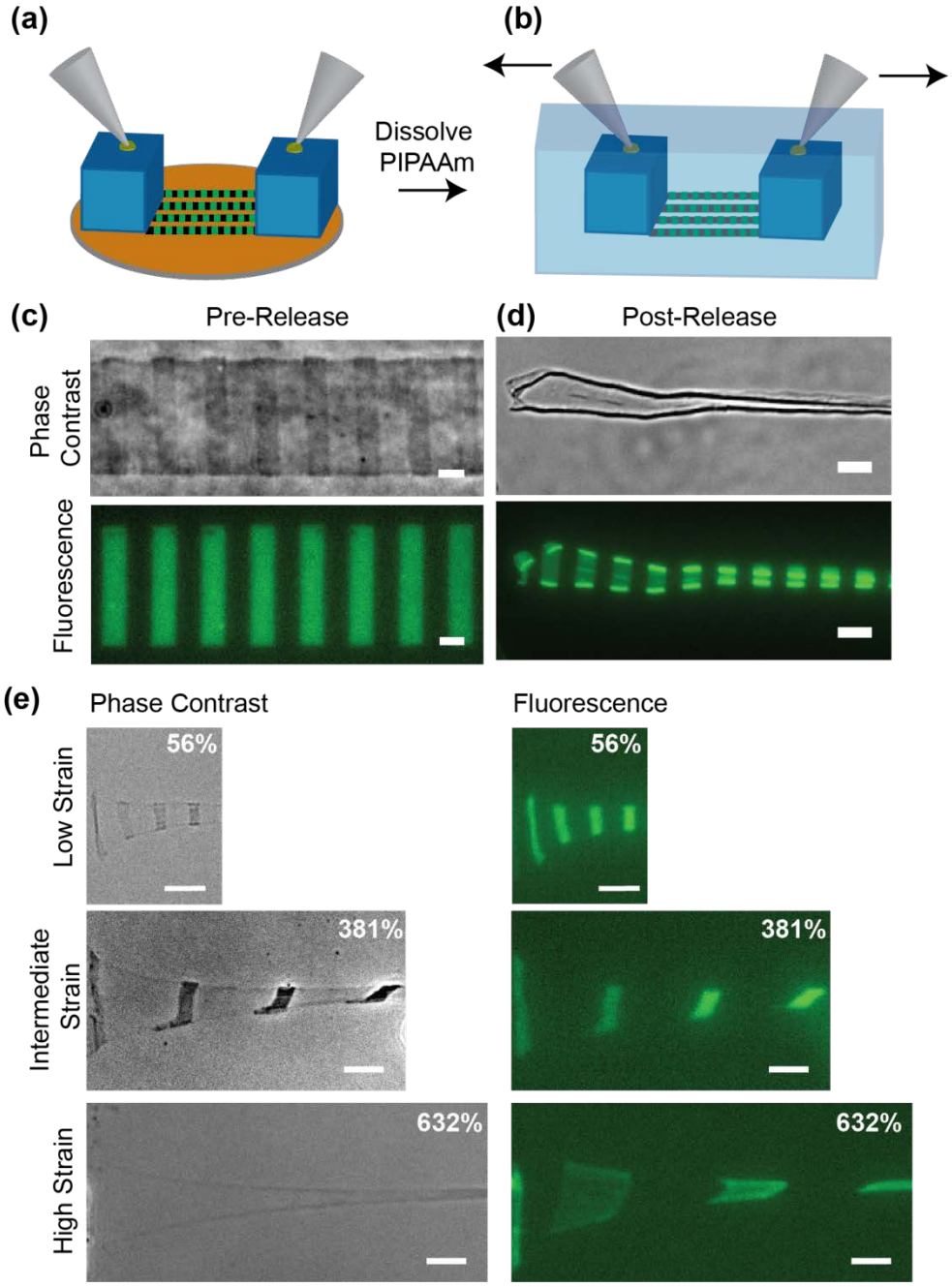

Fig. 3.2. Using fiduciary marks to measure FN strain. (a) Schematic of the straining apparatus where PDMS supports are placed on opposite ends of 1 cm long FN nanofibers. Micromanipulators are then attached to the PDMS supports using high strength epoxy. (b) After hydration and thermally triggered dissolution of PIPAAm, the FN nanofibers release onto the PDMS supports where they are freely suspended in between. (c) Phase contrast and fluorescent image of a FN nanofiber pre-release with 10 µm wide, 10 µm spaced fiduciary marks. The center-to-center distance of the fiduciary marks was 20.10 ± 0.64 µm. (d) Phase contrast and fluorescent image of a FN nanofiber post-release where the center-to-center distance of the fiduciary marks decreased to 10.76 ± 0.48 µm. (e) FN nanofibers were subjected to low, intermediate, and high strains as indicated by the separation of the fiduciary marks. Scale bars are (c and d) 10 µm and (e) 20 µm.

3.4.2. The Nanostructure of Nanofibers Under Low Strain is Comprised of Large Nodules

Our main focus was to investigate whether the nanostructure within the FN nanofibers was dependent on nanofiber strain. We previously demonstrated that the fibrillar-nodular transition within the nanostructure was a major driving force behind the large strains observed during the SIA process (Fig. 2.5). However, in previous work we were limited to analyzing the nanostructure between only the pre-release and post-release states. We had previously found that the nanostructure of fully contracted nanofibers was comprised of elliptically-shaped nodules that were several times larger than the expected diameter of a single FN dimer in a compact, solution form (~51x32 nm[156]). From this, we hypothesized that strain would first induce the separation of the large nodules into smaller nodules which, upon further strain, would then unfold into a fibrillar morphology reminiscent of the pre-release state (Fig. 2.5b).

To determine whether the nanostructure of fully relaxed FN nanofibers was different than the 50 μm x 20 μm rectangles used previously, we used AFM to scan a 20 μm x 20 μm subsection of the 1 cm long, 50 μm wide nanofibers that had been allowed to fully contract in solution (Fig. 3.3a). At high resolution, it is clear that the nanostructure is comprised of large nodules (Fig. 3.3.b) in an overall isotropic arrangement. Analysis of the nodule diameter indicates that these nodules had an average diameter of 107.11 ± 29.43 nm (Fig. 3.3c). This diameter is comparable to the diameter of the nodules found in the interior of fully contracted, 50 μm x 20 μm FN rectangles (Fig. 2.5f, g, and h). Next, we scanned FN nanofibers that had a fiduciary mark center-to-center distance of 20.84 ± 1.12 μm, a ~94% strain relative to the fully contracted nanofibers (Fig. 3.3.d). This was accomplished by releasing the nanofibers onto the PDMS supports and immediately lowering them back down onto the coverslip. At high resolution (Fig. 3.3.e) it was clear that the nanostructure was still dominated by the presence of nodules although they were markedly smaller with an average diameter of 72.88 ± 18.69 nm (Fig. 3.3f). This diameter is still larger than the nodules observed using cell-free assembly techniques yet it is closer to the expected diameter for a single FN dimer in a compact conformation.

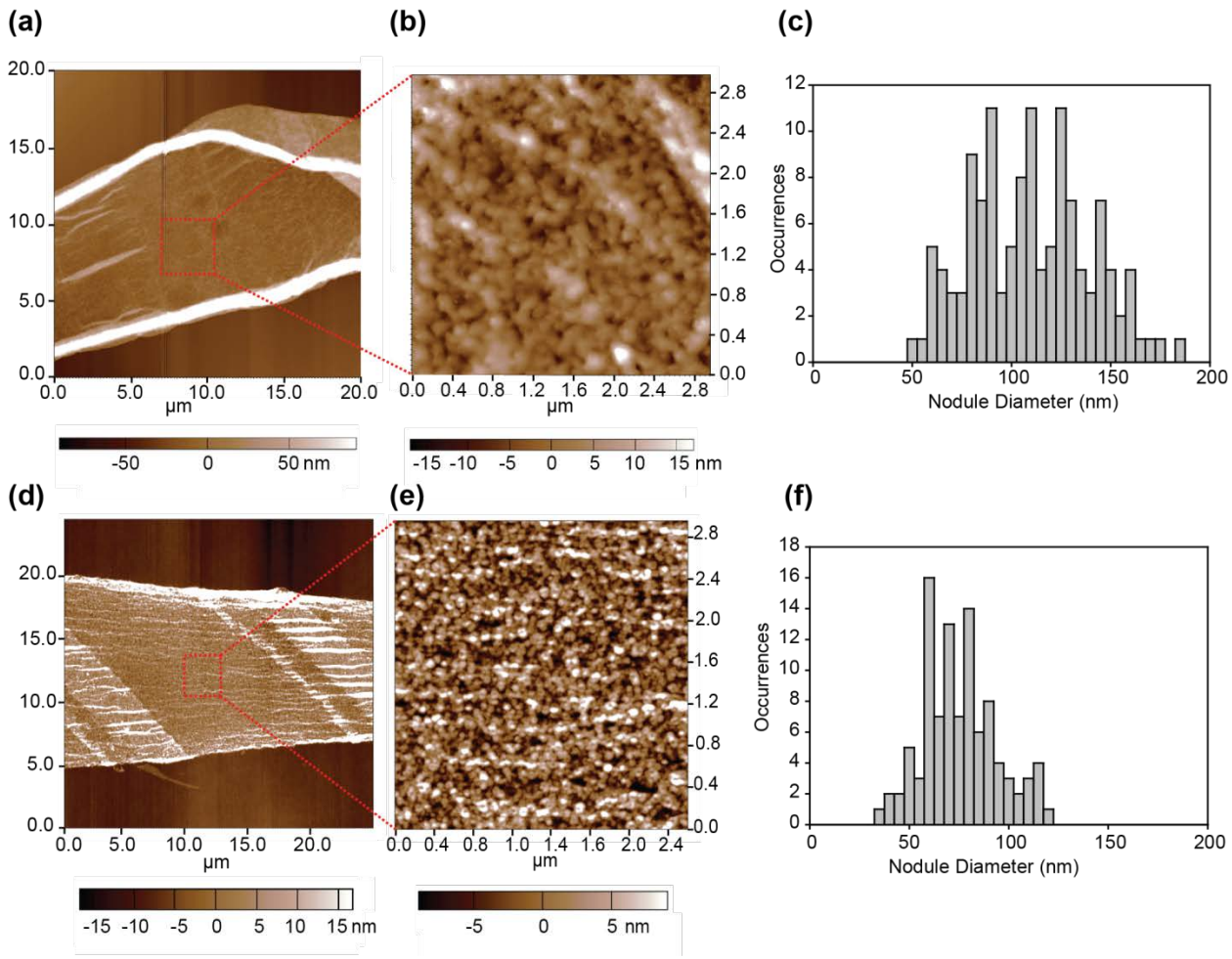

Fig. 3.3. Investigating the nanostructure of fully contracted and minimally strained FN nanofibers. (a) A representative FN nanofiber that was allowed to fully contract in solution prior to AFM imaging. (b) A higher resolution scan of the nanofiber in (a) indicates that the nanostructure consists mainly of large, isotropic nodules. (c) The nodules in fully contracted FN nanofibers had an average diameter of 107.11 ± 29.43 nm, consistent with previous findings using smaller FN nanofibers. (d) A representative low resolution AFM scan of a FN nanofiber strained to 94% relative to the fully contracted state. (e) A higher resolution scan of the nanofiber in (d) shows a mostly isotropic, nodular network, (f) yet these nodules had an average diameter of 72.88 ± 18.69 nm.

3.4.3. The Nodular Diameter Decreases with Strain

Further increasing the strain to center-to-center fiduciary mark distances of 39.76 ± 1.12 µm (Fig. 3.4a, 269.52% strain), 51.33 ± 3.82 µm (Fig 3.4b, 377.04% strain), and 117.40 ± 5.96 µm (Fig 3.4c, 664.82% strain) revealed the presence of an overall fibrous nanostructure whereby the fibrils were anisotropically aligned in the direction of the applied load. It is important to note that the fiduciary marks for Fig. 3.4c were prepared using a different stamp and had a center-to-center distance of 29.34 ± 1.57

μm. The fiduciary mark center-to-center distance of these FN nanofibers in a fully contracted state was 15.35 ± 0.30 μm and was therefore used as the initial length.

In order to resolve the structural details of the aligned fibrils, we increased the resolution of the AFM by decreasing the scan area to ~3 μm x 3 μm. At this scale, it is clear that FN nanofibers strained to 269% were comprised of thick fibrils with an apparent nodular structure (Fig. 3.4d). Interestingly, it is clear that the thick bundles became increasingly smaller (Fig. 3.4d, inset) at specific points. Similarly, for FN nanofibers strained to ~377% and ~664% there was also an apparent nodular nanostructure (Fig. 3.4e, f) yet along a given fibril, these nodules became smaller and transitioned into smooth segment (insets, Fig. 3.4e and f, respectively). This is similar to what has been reported for cell-generated FN fibers using SEM[94]. FN nanofibers strained to ~269% were found to have an average nodule diameter of 46.70 ± 14.12 nm (Fig. 3.4g). FN nanofibers strained to ~377% and ~664% were found to have larger average nodule diameters than nanofibers strained to ~250% with mean diameters of 56.88 ± 20.23 nm (Fig. 3.4h) and 53.49 ± 22.81 nm (Fig. 3.4i), for ~377% and ~664% strains, respectively. We attributed this increase in nodule diameter to the constituent fibrils breaking during large strains causing them to adopt a more compact, globular conformation. When comparing the average nodule diameters for each strain state, we found that the mean nodule diameter significantly decreased from 107.11 ± 29.43 nm for full contracted FN nanofibers to 46.70 ± 14.12 nm for FN nanofibers strained to ~269%, about a 2.3-fold decrease in average diameter (Fig. 3.5a). During the transition from fully contracted to highly strained, we also measured the surface coverage of the constituent FN fibrils. We found that as the nanofibers were stretched, there was a noticeable decrease in the surface coverage of the constituent fibrils (Fig. 3.5b). For example, fully contracted FN nanofibers had an average surface coverage of 87.39% while after straining the FN nanofibers to ~100%, the surface coverage of the constituent FN molecules decreased to 80.4%. At higher strains, we observed a sharper decline in the FN surface coverage from 55.1% for nanofibers strained to 269% to 33.77% for nanofibers strained to 377%. Finally, at maximum strain, the surface coverage was 34.86%. Altogether, it is clear that with increasing strain, the nodule size decreased

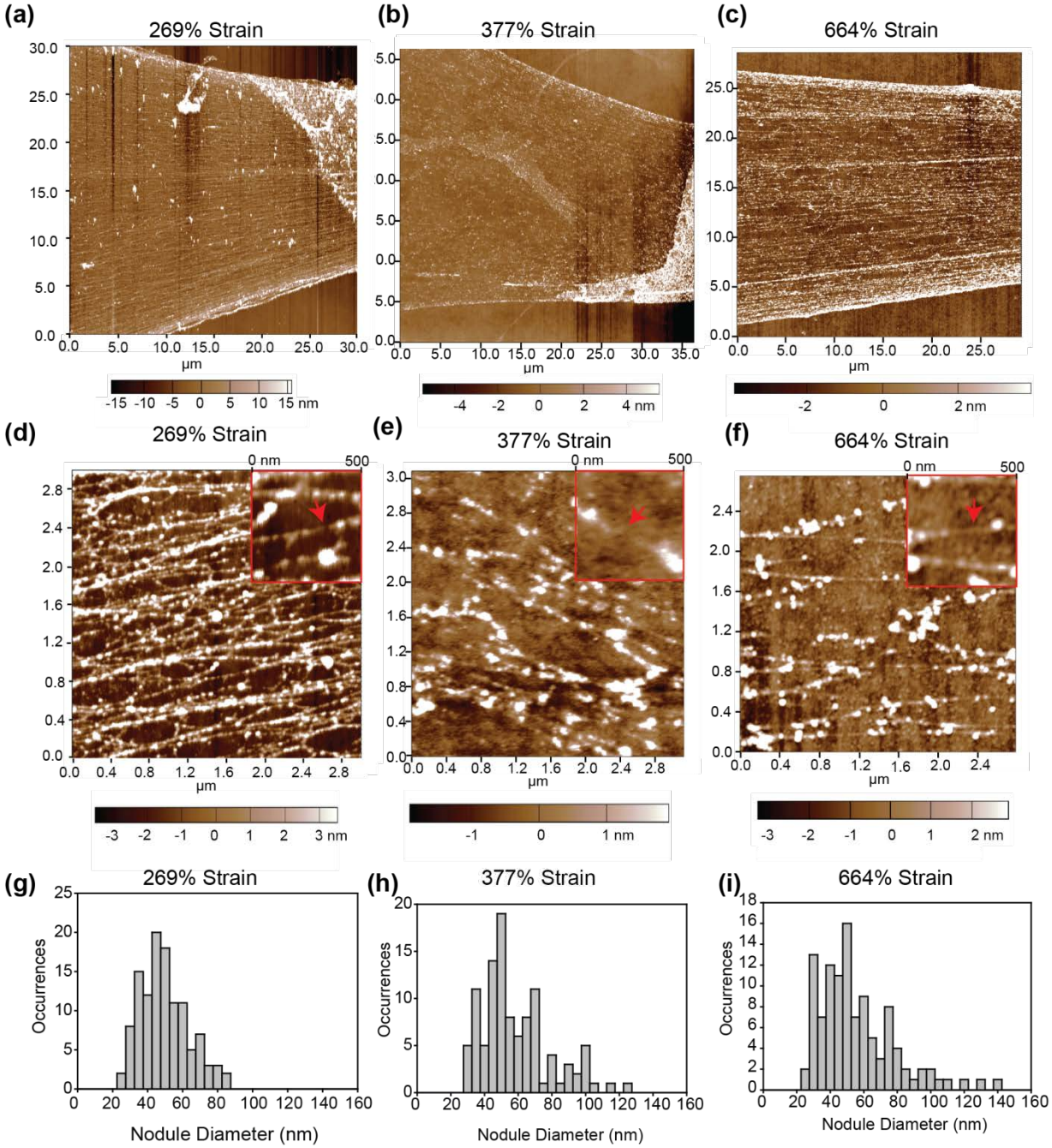

Fig 3.4. Investigating the nanostructure of highly strained FN nanofibers. FN nanofibers were strained to (a) 269%, (b) 377%, and (c) 664% relative to the fully contracted state and scanned using AFM. High resolution scans were also acquired for fibers strained to (d) 269%, (e) 377%, and (f) 664%. Insets show zoomed in regions to highlight (d) thicker fibrils becoming increasing smaller and (e, f) regions where the nodular morphology transitioned to a smooth morphology. Analysis of the nodule diameter demonstrates that fibers strained to (g) 269% had a mean nodule diameter of 46.70 ± 14.12 nm whereas fibers strained to (h) 377% and (i) 664% had mean nodule diameters of 56.88 ± 20.23 nm and 53.49 ± 22.81 nm, respectively.

until the strain became high enough that the constituent fibril strands begin to break and reform larger nodules. With increasing strain there was also a measureable decrease in the FN surface coverage.

3.4.4. Highly Strained FN Nanofibers Have a Variable Nodular Nanostructure

Since there was a large decrease in the mean nodule diameter around 269% strain, we optically zoomed in on the high resolution AFM scans to detect sub-fibril features and compared this to FN nanofibers that have been strained to ~664% (Fig. 3.6). At high resolution, it is evident that a nodular structure still persists in a 'beads-on-a-string' configuration (Fig. 3.6.a). While recent reports investigating cell-generated FN fibers[160] and FN fibers assembled on polysulfonate surfaces[122] reported the presence of highly periodic, sub-fibril nodules, we found that the periodicity and nodule diameter varied even along single fibrils. Although there was a large variability in the subfibril nodules, we did notice regions where there was short range periodicity. For example, there were regions where larger nodules would transition into clusters of nodules that were ~32 nm in diameter with an average periodicity of 41.11 ± 5.14 nm (Fig. 3.6b). Moreover, the height of these nodules ranged from ~2-4 nm, down from about 10-15 nm for the height of the nodules in fibers strained to 94%. In addition to the periodic subfibril nodules, we also observed segments that spanned between two nodules that had a mostly smooth appearance (Fig. 3.6.c). These segments had heights that varied between 0-2 nm. Further investigation is needed to confirm that this nodule-fibril transition corresponds to FN dimer unfolding.

Next, we analyzed the nanostructure of FN nanofibers that were strained to 664% relative to the fully contracted state (Fig. 3.6.d). Similar to FN nanofibers that were stretched to 269% strain, the constituent fibrils within the nanofiber still maintained a nodular nanostructure arranged in a beads-on-a-string conformation. These nodules were also highly variable in size without a long range periodicity. However, the nanostructure also contained regions in which larger nodules transitioned into smooth segments with a sparse arrangement of nodules that were 24.44 ± 3.99 nm in diameter. These nodules were smaller than those observed for FN nanofibers strained to 269% and were spaced further apart.

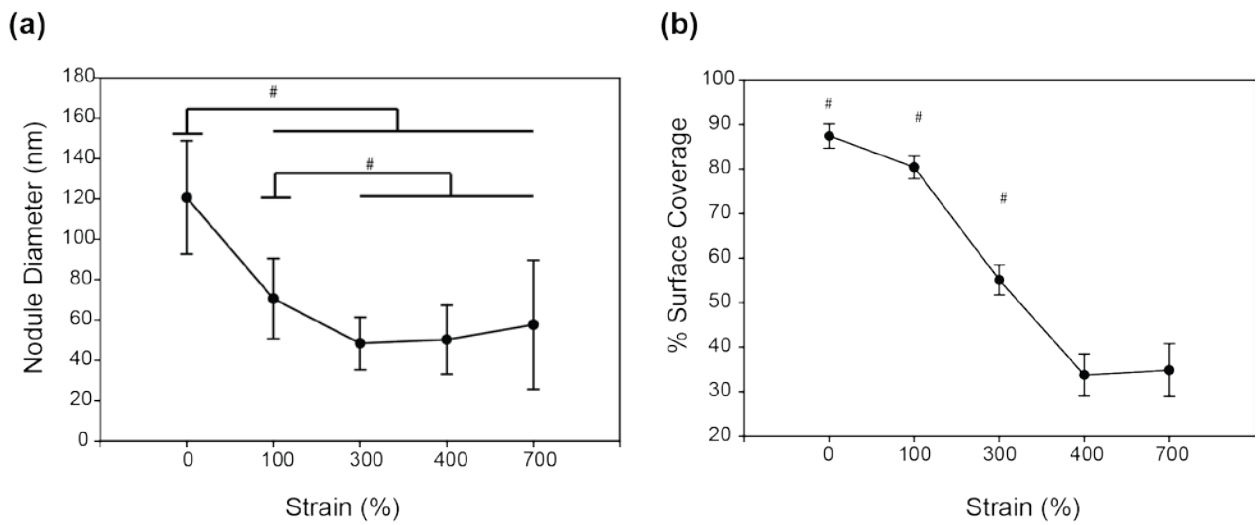

Fig 3.5. Measuring nodule diameter and FN surface coverage as a function of strain. (a) Mean nodule diameter. Error bars are standard deviation and the symbol # indicates a statistically significant difference with $P < 0.05$ using an ANOVA rank sum test with a Dunn's pairwise comparison. (b) Percent of FN molecule coverage as a function of strain. The symbol # indicates a statistically significant difference from the other points with $P<0.05$ using a one-way ANOVA rank sum test with a Dunn's pairwise comparison.

Unlike FN fibers assembled onto surfaces, we found that the nanostructure of strained nanofibers was variable where larger nodules progressively transition into regions of smaller, periodic nodules.

3.5.0. Discussion

In this study, we examined how the nanostructure of FN nanofibers changes as a result of strain. We were able to overcome the barriers present in prior work which investigated the nanostructure of FN fibrils assembled via protein-surface interactions on different surface chemistries[38,121,130,131]. While these studies could track FN morphology on different surface chemistry and, particularly on negatively charged polysulfonate surfaces[122], measure the size and arrangement of sub-fibril nodules, they were limited to studying the FN nanostructure in a single state as the FN fibrils were permanently bound to the surface. To overcome this barrier we used a SIA technique, which enables FN nanofibers to be released from a

dissolvable, PIPAAm surface. By capturing the released FN nanofibers using micromanipulators mounted to PDMS supports, we were able to uniaxially strain the FN nanofibers from fully contracted to highly

Other groups have reported the mechanical properties of FN fibers through tensile testing with either MEMS force sensing tips[119] and calibrated microneedles[125]. In these experiments, the entire 8-fold strain could be tracked within the field of view of a microscope. Due to the bulky nature of the PDMS supports, it was difficult track the entire fiber extension within the field of view of the microscope, even at low magnification. Compounding the issue was the need for higher magnification imaging to confirm that the FN nanofibers suspended between the PDMS supports were still intact during straining. This necessitated the need to tag the FN nanofibers with fiduciary marks. A review of literature revealed several methods for creating fiducial marks on protein-based systems. Klotzsch et al used a method to photobleach fluorescent FN fibers in a precise, defined manner[119]. However, this was limited to a small area and may not be suitable for our high throughput approach. In another approach, graphite powder was applied to fibrin gels to measure their strain during tensile testing[155]. However, these fibrin gels were on a scale of several mm in diameter, therefore applying graphite powder to 50 μm wide FN nanofibers would be technically challenging and may potentially disrupt the properties of the FN nanofibers.

Instead, we labeled the 50 μm wide, 1 cm FN nanofibers with 10 μm wide, 10 μm spaced fluorescent FN-based fiducial marks through the use of a recently published PoT approach[161] in combination with SIA. Using this approach, we could add fiduciary marks to the FN nanofibers with high precision and little fiber-to-fiber variability (Fig. 3.2). It is important to note that the degree of integration between the fiduciary marks and the underlying FN nanofibers is currently unclear. Therefore, in this study, we measured the center-to-center distance instead of the distance between the edges of the fiduciary marks. Finally, while not investigated here, width and spacing of the fiduciary marks can be adjusted, thereby making them more sensitive to regional differences in nanofiber strain. This would allow us to measure the strain associated within different sub-regions of the FN nanofibers instead of just the overall strain (See chapter 4).

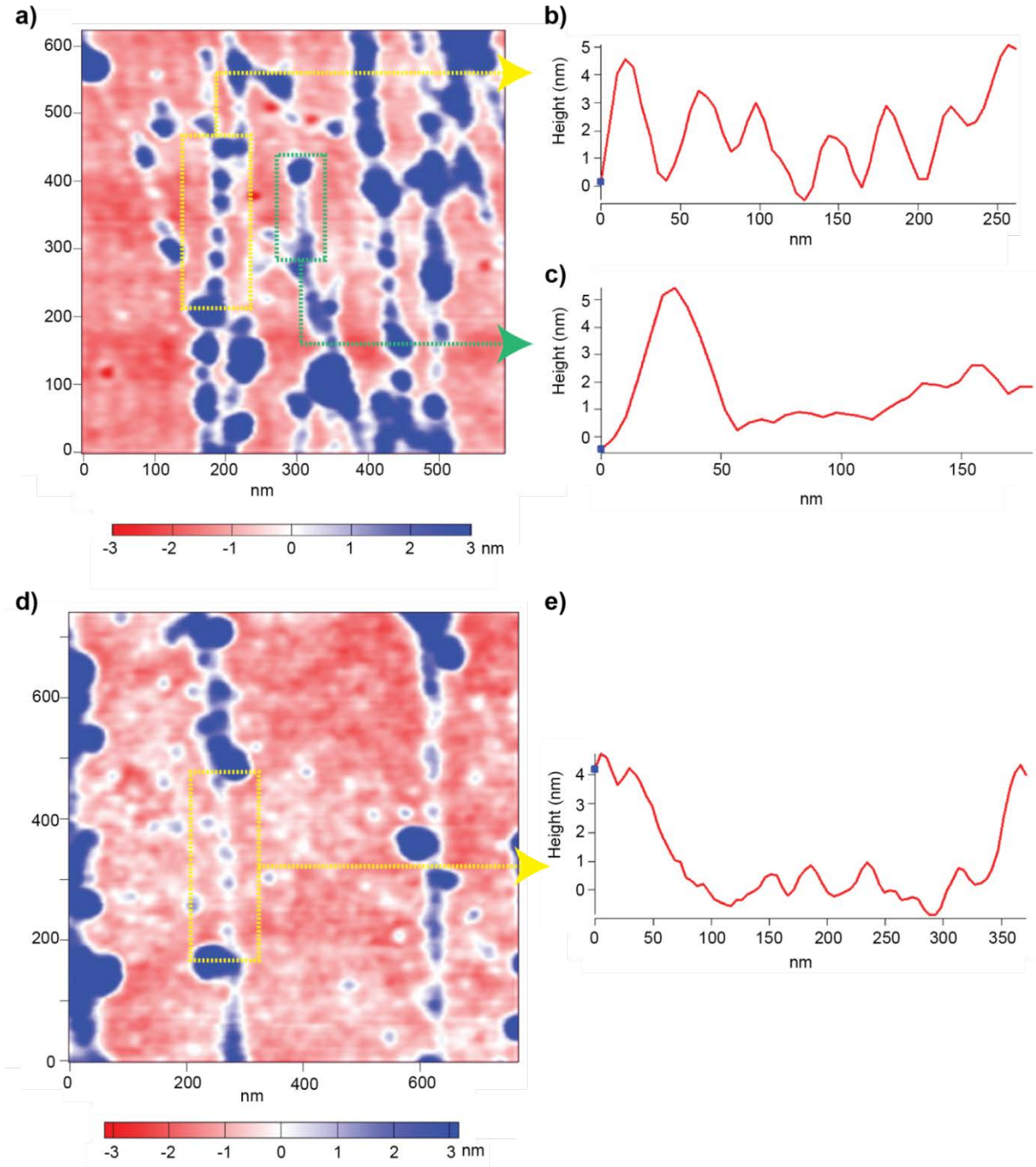

Fig. 3.6. Investigating the subfibril features of FN nanofibers strained to 269% and 664%. (a) A representative optical zoom from a 3 µm x 3 µm scan of a FN nanofiber strained to 269%. (b) A cross-sectional profile from (a) reveals that some fibrils had a short range periodic nodular structure with an average nodule diameter of 31.86 ± 5.63 nm and a periodicity of 41.11 ± 5.14 nm. (c) An additional cross-sectional profile from (a) indicating that FN fibrils also could transition from nodular to smooth morphologies. The length of the smooth segment was 75.91 nm. (d) A representative optical zoom from a 3 µm x 3 µm scan of a FN nanofiber strained to 664%. (e) A cross-sectional profile from (d) indicating that segments contained subfibril nodules with a mean diameter of 24.45 ± 3.99 nm and a nodule-to-nodule spacing of 34.22 nm, 48.89 nm, and 78.22 nm.

Understanding the nanostructure and molecular arrangement of FN dimers into fibers has been of considerable interest to further our knowledge into how FN can be manipulated and deformed to expose cryptic binding sites. Our group as well as others have identified that both FN molecules and FN fibers assembled with and without cells contain a nodular nanostructure[94,122,132,133,161]. For example, FN fibrils formed on negatively charged, polysulfonate surfaces formed 1 μm long fibrils where each fibril contains nodules in a bead-on-a-string arrangement[122]. These nodules were highly periodic, with a nodule-nodule spacing of 60 nm leading to the conclusion that these nodules were the result FN dimers aligning in a staggered manner with an overlap between the first seven FN type III modules of each FN dimer. This conformation was determined to be initially driven by electrostatic interactions between FN and the negatively charged surface and eventually, further stabilized by FN-FN interactions. A separate study used STORM super-resolution microscopy to measure the short range periodicity of cell-generated FN fibers[160]. From these experiments it was concluded that FN fibers assembled by cells have a periodicity of ~95 nm which arises from a 30-40 nm overlap between the first five FN type I modules on the N terminus of adjacent FN dimers. Finally, the use of electron microscopy on cell generated FN fibers revealed the presence of both nodular and smooth regions, where the smooth regions represent regions of the FN fiber that were under tension[94]. From these studies, it is clear that FN can form different molecular arrangements that depend on FN-FN interactions, and presumably tension.

Since we had the ability to strain and subsequently immobilize FN fibers in the strain state, we wanted to determine how the nanostructure of the nanofibers changed as a function of strain. FN nanofibers that were released and allowed to fully contract in solution served as the initial center-to-center fiduciary mark distance for strain experiments (Fig. 3.2b). Analysis of the nanostructure revealed the presence of large nodules with an average diameter of 120.64 ± 28.01 nm (Fig. 3.3c). This diameter is appreciably larger than the diameter of nodules observed in cell generated FN fibers[94] and FN fibers formed on polysulfonate surfaces[122] and microfabricated PDMS surfaces[115]. Since this diameter is also larger than the diameter of single FN dimers in a compact, globular conformation, we reason that these

nodules are comprised of several compact FN dimers clustered together. This is further supported when examining the nanostructure of FN nanofibers in an as-patterned, pre-release state (Fig. 2.5b). In this state, the nanofibers are composed of an isotropic network of elongated fibrils with a large degree of overlap. We proposed that this promotes sufficient FN-FN interactions upon release to assemble into a fiber. Since the FN fibrils are no longer 'pinned' to the surface by protein-surface interactions, many FN dimers are able to contract into a globular conformation within close proximity to one another. It would be interesting to see if FN fibers in cell culture are capable of obtaining such structures when the fibers are broken and no longer under cell-mediated tension.

By releasing the FN nanofibers onto the PDMS supports and immediately immobilizing them back down onto the coverslip the nanofibers obtained a strain of a 94% relative to the fully contracted state. The act of holding the FN nanofibers under tension resulted in a significant decrease in nodule diameter to 70.59 ± 19.87 nm (Fig. 3.3f). This nodule diameter is reasonably comparable to the size of single FN dimers in a compact, globular conformation[156].

By increasing the nanofiber strain, we found that the average nodule diameter decreases up until about 269% at which it slightly increases. We attributed this slight increase in nodule diameter to constituent FN fibrils breaking during strain and contracting into a globular conformation. While we acknowledge that a more exhaustive investigation that covers many more strains is needed, these results indicate that while the FN nanofibers can withstand strains upwards of 664%, constituent fibrils can begin to break within the nanostructure at much lower strains.

Finally, zooming in on the AFM images of the FN nanofibers that were strained to 269% (Fig. 3.6a) and 664% (Fig. 3.6d) relative to the full contracted length revealed that the nanostructure is still nodular albeit highly irregular. For FN nanofibers strained to 269%, the nodules were arranged in a 'beads-on-a-string' morphology where large nodules would progressively get smaller to ~32 nm. In these regions, the smaller nodules adopted a short range periodic structure of with an average nodule-nodule distance of 41.11 ± 5.14 nm. These nodules are smaller than those observed on fibers assembled on

polysulfonate surfaces and are comparable to the 30-40 nm overlap observed in cell generated FN fibers using STORM microscopy. Additionally, while the height of the nodules in FN nanofibers strained to 100% was ~10-15 nm (Fig. 3.3.e), the height for the nodules in stretched FN nanofibers was approximately 3-4 nm. While it is unclear what the main contributing factors to the appearance of these small, periodic nodules, prior work has suggested it is due to the overlap between adjacent FN dimers in an extended state[122]. At this strain state, even within the same field of view of the fiber in Fig. 3.6a, we also observed larger, nodules (51.38 nm in this case) transition into relatively smooth fibrillar segments. This segment had a height that on the order of <2 nm. At the highest strained state we also observed a highly irregular nodular morphology, where large nodules progressively decreased in size, forming small nodules with an average diameter of ~24 nm and were spaced ~34nm, ~48 nm, and ~78 nm.

Altogether, we demonstrate that the nanostructure is dependent on the microscale strain on the FN fibers. We found that during strain, large nodules in fully contracted FN fibers begin to decrease in size; presumably as individual FN dimers get separated from large cluster. With further strain, the nodules continue to decrease in size and align in the direction of the applied load. At strains of 269% or greater we propose that the nodules are no longer made up of single or several FN dimers in a compact form but rather we speculate that the nodules represent the overlap of adjacent, elongated FN dimers. Finally, we also found that the morphological changes within the nanostructure do not homogenously change; rather there are regions of large nodules and regions where these nodules transition to short, periodic sequences of small nodules. Our results provide insight into how morphology of the nanostructure changes as a function of strain. Future work will continue this investigation with a focus on the thin fibril strands observed in high strains. We will measure how the nodule-nodule distance changes with increasing strain as well as study how these different conformational morphologies within the nanostructure of FN fibers, influence the biological properties of FN, specifically the exposure of cryptic binding sites.

CHAPTER 4:

Development of a Patterning-on-Topography Method to Measure the Effect of Fibronectin Strain on C2C12 Myoblast Adhesion

4.1. Abstract

The extracellular matrix (ECM) plays an integral role in tissue development and homeostasis. While the physical and chemical properties of the ECM are known to influence cell behavior and modulate gene expression, emerging evidence suggests that ECM proteins also have mechanosensitive properties. Specifically, the ECM protein fibronectin (FN) undergoes strain-dependent conformational changes that modulate self-assembly as well as binding to specific transmembrane integrin receptors. While recent studies have demonstrated that FN fibers on the order of several micrometers exhibit strain-dependent properties, these FN fibers are too small to be suitable cell culture substrates. Therefore many studies are limited to studying how FN strain affects the binding affinitiy of small molecules and peptides. To study these mechanosensitive properties and their effect on cell adhesion, we developed a Patterning-on-Topography (PoT) approach where 20 μm wide FN fibers or 1 cm x 1 cm FN sheets can be assembled and transferred to geometrically well-defined PDMS micro-ridges through the swelling and dissolution of a poly(N-isopropylacrylamide) (PIPAAm) sacrificial layer. The unique aspect of this approach is that the strain state of the FN fibers can be modulated by adjusting the height and spacing of the micro-ridges. For instance, when PoT printed onto PDMS micro-ridges that were 50 μm wide, 50 μm spaced, and 40 μm deep, 20 μm wide FN fibers and FN sheets maintained their initial unstrained conformation on the ridge tops but were strained to approximately 160% in the trenches between the micro-ridges. Increasing or decreasing the micro-ridge height results in higher or lower imposed FN strain, respectively. To determine how FN strain affects cell adhesion and integrin expression, we seeded C2C12 myoblasts onto FN sheets that were PoT printed onto low and high aspect ratio micro-ridges. We found that while a decrease in FN density in the trench bottoms likely promoted less cell spreading and α_5 integrin expression, the observed behaviors were exacerbated by FN in a highly strained state. This work provides insight into how the PoT technique could be used to investigate the mechanosensitive properties of FN and other ECM proteins and how these properties can affect cellular behavior.

4.2. Introduction

The chemical and physical properties of the extracellular matrix (ECM) play a major role in many critical biological processes such as embryonic development, wound healing, homeostasis, and disease[5-8,13,45,47,50,162,163]. While it has long be acknowledged that cells sense and respond to the chemical composition of their microenvironment, significant research over the past few decades has demonstrated that physical properties such as rigidity[16,24,25], topography[17,18], and geometry[19,23] also play an imporant role in cell behavior. This has sparked interest into the development of materials and fabrication strategies that can be used to influence cell behaviors such as adhesion[20-22], migration[23-25], and differentiation[15,26,27] *in vitro*.

Fibronectin (FN) is an ECM glycoprotein that is commonly used to promote cell adhesion and survival[40,86,164,165] in a variety of biomaterial systems. While FN, particularly the arginine-glycine-aspartic acid (RGD) tripeptide found in the FN III_{10} domain, is used ubiquitously throughout the fields of tissue engineering and regenerative medicine[166-168], a complete understanding of the biological function of FN is lacking. For example, while the RGD tripeptide is commonly grafted to a variety of surfaces to promote cell adhesion, inclusion of the synergy site on the neighboring FN III_9 domain is necessary for $\alpha_5\beta_1$ integrin adhesion to FN[84,101]. The inclusion of this domain into FN fragments containing the RGD site has been shown to increase proliferation, adhesion strength, and cell phenotype[88,169]. In addition to binding sites for cell surface integrin receptors and other ECM proteins such as collagen, heparin, and fibrin, FN also contains cryptic binding sites that require conformational changes within the FN molecules to become exposed[12,59]. It has been proposed that at least a portion of these sites become exposed in a force-induced manner where cell-generated forces lead to conformational unfolding of FN molecules which subsequently expose initially cryptic domains[59,109,119,136]. A major role of these cryptic domains is to regulate FN assembly into fibers[35,83,85]. Thus, understanding how FN fibers are manipulated and deformed by cells to modulate their bioactivity will enable the development of new strategies to modulate cell behavior in engineered systems.

With the development of several strategies to assemble FN fibers in a cell-free environment, there have been numerous studies investigating how the application of force can regulate the exposure of cryptic binding domains as well as the deactivation of initially surface exposed domain[41,42,81,119,120]. For example, Vogel and coworkers have established that FN fibers pulled out of a concentrated droplet can be deposited on stretchable substrates to enable their mechanical characterization[120]. Using this force-based assembly technique it was shown that strain modulates the exposure of cryptic cysteine amino acid residues[119], sites for bacterial adhesion peptides[42], and interactions with collagen type I[41]. However, these fibers are generally only a few micrometers in diameter thereby limiting their studies to small molecules and proteins. This is further supported by recent work in our laboratory which has shown that C2C12 cells differentiate preferably on larger 100 μm and 50 μm wide FN lines compared to smaller 10 μm and 20 μm wide FN lines[170].

Material-driven FN assembly techniques rely on the use of protein-surface interactions to initiate the formation of nanoscale FN fibrils on materials with a variety of surface chemistries[121,130]. Additionally, by altering the surface chemistry, it was possible to modulate the FN conformation thereby affecting integrin-FN interactions, cell adhesion, and cell differentiation[38,39,121,131]. Additionally, these studies have also demonstrated that FN conformation is able to modulate integrin binding. For example, several studies have demonstrated that the RGD sequence on the FN III_{10} domain must be functionally coupled with the PHSRN synergy site on the neighboring FN III_9 domain to enable $\alpha_5\beta_1$ integrin binding[38,39,169,171]. Decoupling of the RGD-synergy sites through either protein-surface interactions or engineered FN fragments resulted in a loss of $\alpha_5\beta_1$ integrin binding leading to downregulated osteoblast differentiation[39] and epithelial-to-mesenchymal transition in alveolar epithelial cells[169,171]. While these studies have demonstrated that protein-surface interactions can modulate FN conformation to alter its bioactivity and affect subsequent cell responses these fibrils are permanently bound to the surface they are adsorbed on preventing a dynamic structural and mechanical analysis.

In this study our first objective was to develop a method to allow us to impose strain onto FN fibers but also to immobilize them in the strained state in a manner the permits them to be suitable for C2C12 myoblast culture. We accomplished this through the development of a Patterning-on-Topography (PoT) method which allowed us to pattern FN fibers and sheets with a nanoscale thickness onto geometrically well-defined poly(dimethylsiloxane) (PDMS) micro-ridges. Using fiduciary marks, we found that the FN fibers became strained in a predictable manner as they were transferred to the vertical sidewalls and trenches between micro-ridges. Because the FN fibers and sheets maintained their initial geometry, we reasoned that they would make an ideal substrate to test the relationship between FN strain and C2C12 myoblast adhesion. We hypothesized that FN nanofiber strain would induce RGD-synergy site separation leading to the loss of $\alpha_5\beta_1$ integrin expression and cell spreading area. Using this approach we found that while decreases in FN density contributed to a decrease in both cell spreading area and α_5 integrin expression, the decreases were further exacerbated by FN under strain and thus, FN strain likely plays an important contributory role as well.

4.3. Materials and Methods

4.3.1 Fabrication of Microtopographically Modified Surfaces

Polydimethylsiloxane (PDMS, Sylgard 184, Dow-Corning) was mixed in 10:1 base resin to curing agent ratio, degassed and then used to create the different microtopographically modified surfaces in this study. Smooth control surfaces were fabricated by spin coating the PDMS on 25 mm diameter glass coverslips at 4,000 RPM and cured at 65°C for 4 h to create ~15 µm thick films[172]. Surfaces with random microtopographies were fabricated be creating PDMS replicas (negatives) of A4 printer paper and 220-grit and 150-grit sandpaper. To do this a 4x4 cm square of the paper was placed in the bottom of a 10 cm petri dish and PDMS was poured on top to an approximate thickness of 0.5 cm. The PDMS was cured at 65°C for 4 h, peeled off and then cut into 1x1 cm squares. Surfaces with micro-ridge topographies were fabricated by using photolithography according to previously published methods[123,124,172]. The materials used for photolithography varied depending on the photoresist layer thickness. For photoresist layers with a thickness between 2 and 10 µm, SPR 220.3 photoresist (Microchem) was spincoated onto glass wafers. Thicker photoresist layers between 10 and 40 µm were prepared by spin coating SU-8 2015 photoresist (Microchem) onto silicon wafers. SU-8 2050 photoresist (Microchem) was spincoated onto silicon wafers to generate photoresist layers thicker than 40 µm. All photoresist layers were exposed to UV light through a transparency photomask and then developed using SU8 developer or MF-26A developer (SU8 and SPR respectively, Microchem) to create SU-8 or SPR micro-ridges on top of silicon or glass wafers. Patterned wafers were then coated with PDMS to a thickness of 0.5 cm, cured at 65°C for 4 h, peeled off and then cut into 1x1 cm squares.

4.3.2. Uniform Coating and Microcontact Printing of ECM Proteins

For uniform protein coatings adsorbed from solution, the PDMS substrates were sonicated in 50% ethanol for 30 min and dried using nitrogen. The ECM protein FN derived from human plasma (Corning, catalog number 356008) was diluted to a concentration of 50 µg/mL in DI water and 40% of the FN was

conjugated to Alexa Fluor 488 or Alexa Fluor 488 fluorescent dyes (Life Technologies). A 300 µL droplet of FN solution was incubated on the PDMS substrates for 15 minutes, rinsed 2 times with DI water and then dried under nitrogen. For µCP, PDMS stamps with either micro-ridges 20 µm wide, 20 µm spaced and 2 µm tall or 50 µm wide, 50 µm spaced, and 2 µm tall were fabricated using photolithography as described above for the microtopographically modified surfaces. PDMS stamps were sonicated in 50% ethanol for 30 min, dried using nitrogen, incubated with FN solution for 1 h, rinsed 2x with distilled water and then dried under nitrogen. For experiments involving decreased FN density, we coated the PDMS stamps with FN diluted to concentrations of 50 µg/mL, 10 µg/mL, and 5 µg/mL. The µCP of laminin (LAM, Invitrogen) and collagen type IV (COL IV, Sigma) were performed similarly except both were diluted to working concentrations of 100 µg/mL in DI water. The PDMS substrates to be patterned were UV/Ozone treated for 15 minutes and then brought into conformal contact with the PDMS stamps for 5 min. Gentle pressure by light tapping the back of the PDMS stamps with tweezers was used to ensure contact.

4.3.3. PoT Printing of ECM Proteins

The PoT printing process is a modification of surface-initiated assembly (SIA)[123] where the release of the ECM protein occurs directly onto a microtopographically structured surface. To do this, we first spincoated 25 mm diameter glass cover slips with a 10% poly (N-isopropylacrylamide) (PIPAAm, Polysciences, Inc.) in 1-butanol (w/v) solution at 6,000 RPM. To PoT print features with a depth-to-width aspect ratio higher than 0.5, we increased the thickness of the PIPAAm layer by spin coating glass coverslips with a 40% PIPAAm in 1-butanol (w/v) solution at 2,000 RPM. PIPAAm layer thickness was determined by first spin coating PIPAAm at different concentrations and then making a small incision through the PIPAAm layer with a razor blade. Next, we used atomic force microscopy (AFM, MFP3D, Asylum Research) in air using AC mode with AC160TS-R3 cantilevers (Olympus Corporation) to scan over the incision. The thickness of the PIPAAm layer was then quantified using the IGOR Pro software environment (WaveMetrics, Inc.). Prior to PoT printing, the PIPAAm coated cover

slips were sterilized using high-intensity UV light for 15 min. Fluorescently labeled FN, LAM and COLIV were then patterned onto the PIPAAm coated cover slips by µCP with various geometries including, (i) 20 µm wide, 20 µm spaced lines; (ii) 50 µm wide, 50 µm spaced lines; and (iii) 1 cm x 1cm FN sheets. Next, PDMS substrates with microtopography on the surface were sterilized using high-intensity UV light for 15 min and placed in conformal contact with the protein patterned, PIPAAm coverslips for 10 min. Making sure to keep the PDMS stamp and PIPAAm surface in contact, the samples were placed within the well of a 6-well plate, 40°C sterile DI water was poured onto the stamp and PIPAAm, and then the plate was placed in 37°C incubator for at least 3 hours to allow time for water to enter the channels or spaces and diffuse into the PIPAAm. The plate was then removed from the incubator and placed in the biosafety cabinet at room temperature for 1 hour in order to dissolve the PIPAAm layer and release the ECM patterns onto the PDMS substrates. Once the PIPAAm dissolved, the PDMS and coverslip were no longer attached and the PDMS substrate could then be removed and used for cell culture or analysis. For experiments involving the PoT printing of FN lines onto flat PDMS coated coverslips, PDMS prepolymer solution was prepared as described above and then spincoated at 4000 rpm to achieve a layer thickness of ~13 µm. The PDMS coated coverslips were then placed in an oven set to 65° C and cured for 4 hours. Once cured, the coverslips were sterilized using high-intensity UV light for 15 min and then brought into conformal contact with FN patterned, PIPAAm-coated coverslips. The PIPAAm was dissolved and the FN patterns were released as described above. For all experiments, PoT printed substrates that had defects due to poor contact with the PIPAAm-coated cover slip or to improper water penetration within the topography were discarded. At least three samples per condition were used for imaging and cell seeding.

4.3.4. Stability of PoT-Printed ECM Patterns in Cell Culture

PDMS coated cover slips were either µCP or PoT printed with 20 µm wide and 20 µm spaced FN lines that were fluorescently labeled as previously described. All substrates were treated with 1% Pluronics F-127 (Sigma-Aldrich) for 15 min, washed three times with PBS, and then placed in separate

wells of a 6-well plate. For each condition, three cover slips were seeded with 50,000 C2C12 mouse myoblasts (ATCC, CRL-1772) per well in growth medium (DMEM, 10% fetal bovine serum, 1% Penicillin/streptomycin, 1% L-glutamine) while three cover slips were kept in growth medium without cells. After three days in culture, all samples were fixed and cell samples were stained for nuclei and F-actin and imaged as described earlier. C2C12 cells were authenticated and certified mycoplasma-free by the manufacturer.

4.3.5. Fabrication of Low Young's Modulus PDMS Stamps for Microcontact Printing

To determine the depth-to-width aspect ratio at which microcontact printing is unable to pattern topographical surfaces, we fabricated elastic, low Young's modulus PDMS stamps as described previously[172]. Briefly, stamps with an elastic modulus of ~50 kPa were prepared by mixing Sylgard 184 and Sylgard 527 in a 10:1 ratio (w:w). Sylgard 184 was prepared as described previously while Sylgard 527 was prepared by mixing equal parts of A and B components per manufacturer's instructions. The 10:1 mixture of Sylgard 184 and Sylgard 527 was then cast over a SPR 220.3 master mold and cured at 65 ^{o}C for 4 hours. Prior to casting, the SPR 220.3 master mold was silanized (PlusOne Repel-Silane ES, GE Healthcare) in a vacuum desiccator for at least 4 hours. After curing, the stamps were peeled off of the master mold, coated with FN as previously described and then µCP orthogonally onto PDMS micro-ridges.

4.3.6. Engineering FN Nanofibers with Fibronectin-Based Fiduciary Marks

FN nanofibers were tagged with fluorescently labeled, FN-based fiduciary marks by modification of the PoT technique. Briefly, 10 µm wide and 1 cm long lines of FN conjugated to an Alexa Fluor 488 dye (Life Technologies) were microcontact printed onto a PIPAAm coated coverslip. The PIPAAm coated coverslips were prepared as described above. Following microcontact printing, a PDMS stamp with 50 µm wide, 1 cm long, and 2 µm tall ridges was coated with a 50 µg/mL solution of FN in which 40% of the FN was conjugated to an Alexa Fluor 546 dye (Life Technologies). The stamp was then washed to remove excess FN, dried under a stream of nitrogen and subsequently brought into conformal contact

orthogonal to the 10 μm wide lines on the PIPAAm coated coverslip. While maintaining conformal contact, the PIPAAm was hydrated with warm, 40° C, distilled water and placed in a 37° C oven for 3 hours to allow for the water to enter the channels and diffuse into the PIPAAm. After 3 hours, the samples were taken to a biosafety cabinet and allowed to cool below the LCST of PIPAAm thereby releasing the fluorescently labeled, 10 μm wide FN lines off of the PIPAAm onto the PDMS stamp which was pre coated with FN. The stamp was then removed, washed in distilled water, dried under a stream of nitrogen and then brought into conformal contact with a new PIPAAm coated coverslip for 10 minutes to create arrays of 1 cm x 50 μm FN lines with 10 μm wide and 10 μm spaced fiduciary marks.

4.3.7. C2C12 Myoblast Cell Culture

Prior to cell seeding, all substrates were treated with 1% Pluronics F-127 (Sigma-Aldrich) for 15 minutes, washed three times with PBS, and then placed in separate wells of a 6-well plate. For each condition, a minimum of three coverslips or substrates were seeded with 20,000 C2C12 mouse myoblasts (ATCC, CRL-1772) in serum-free medium (DMEM, 1% penicillin/streptomycin) and cultured for 2 hours. After culture, all samples were rinsed with warm PBS to remove dead and/or floating cells and fixed and stained for nuclei, actin, and α_5 integrins. C2C12 cells were authenticated and certified mycoplasma-free by the manufacturer.

4.3.8. Fluorescent Staining and Imaging

The C2C12 cells and ECM proteins were fluorescently labeled in order to analyze the surface structure and cell response. The FN (Corning) was fluorescently labeled prior to use with fluorescent dyes, either Alexa Fluor 546 maleimide or Alexa Fluor 488 carboxylic acid, succinimidyl ester (Life Technologies) according to published methods[119]. The fluorescently labeled FN was combined with unlabeled FN at volume concentration of 40%. PDMS surfaces PoT printed with LAM or COL IV were fluorescently stained using monoclonal primary antibodies (Sigma, catalog number L9393 for LAM, C1926 for COL IV) followed by staining using Alexa Fluor 488 conjugated goat anti-mouse secondary antibodies. The

C2C12 cells were cultured for 2 hours, removed from the incubator, briefly washed with 37°C PBS and then fixed for 15 minutes in 4% paraformaldehyde with 0.05% TritonX-100. Next, samples were blocked for 1 hour with 5% bovine serum albumin and then incubated with 1:200 DAPI, 1:100 primary monoclonal antibody against α_5 integrin (Abcam, catalog number 150361) and 1:60 Phalloidin conjugated to Alexa Fluor 633 (Life Technologies) for 2 hours at 37°C. Samples were subsequently washed 3 times for 10 min in PBS and then incubated with goat anti-mouse secondary antibody conjugated to Alexa Fluor 488 (Life Technologies, catalog number A-11001) for 2 hours at 37° C. Finally, samples were washed 3 times for 10 min in PBS and mounted against No. 1.5 glass coverslips with Prolong Gold (Life Technologies). Substrates were imaged using a Zeiss LSM 700 laser scanning confocal microscope with a 20x (NA=0.8) air objective or a 63x (NA=1.4) oil immersion objective. 3-D image stacks were deconvolved using AutoQuant X3 (Media Cybernetics, Inc.). Image processing and 3D rendering were ImageJ image processing software (NIH) and Imaris (Bitplane, Inc.).

4.3.9. Quantifying Cell Area and α_5 Integrin Area

To analyze C2C12 cell spreading area, images were exported into imageJ, thresholded and coverted into binary images. The area of each cell was measured using the ROI manager. Prior to analysis, the images were inspected and cells that were in contact with the sidewalls through multiple planes in the *z* direction were excluded from analysis. Additionally, for α_5 integrin analysis, high resolution, 63x images were exported into imageJ and the cell area was first measured as described previously. Then, using only the α_5 integrin fluorescent channel at the *z* position correlating to the contact between FN and the cells, we thresholded the image to limit the amount of non-activated α_5 integrin. Area of the integrin plaques was measured as described previously.

4.3.10. Measurement of FN Density Using Atomic Force Microscopy

Atomic force microscopy (AFM) (MFP3D-Bio, Asylum Research) was used to analyze the nanostructure and quantify the density of constituent FN molecules following microcontact printing using low (5 μg/mL), intermediate (10 μg/mL), and high (50 μg/mL) concentrations of FN in solution when coating the

PDMS stamps. The microcontact printed FN was scanned in air using AC mode with AC160TS cantilevers (Olympus Corporation). For each condition, we scanned at high resolution with a points and lines of 1024x1024 over a scan area of 3 μm x 3 μm. To quantify FN surface coverage, we applied a mask to the fibrils within the nanostructure and measured the area occupied by the masked regions divided by the total area for the image.

4.3.10. Statistical Analysis

All results were analyzed using Sigma Plot (Systat Software, Inc). Unless otherwise noted, we performed a one-way ANOVA on Ranks with a Dunn's pairwise comparision. Results were considered significant for $P<0.05$.

4.4. Results

4.4.1. Patterning a Wide Variety of Topographies with Fibronectin and Other ECM Proteins

In this study, we first sought to develop a method that would enable the conformal patterning of ECM proteins onto complex and/or high aspect ratio topographies in a manner similar to how microcontact printing is used to pattern 2D surfaces. To do this, we modified a SIA[123,124] approach to create a Patterning-on-Topography (PoT) technique (Fig. 4.1). Briefly, as in SIA, a PDMS stamp with raised features is first coated with a FN solution and then microcontact printed onto a PIPAAm coated coverslip (Fig. 4.1a). Instead of just releasing the FN fibers by hydrating the PIPAAm and cooling the solution below its lower critical solution temperature (LCST, ~32° C) as performed in SIA, we first bring another topographical surface into conformal contact with the FN-patterned, PIPAAm-coated coverslip (Fig. 4.1b). We then triggered the swelling and dissolution of PIPAAm by adding warm, 40° C, distilled water and allowed it to cool below the LCST of PIPAAm. As the solution temperature cooled, the PIPAAm layer first swelled (Fig. 4.1c) before completely dissolving. This swelling action is responsible for "pushing" the FN pattern into conformal contact with the entire surface area of the topography (Fig. 4.1d).

When using the parameters routinely used for SIA, we found that there was an aspect ratio limitation of the topography such that if the depth:width ratio of a topography was greater the 0.5, the FN lines would no longer be able to pattern to entire topographical feature (data not shown). Instead, we found that it was possible to increase the PIPAAm layer thickness by increasing the concentration of PIPAAm in solution (w/v) prior to spincoating (Fig. 4.2). Using AFM, we found that when using the standard 10% PIPAAm solution, the layer thickness was 0.73 ± 0.10 μm (Fig. 4.2a). The layer thickness subsequently increased with increasing PIPAAm concentration up to 5.67 ± 1.18 μm (Fig. 4.2b-d). Cross-section profiles further confirm that by tuning the concentration of PIPAAm in solution, we could modulate the spincoated layer thickness (Fig. 4.2e-h). Moreover, when fit to a linear regression, there was a good agreement between spincoated layer thickness and PIPAAm solution concentration (Fig 4.2i, r^2 =

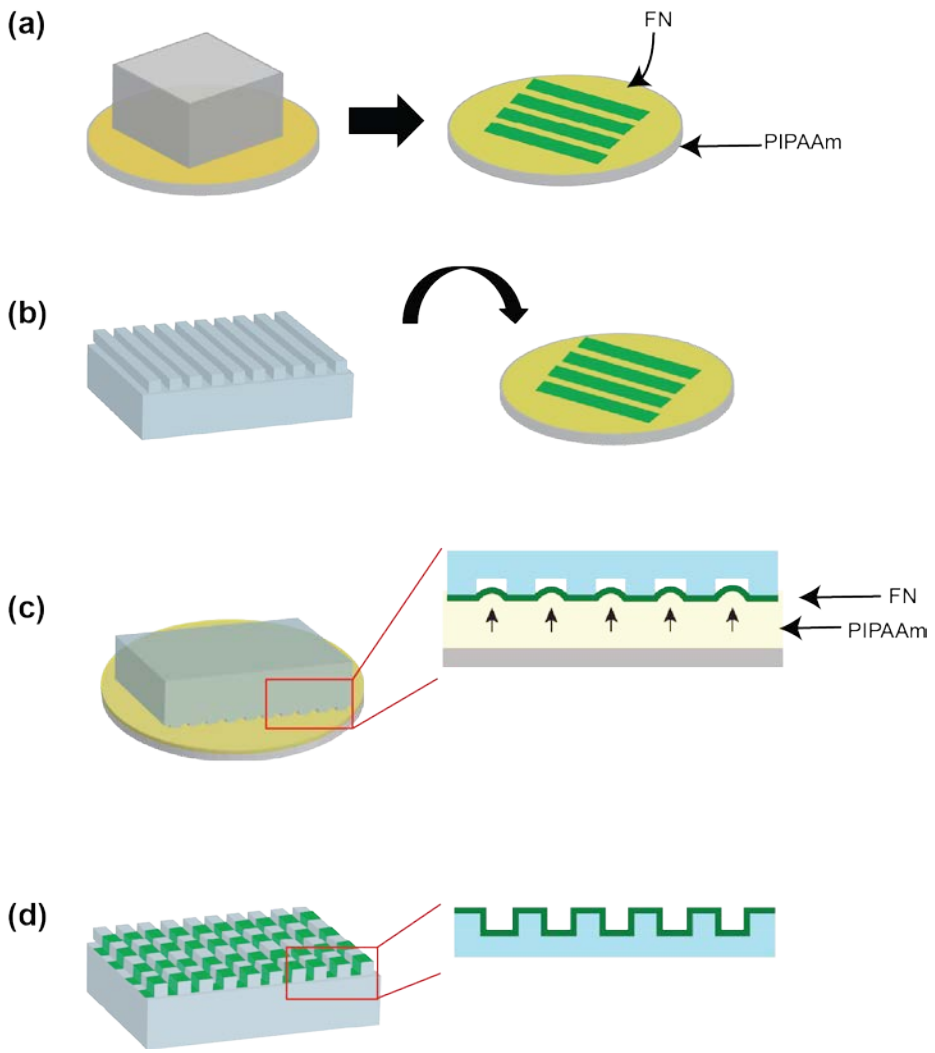

Fig. 4.1. Schematic of the PoT printing method. (a) FN or other ECM proteins are microcontact printed onto a PIPAAm coated coverslip. (b) A topographical substrate is brought into conformal contact with the FN-patterned, PIPAAm coated coverslip and (c) submerged in warm, 40° C distilled water. As the solution cools, the PIPAAm swells, pushing the FN against the topography. (d) Once the PIPAAm is completely dissolved, the topographical substrate contains a FN pattern that reflects to original microcontact printed geometry.

0.9934). Using a thicker, ~5.5 μm deep PIPAAm layer prepared by a 40% PIPAAm solution, we were able to overcome these aspect ratio limitations.

To demonstrate the capabilities of PoT, we first PoT printed 20 μm wide lines of FN onto PDMS replicas of 150 and 220-grit sandpaper (Fig. 4.3). Due to its highly irregular surface topography,

sandpaper represents an ideal test surface. To visualize microtopographies of the different sandpaper surfaces, we first coated the entire surface with a fluorescently tagged fibronectin solution (Fig. 4.3a). Using flat PDMS as a control surface, we then tested the ability to transfer 20 μm wide lines of FN using conventional microcontact printing (Fig. 4.3b). As expected, microcontact printing patterned the flat PDMS surface with high fidelity. However, when microcontact printed onto either 220-grit or 150-grit sandpaper there were noticeable gaps in the pattern that extended over 100 μm. Additionally, because the stamp was firmly pressed onto the substrate in an attempt to pattern the entire surface, the pattern collapsed resulting in a loss of the fidelity of the FN lines. Finally, we PoT printed FN lines onto the three different surfaces (Fig. 4.3c). When PoT printed onto the flat PDMS control surface, the FN lines were able to transfer with high fidelity, almost identical to the microcontact printed FN lines. Unlike microcontact, which was unable to pattern the complex sandpaper topographies, PoT was able to transfer the FN lines to both the 220-grit and 150-grit sandpaper. The lines were able to traverse into complex gaps in the surface while maintaining line fidelity.

Since sandpaper is a highly irregular surface, we sought to investigate the limitations of PoT in a more controlled manner. To do this, we fabricated PDMS micro-ridges with defined width, depth, and spacing thereby allowing us to control the micro-ridge aspect ratio (Fig. 4.4). We started with surfaces that were engineered to have 20 μm wide, 20 μm spaced, and 11.5 μm deep micro-ridges (Fig. 4.4a) and then systematically increased the depth to 27 μm (Fig. 4.4b), 37 μm (Fig. 4.4c), and 48 μm (Fig. 4.4d). This corresponded to depth:width aspect ratios of 0.57, 1.35, 1.85, and 2.4 for micro-ridges with depths of 11.5 μm, 27 μm, 37 μm, and 48 μm, respectively. Orthogonal cross-sections of the micro-ridges reveal that the FN lines conformally patterned the micro-ridge top, the vertical sidewalls, and the trench bottom between micro-ridges (Fig. 4.4e-h). The one exception involved the 48 μm deep micro-ridges were we observed small breaks in the line pattern, particularly on the sidewalls (Fig. 4.4h). A 3D rendering of the FN lines PoT printed onto the 48 μm deep, high aspect ratio micro-ridges confirms that the FN lines where broken along the sidewalls (Fig. 4.4i).

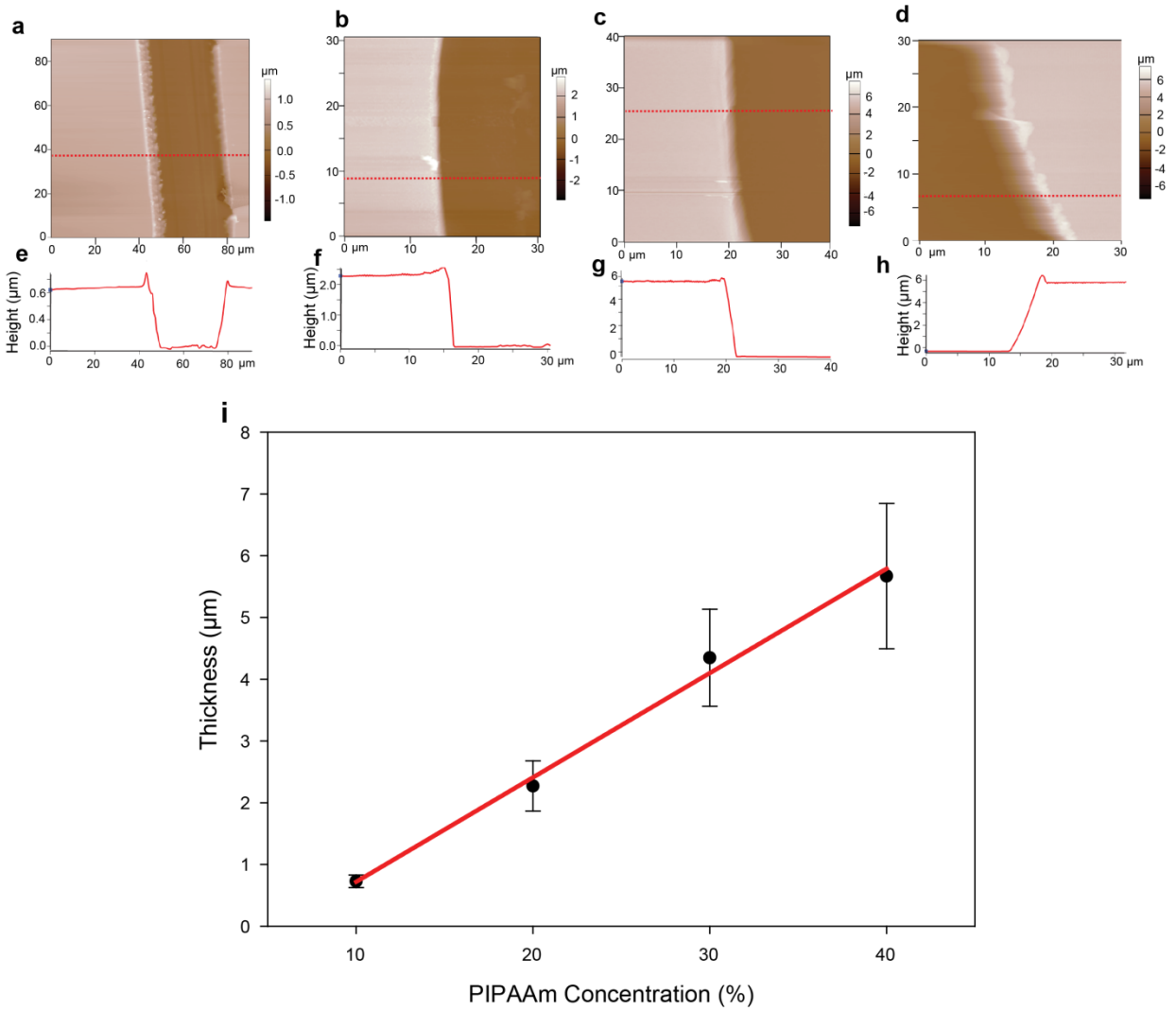

Fig. 4.2. **The thickness of the PIPAAm layer was tuned by changing the concentration (w/v) of PIPAAm being spincoated.** The concentration of PIPAAm dissolved in butanol (w/v) was varied from 10% to 40% in order to tune the thickness of the resulting PIPAAm layer being spincoated. Representative AFM images of the spincoated PIPAAm layer on glass coverslips from (a) 10%, (b) 20%, (c) 30%, and (d) 40% PIPAAM solutions. (e-h) Cross sectional profiles of the red line drawn in the respective AFM images (a-d) demonstrated control of the PIPAAm thickness. (i) Quantification of the PIPAAm layer thickness showed that the PIPAAm layer increased from 0.73 ± 0.10 µm to 5.67 ± 1.18 µm. The red line is linear regression with r^2 = 0.9934. Error bars are standard deviation of n=3 PIPAAm coated coverslips where the thickness of the layer was the mean of measurements taken at the center, right edge, and left edge.

Interestingly, the break appeared to be at the same location on the sidewall for consecutive micro-ridges. Furthermore, a top-down, maximum intensity projection indicates that the FN on the ridge tops appears to be at a higher density than the FN in the trench bottoms (Fig. 4.4j). Consequently, a depth:width aspect ratio of 2.4 appeared to be the maximum aspect ratio for PoT printing FN features. Further investigation is needed to confirm whether other ECM proteins have different aspect ratio limitations.

To further expand our understanding of the ability of PoT to print FN lines onto a variety of surfaces, we again modulated the micro-ridge geometry to first PoT print 20 μm wide lines of FN onto 2 μm wide, 2 μm spaced, and 2.5 μm deep micro-ridges (Fig. 4.5a). We then expanded to PoT printing lines of FN onto 30 μm wide, 50 μm wide, and 200 μm wide micro-ridges with depths of 30 μm, 32 μm, and 36 μm, respectively (Fig. 4.5b-d). Cross-sectional views further demonstrate the FN line were able to conformally pattern the ridge tops, sidewalls, and trench bottoms for a wide range of micro-ridge geometries (Fig. 4.5e-h). Interestingly, the 30 μm wide and 50 μm wide micro-ridges did not have completely vertical sidewalls yet; the FN lines were able to fully conform to the polygonal shape.

To fully validate that variations of microcontact printing were unable to pattern high aspect ratio topographies, we engineered low modulus (E ~ 50 kPa, down from ~1.72 MPa) PDMS stamps[173] under the assumption that they would be able to deform around the micro-ridges and pattern the entire topography (Fig. 4.6). Using this approach we microcontact printed 20 μm wide FN lines onto PDMS micro-ridges that were 20 μm wide, 20 μm spaced and 7 μm deep (Fig. 4.6a). At this depth, the stamp was able to deform enough to pattern bottom of the trenches (Fig. 4.6b) however, a cross-sectional view indicates that the stamps were unable to transfer FN lines onto the vertical sidewalls of the micro-ridges (Fig. 4.6c). Since the depth:width aspect ratio of these micro-ridges was 0.35, considerably low compared to the aspect ratio of topographical features that can be patterned using PoT, we also tested the ability to microcontact print FN lines onto deeper micro-ridges that were 14 μm deep (Fig. 4.6d).

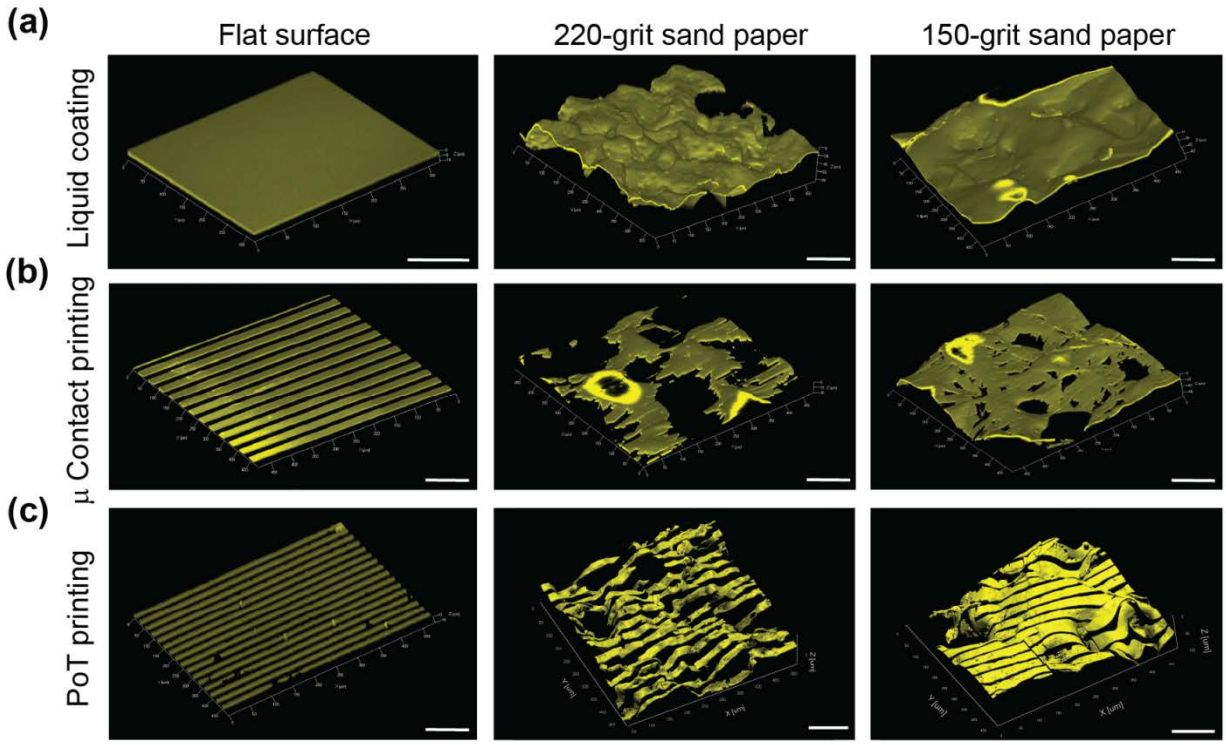

Fig. 4.3. PoT printing micropatterns of FN lines onto topography complex surfaces (a). Representative 3D confocal images of flat PDMS, 220-grit, and 150-grit sandpaper PDMS replicas that were uniformly coated with a fluorescent FN solution. (b) 20 μm wide lines of FN were microcontact printed onto each of the substrates where there were noticeable gaps in the pattern on the sandpaper replicas. (c) 20 μm wide FN lines were PoT printed onto each of the surfaces maintained their integrity as they adhered to all of the topographical features. Scale bars are 100 μm.

In this case, the low modulus PDMS stamp was unable to deform enough to reach the bottom of the trenches (Fig. 4.6e). Additionally, a cross-sectional view confirms that, while not able to pattern the bottom of the trenches, the stamps were again unable to pattern the vertical sidewalls (Fig. 4.6f). It is also important to note that the pressure applied to the low modulus PDMS stamps resulted in a loss of pattern fidelity on the micro-ridge tops (Fig. 4.6a).

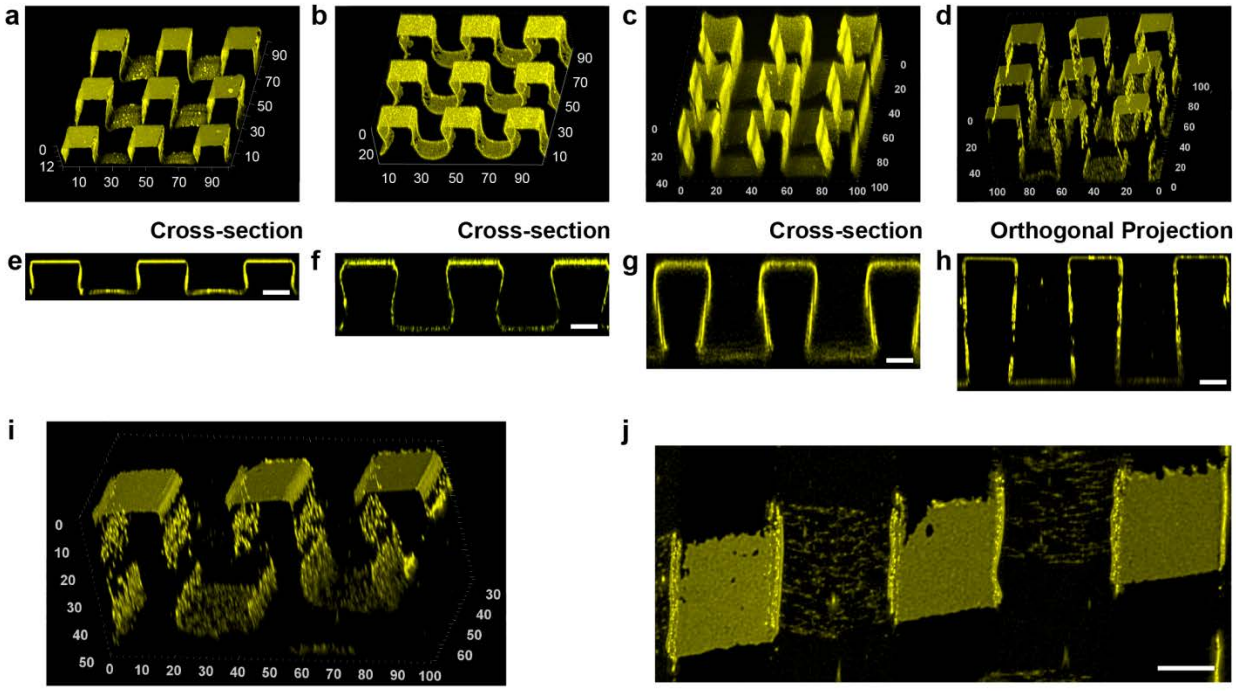

Fig. 4.4. PoT printing onto variable aspect ratio micro-ridges. We engineered surfaces with 20 µm wide, 20 µm spaced micro-ridges at heights up to 48 µm and used confocal microscopy to analyze conformal patterning. PoT printed FN lines released onto the (**a**) 11.5 µm (**b**) 27 µm and (**c**) 37 µm high micro-ridges were found to achieve conformal patterning. This is a depth-to-width aspect ratio of 1.85 at the 37 µm ridge height and the FN pattern was continuous and conformal to the ridge tops, vertical sidewalls and trench bottoms. At higher ridge heights and aspect ratios >2.0 PoT was still able to pattern FN on the surfaces, however the FN started to become discontinuous in places, (**d**) as shown for the 48 µm high ridges at an aspect ratio of 2.4. Cross-section views of the (**e**) 11.5 µm (**f**) 27 µm and (**g**) 37 µm high micro-ridges confirmed the continuous and conformal FN patterning while the (**h**) 48 µm high micro-ridges showed distinct gaps in FN on the vertical sidewalls. Closer examination of PoT on the 48 µm high micro-ridges showed that (**i**) in 3D the gaps in FN transfer were observed only on the vertical sidewalls, and (**j**) in a top-down projection, the FN on the ridge tops appeared to be at higher density than the FN in the trench bottoms. The micro-ridges with aspect ratios >0.5 were PoT printed using the 40% (w/v) PIPAAm coating. Scale bars are 10 µm.. For each depth, the PDMS micro-ridges were prepared using the same master mold; therefore their depth remained constant for each experiment.

While FN was the main focus of this work, we also confirmed that the PoT method is compatible with other ECM proteins, namely laminin and collagen IV (Fig. 4.7). To test this, we first PoT printed 20 μm wide lines of laminin onto 20 μm wide, 20 μm spaced, and 5 μm deep PDMS micro-ridges. We found that, like FN, laminin was able to transfer to and conformally pattern the micro-ridge tops, vertical sidewalls, and trench bottoms (Fig. 4.7a). Next, we PoT printed 20 μm wide lines of collagen IV onto identical PDMS micro-ridges. As expected, collagen IV was also able to conformally pattern the micro-ridges (Fig. 4.7b). Lastly, we wanted to test the ability to PoT print a more complex, multicomponent FN/laminin mesh onto PDMS micro-ridges that were 20 μm wide, 20 μm spaced, and 14.5 μm deep (Fig. 4.7c-e). Following PoT, we found that the two proteins were able to conform to the PDMS micro-ridges while maintaining their spatial arrangement relative to each other. This further demonstrates the utility of the PoT method and how it can be applied to wide variety of substrate topographies using one or many ECM proteins.

Since PoT printing enables the transfer of FN patterns with high fidelity in a manner similar to microcontact printing on 2D surfaces, we wanted to confirm that PoT printed FN patterns behaved similarly to microcontacted printed ones in cell culture conditions (Fig. 4.8). To provide a direct comparison, we microcontact printed (Fig. 4.8a) and PoT printed (Fig. 4.8b) 20 μm wide lines of FN onto flat PDMS surfaces and kept them in cell culture conditions (growth media, 37° C, 10% CO_2) without cells for two days. After two days, there were no discernable differences between the FN lines prepared through each technique. Next, we wanted to determine whether cultured cells would respond similarly to FN lines prepared through either microcontact printing (Fig. 4.8c) or PoT printing (Fig. 4.8d). To do this, we seeded C2C12 myoblast cells and cultured them for 2 days.

Since PoT printing enables the transfer of FN patterns with high fidelity in a manner similar to microcontact printing on 2D surfaces, we wanted to confirm that PoT printed FN patterns behaved similarly to microcontacted printed ones in cell culture conditions (Fig. 4.8).

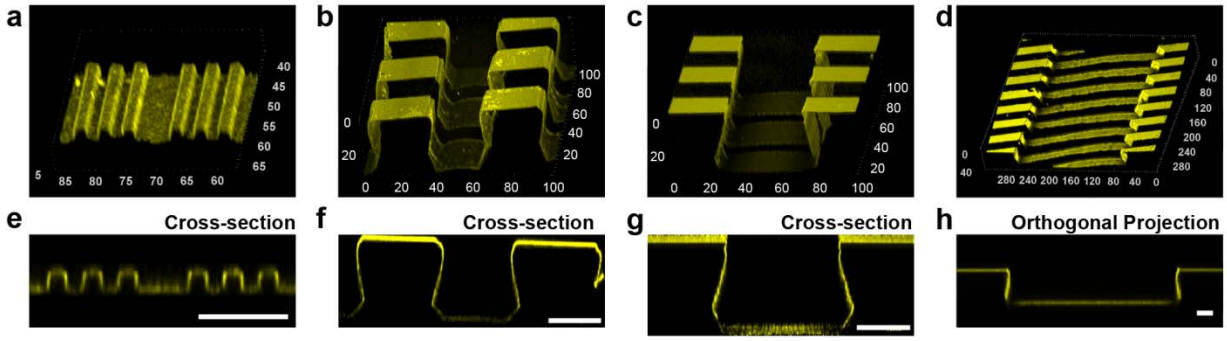

Fig. 4.5. PoT printing onto variable size micro-ridges. In addition to the 20 µm wide and 20 µm spaced PDMS micro-ridges, FN lines were also PoT printed across smaller and larger PDMS micro-ridges to demonstrate that the technique is applicable to a wide range of surface feature dimensions. Specifically, 20 µm wide FN lines were PoT printed across micro-ridges that were (**a**) 2 µm wide, 2 µm spaced, 2.5 µm deep with every fourth ridge missing, (**b**) 30 µm wide, 30 µm spaced, and 30 µm deep, (**c**) 50 µm wide, 50 µm spaced, and 32 µm deep, and (**d**) 200 µm wide, 200 µm spaced and 36 µm deep. Analysis of the cross-section of the (**e**) 2, (**f**) 30, (**g**) 50, and (**h**) 200 µm wide micro-ridges demonstrated that in all cases, the FN lines were able to fully conform to the topography. This confirms that PoT can pattern FN on micro-ridges spanning 2 orders-of-magnitude in X and Y dimensions and greater than 1 order-of-magnitude in the Z dimension. These results also suggest that smaller, nanometer scale features should be able to be patterned. Scale is in micrometers for (**a-d**). Scale bars are (**e**) 10 µm and (**f-h**) 20 µm. Images are representative for n=3 separate experiments.

To provide a direct comparison, we microcontact printed (Fig. 4.8a) and PoT printed (Fig. 4.8b) 20 µm wide lines of FN onto As expected, the C2C12 myoblasts were able to adhere to both the microcontact printed lines and the PoT printed FN lines without any discernable differences in cell morphology. Additionally, looking solely at the FN channel of the fluorescent images reveals that the cells were able to remodel both the microcontact printed FN lines (Fig. 4.8e) and PoT printed FN lines (Fig. 4.8f). Altogether, these results indicate that PoT printed FN lines behave similarly to microcontact printed FN lines in terms of stability in cell culture conditions and their ability to promote cell adhesion and FN remodeling.

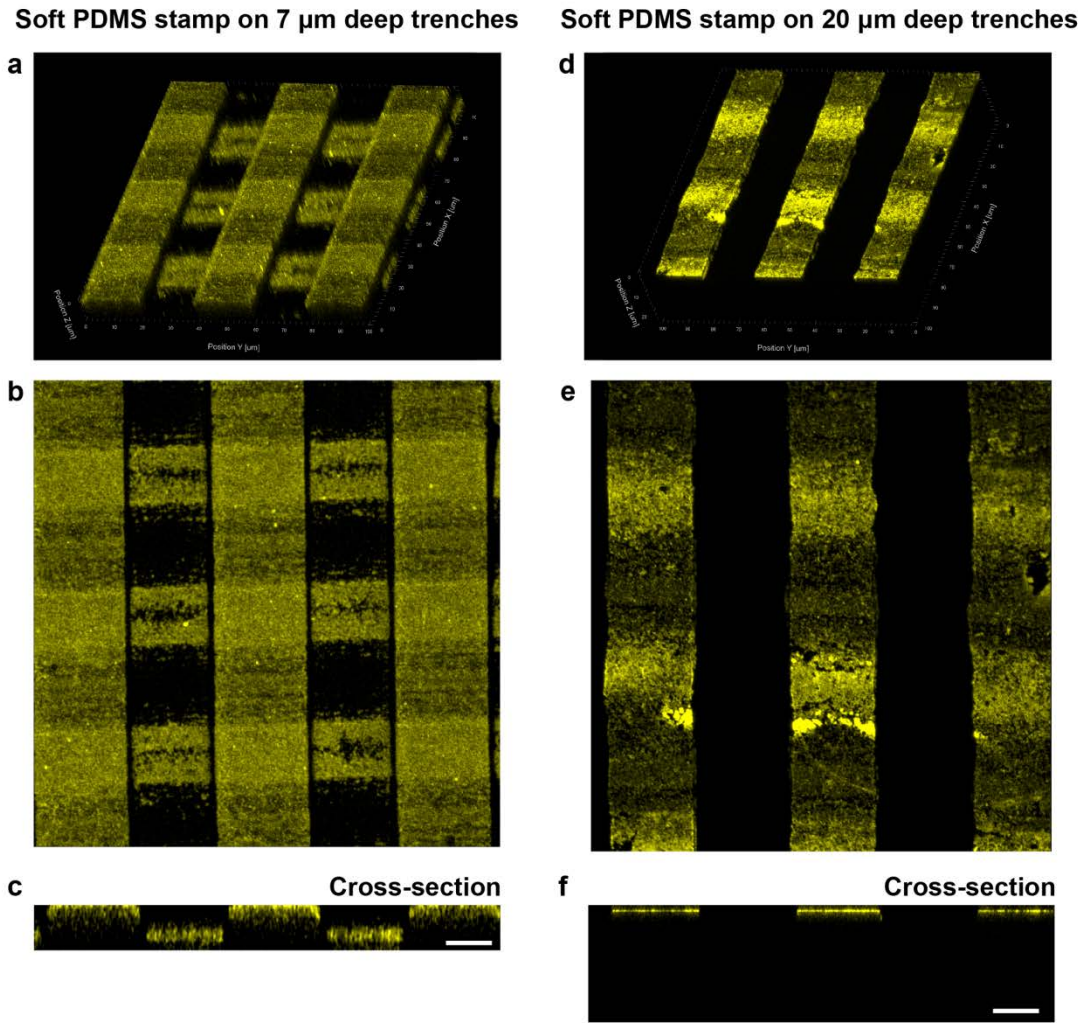

Fig. 4.6. Microcontact printing with low Young's modulus PDMS stamps is unable to conformally pattern FN onto micro-ridges. Representative confocal microscopy images of 20 µm wide FN lines microcontact printed orthogonally onto 20 µm wide, 20 µm spaced micro-ridges using a low Young's modulus PDMS stamp (E = 50 kPa)[172], (**a**) At a 7 µm ridge height the FN lines reach the bottom of the trenches (**b**), but do not pattern the vertical side walls, leaving a distinct gap in protein transfer between the ridges tops and trench bottoms (**c**). Further, the pressure required to press the soft PDMS stamp onto the micro-ridges in order to pattern the trench bottom causes loss of pattern fidelity on the ridge tops (**a**). Specifically, FN is also transferred in-between the 20 µm wide FN lines. (**d**) At a 14 µm ridge height, the FN lines do not reach the bottom of the trenches (**e**), and also do not pattern the vertical side walls (**f**). Further, as seen in (**a**), the pressure applied to the PDMS stamp in order to pattern the micro-ridges causes a loss of pattern fidelity with protein transfer in-between the FN lines. Scale bars are 10 µm. Images are representative for n=3 separate experiments.

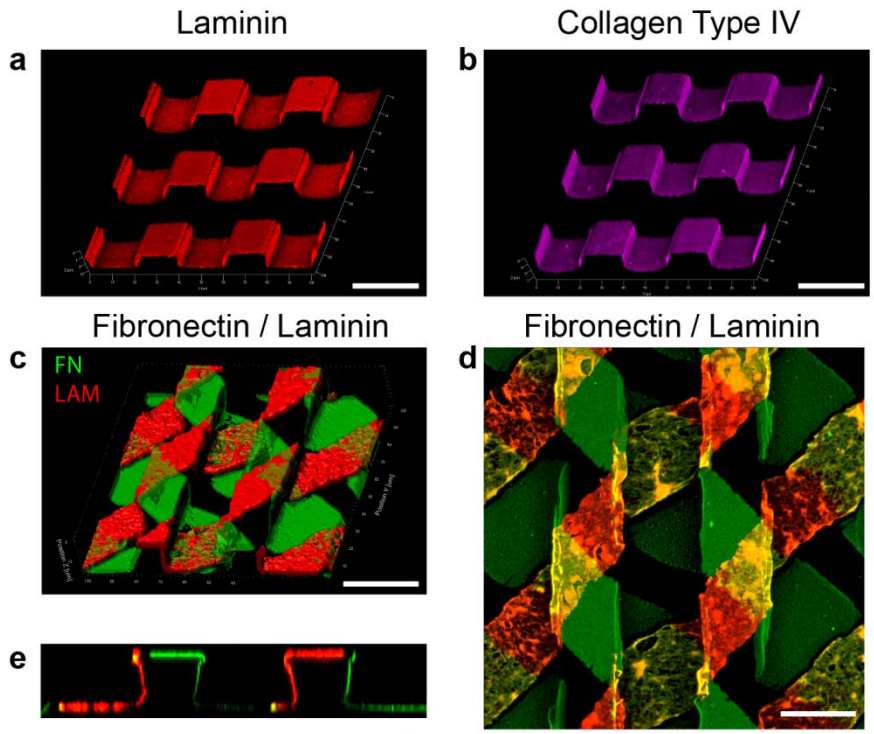

Fig. 4.7. PoT printing can be performed using a range of ECM proteins. Representative confocal images of 20 µm wide, 20 µm spaced, 5 µm tall micro-ridges in PDMS orthogonally PoT printed with 20 µm wide lines of (**a**) laminin (red) and (**b**) collagen type IV (violet). Note that the patterned ECM follows the contours of the micro-ridges, which run orthogonal to the direction of the ECM lines. (**c**) Confocal image of 20 µm wide, 20 µm spaced, 14.5 µm tall micro-ridges in PDMS PoT printed sequentially at a 45° angle with FN and laminin lines to create a bicomponent, orthogonal fibronectin/laminin mesh. The top view (**d**) shows the good pattern transfer fidelity over multiple PoT printings and the cross-section (**e**) demonstrates that both proteins are conformal to the vertical sidewalls. Scale bars are 20 µm. Images are representative for n=3 separate experiments.

4.4.2 Using PoT as a Method to Strain FN in a Controlled Manner

Since, there was a noticeable difference in the appearance of FN depending on whether it was on the micro-ridge top or the trench bottom, particularly on the high aspect ratio, 48 µm deep micro-ridges (Fig. 4.4j); we reasoned that FN was being strained as it was being pushing into the trenches by the swelling PIPAAm. For example, on 20 µm wide, 40 µm deep micro-ridges, the FN lines on the PIPAAm surface pre-release span across the 20 µm wide gap (Fig. 4.9a). When the PIPAAm is hydrated in warm distilled water and cools past its LCST, it begins to swell and push the FN lines onto the topographical surface (Fig. 4.9b). The FN initially in contact with the micro-ridge tops becomes immediately

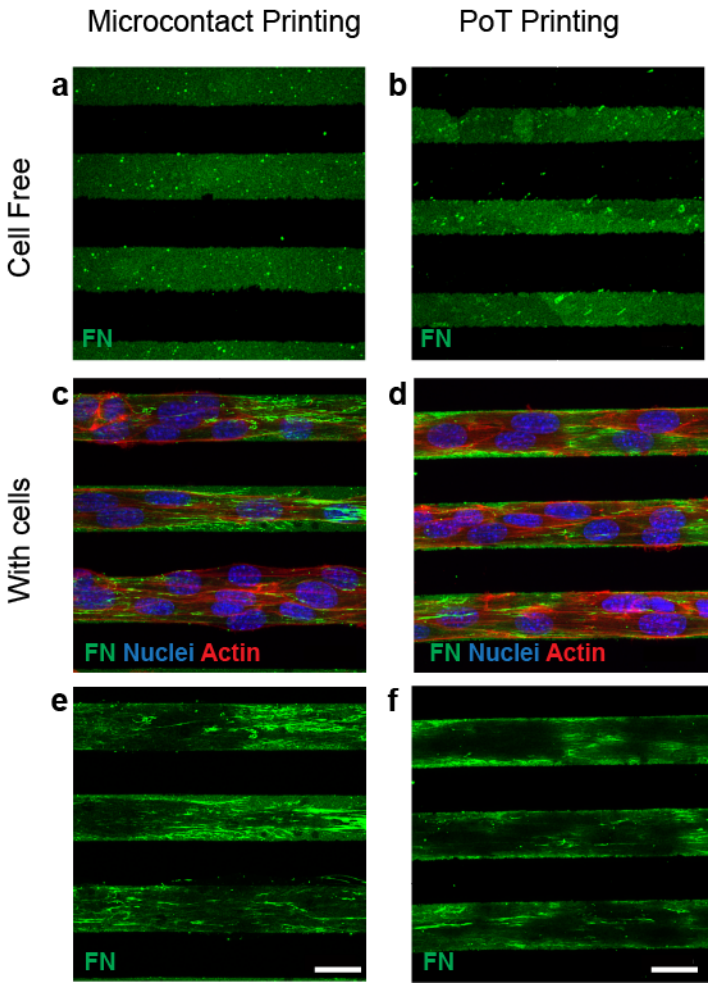

Fig. 4.8. PoT printed FN lines are stable under cell culture conditions, comparable to microcontact printed FN lines. Representative confocal images of 20 µm wide, 20 µm spaced FN lines that were (**a**) microcontact printed or (**b**) PoT printed onto PDMS coated glass coverslips. These were incubated in cell culture conditions (growth media, 37°C, 10% CO_2) without cells for two days and showed no discernable difference between the microcontact printed and PoT printed FN lines. C2C12 myoblasts seeded and cultured for 2 days on the (**c**) microcontact printed and (**d**) PoT printed FN lines showed similar cell morphology with alignment along the length of the FN lines. Imaging of the printed and cell-assembled FN on (**e**) microcontact printed and (**f**) PoT printed FN lines revealed comparable patterns of matrix assembly. Scale bars are 20 µm. Images are representative for n=3 separate µCP or PoT printed coverslips.

immobilized although the FN suspended between the micro-ridges continues to be pushed into the trench by the swelling PIPAAm (Fig. 4.9c). After the PIPAAm has completely swelled and dissolved, the FN lines are left conformally patterned to the sidewalls and trench bottom of the micro-ridges. Since the initially non-supported segment of the FN line is responsible for covering the both sidewalls and the

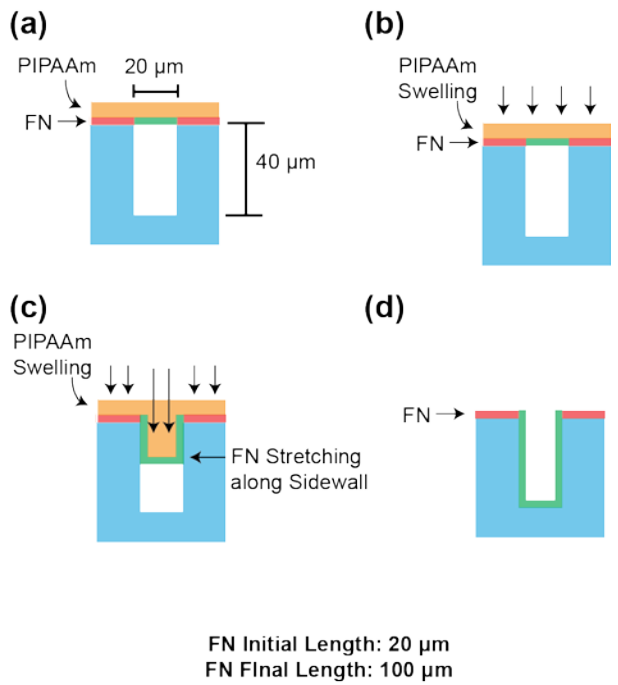

Fig. 4.9. Controlling FN strain by PoT printing FN onto PDMS micro-ridges. (a) The initial unsupported FN segment (green) that spans between two micro-ridges was initially 20 µm. (b) Once the PIPAAm becomes hydrated, it begins to swell and push on the FN pattern. (c) As swelling continues, the unsupported segment gets pushed down the sidewalls of the micro-ridges. (d) At maximal PIPAAm swelling, the unsupported segment is capable of reaching the trench bottom between the micro-ridges. In this case, the final length of the initially unsupported segment is 100 µm, a 400% strain.

trench bottom, we can estimate the length change and thus the strain imposed on that FN fiber segment (Fig. 4.9d).

To more accurately determine the strain imposed on the FN fibers as they are PoT printed onto PDMS micro-ridges, we tagged the 20 µm wide FN lines with FN-based fiduciary marks (Fig. 3.1) that we developed based on a combination of SIA and PoT methods. Unlike previous experiments which utilized 10 µm wide, 10 µm spaced fiduciary marks, we engineered the FN fibers to have 2 µm wide, 2 µm spaced fiduciary marks in order to increase their sensitivity to regional differences in strain. Using this approach, we PoT printed FN fibers onto PDMS micro-ridges with varying geometry to modulate the expected strain on the FN fibers in the bottom of the trenches (Fig. 4.10). First, when PoT printed onto low aspect ratio PDMS micro-ridges that were ~50 µm wide and ~10 µm deep, we found that the

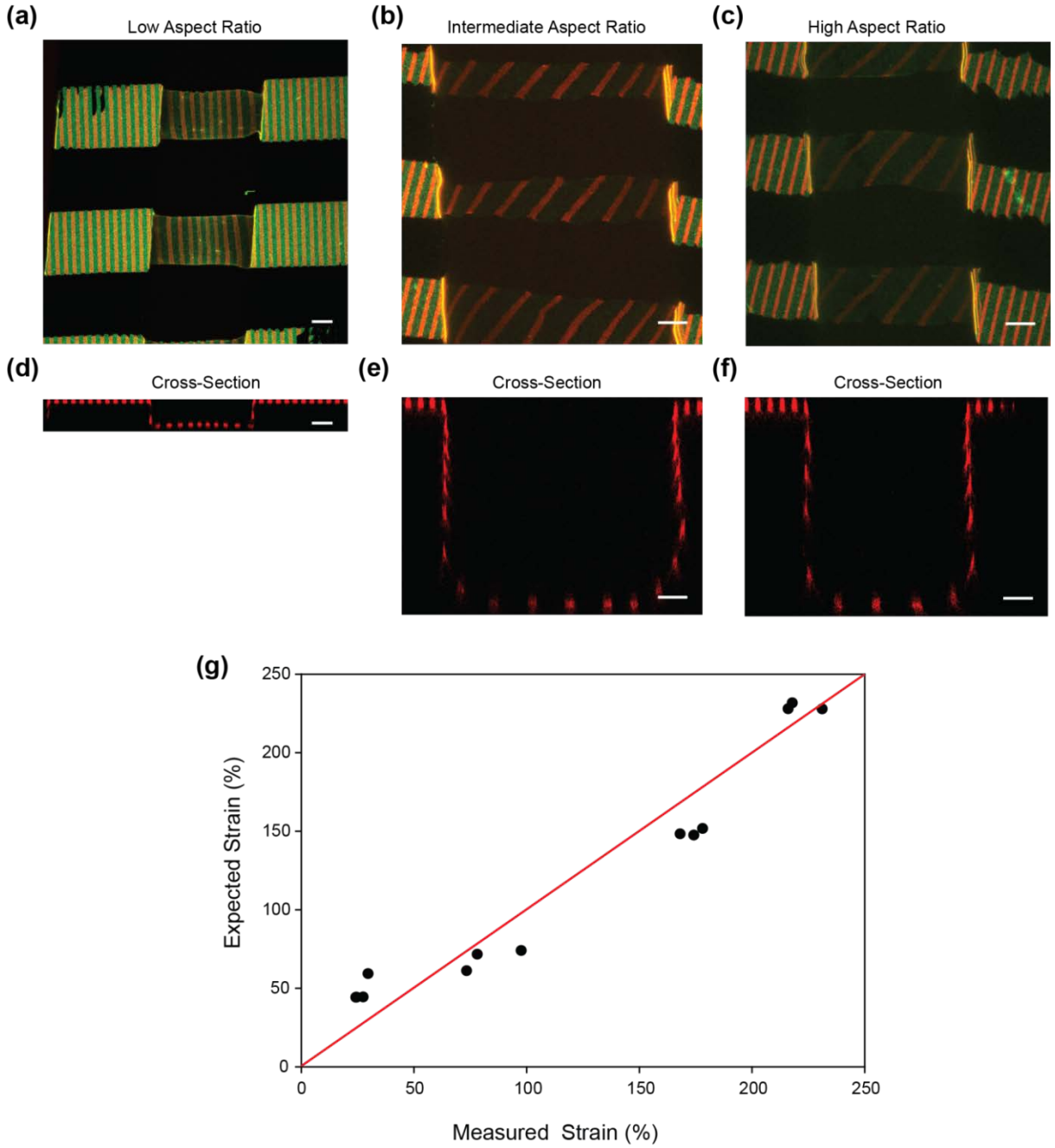

Fig. 4.10. Using fiduciary marks to measure FN fiber strain as it is PoT printed onto PDMS micro-ridges of different geometries. 20 µm wide FN fibers (green) were labeled with 2 µm wide, 2 µm spaced fiduciary mark (red) and PoT onto (a) Low aspect ratio micro-ridges that were 50 µm wide and 10 µm deep, (b) intermediate aspect ratio micro-ridges that were 80 µm wide and 70 µm deep, and (c) high aspect ratio micro-ridges that were 55 µm wide and 70 µm deep. Cross-sectional views of the fiduciary mark channel demonstrate the differential strain imposed on the FN fibers as they adhered to the sidewalls and trench bottoms for the (d) low, (e) intermediate, and (f) high aspect ratio micro-ridges. The expected strain, using the micro-ridge width as the initial length and the FN contour length following PoT as the strained lenghth was plotted against the strain measured by separation of the center-to-center distance of the fiduciary marks. The data were fit to the line, $y = x$ ($r^2 = 0.938$).Scale bars are 10 µm.

the average center-to-center distance of the fiduciary marks increased from 4.05 ± 0.02 μm on the ridge tops to 5.13 ± 0.09 μm in the bottom of the trenches (Fig. 4.10a). This correlated to an average strain of 25.43% while the expected strain (based on the micro-ridge geometry) was 48.02%. Next, we increased the aspect ratio by engineering micro-ridges that were ~80 μm wide and ~70 μm deep (Fig. 4.10b). When the fiduciary mark-labeled FN fibers were PoT printed onto these micro-ridges, we found that the center-to-center distance of the fiduciary marks increased from 4.06 ± 0.03 μm on the ridge tops to 11.09 ± 0.18 μm in the bottom of the trenches, a measured strain of 173.15%. Interestingly, based on the micro-ridge geometry, we expected the overall strain to be 149.14%. We reason that this may be attributed to inconsistencies associated with the integration of the fiduciary marks to the FN fibers (see discussion). Moreover, we investigated whether the fiduciary marks were able to track FN fiber strain on high aspect ratio micro-ridges. Therefore we engineered micro-ridges that were ~55 μm wide and 70 μm deep (Fig. 4.10c). After PoT printing the fiduciary mark-labeled FN lines onto the micro-ridges, we measured an increase in the center-to-center fiduciary mark distance from 4.07 ± 0.02 μm to 13.01 ± 0.35 μm representing a strain of 219.66% compared to an expected strain of 229.12%.

Generation of orthogonal views showing only the fiduciary mark channel of the FN fibers PoT printed onto low, intermediate, and high aspect ratio micro-ridges (Fig. 4.10d-f) points out that the strain is not uniform as the FN fibers adhere to the sidewalls and bottom of the trenches. Specifically, the strain typically is largest on the bottom of the sidewalls which may account for the measured strain being lower than the expected strain. To determine how closely we can estimate strain based purely on the micro-ridge geometry, we plotted the expected strain based on the micro-ridge geometry versus the strain measured by the center-to-center distance of the fiduciary marks in the bottom of the trenches (Fig. 4.10g). We found that there was a generally good agreement between the two and when fit to the line:

$$y = x,$$

there was generally good agreement between the expected and measured strain values ($r^2 = 0.938$).

Therefore we can reasonably assume the strain in the bottom of the trenches based purely on the micro-ridge geometry (Fig. 4.10g).

4.4.3. Determining the Effect of FN Strain on C2C12 Myoblast Adhesion

Since we determined that we could reasonably estimate FN strain simply by modulating the micro-ridge geometry, we used this approach to determine how FN strain would affect C2C12 cell adhesion. We have previously shown that primary chick cardiomyocytes are capable of growing and aligning along PoT printed lines on PDMS micro-ridges (Fig. 4.11a and b). However, when the micro-ridges were isotropically coated (not PoT printed in this case), we found that the cells grew and aligned in the direction of the micro-ridges[161] (Fig. 4.11c and d). Since we wanted to avoid cell interactions with the vertical sidewalls, we therefore PoT printed FN sheets that were 1 cm x 1 cm to fully cover the micro-ridges and ultimately to influence the cells to adhere, migrate, and align in the axis of the micro-ridges and therefore avoid the sidewalls.

The PDMS micro-ridges used in this study were either 50 μm wide or 75 μm and had depths of 10 μm (Fig. 4.12a and b) and ~40 μm (Fig. 4.12c and d). The low aspect ratio, 10 μm deep micro-ridges allowed us to test cell adhesion to FN under low strain (40% and 27% for the 50 μm and 75 μm wide micro-ridges, respectively). Increasing the aspect ratio of the micro-ridges by engineering micro-ridges that were 40 μm deep allowed us to investigate the C2C12 response to FN under high strain (160% and 106% for the 50 μm and 75 μm wide micro-ridges, respectively).

After seeding the C2C12 cells in serum-free media for 2 hours, we observed depth-dependent differences in cell area. In all cases, the C2C12 cells were well spread on the micro-ridge tops (Fig. 4.12e-h). On the 50 μm wide, 10 μm deep micro-ridges (Fig. 4.12e), there was a significant decrease in cell spreading area from 1183.51 ± 525.26 μm^2 (n= 40 cells across a minimum of 3 substrates) on the micro-ridge top to 784.17 ± 386.27 μm^2 (n = 42 cells across a minimum of 3 substrates) on the trench bottom (4.12i). When the depth of the micro-ridges was increased to 40 μm (Fig. 4.12f), the decrease in cell

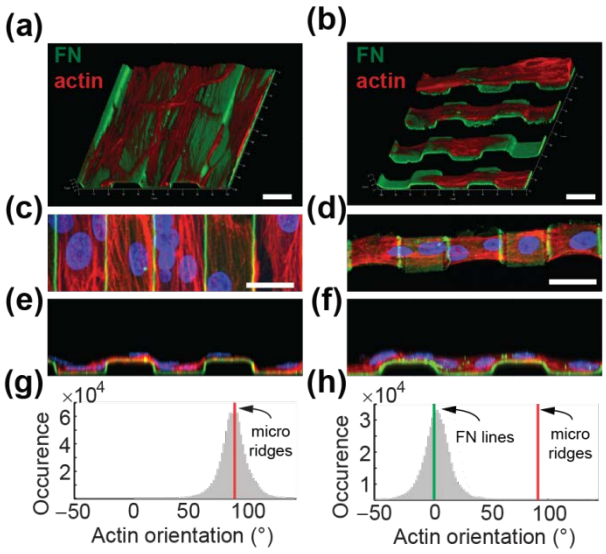

Fig. 4.11. Directed cell alignment on substrates with uniform FN coating or PoT printed, orthogonal FN lines. 20 µm wide, 20 µm spaced, and 5 µm tall PDMS micro-ridges were (a) uniformally coated with FN (green) or (b) PoT printed with orthogonal 20 µm wide FN lines. The substrates were subsequently seeded with primary chick cardiomyocytes and stained for nuclei (blue) and actin (red). Top-down views of the cells on the micro-ridges suggests that they are aligned (c) in the axis of the micro-ridges on uniformly coated micro-ridges, and (d) along the FN lines when orthogonally PoT printed onto the micro-ridges. (e-f) cross-sections of the areas in (c-d). Measuring the actin alignment of the cardiomyocytes seeded on both substrates confirms that they are oriented (g) in the axis of the micro-ridges on when uniformly coated and (h) in the axis of the FN lines when PoT printed orthogonal to the micro-ridges. Scale bars are 20 µm.

spreading area was even more substantial. The cell spreading decreased from 1274.88 ± 722.71 μm^2 (n = 37 cells across a minimum of 3 substrates) on the ridge top to 447.43 ± 282.53 μm^2 (n = 66 cells across a minimum of 3 substrates) for cells on the trench bottom.

When C2C12 cells were seeded onto 75 µm wide, 10 µm deep micro-ridges (Fig. 4.12g) we did not observe any significant differences in C2C12 spreading area (n = 31 cells on the ridge top and n = 26 cells on the trench bottom across a minimum of 3 substrates). This could be attributed to the FN fibers being strained solely on the sidewalls, particularly because the micro-ridges had a very low aspect ratio (0.13 depth:width aspect ratio).

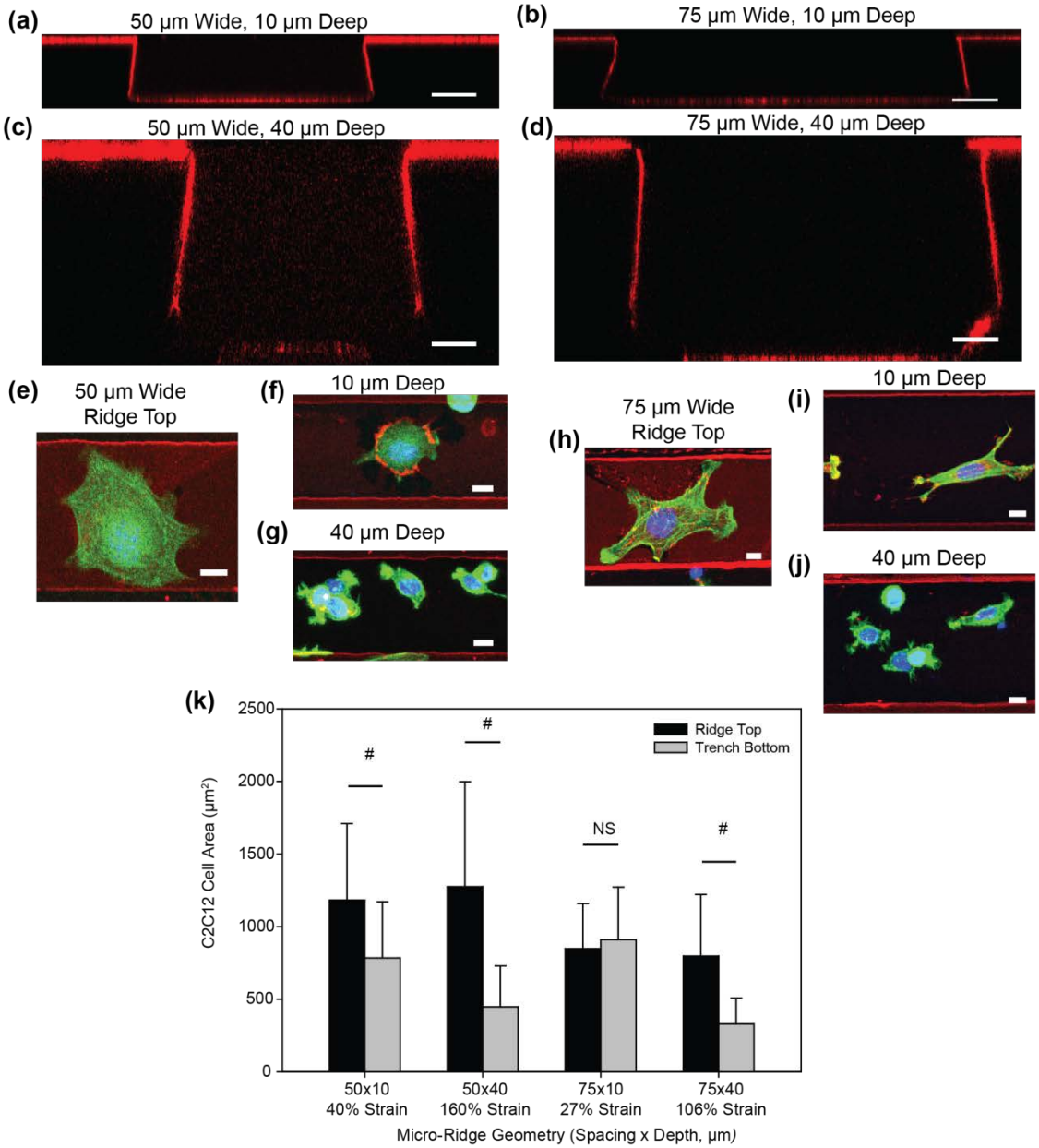

Fig. 4.12 Measuring the C2C12 spreading area on low and high aspect ratio micro-ridges. PDMS micro-ridges were engineered to be either low or high aspect ratio. The low aspect ratio micro-ridges were 10 µm deep and spaced either (a) 50 µm or (b) 75 µm, correlating to strains of 40% and 27% in the trenches, respectively. The high aspect ratio micro-ridges had depths of ~40 µm and were spaced either (c) 50 µm or (d) 75 µm, correlating to strains of 160% and 106% in the trenches, respectively. (e) Representative image of a C2C12 cell adhered to the 50 µm wide ridge top. Representative images from the (f) 10 µm and (h) 40 µm deep trench bottoms indicates a progressive decrease in cell spreading. (h) A representative image of a cell adhered to the 75 µm wide ridge top. Representative images of cells adhered to the (i) 10 µm deep and (j) 40 µm deep trench bottoms show a progressive decrease in cell spreading. (k) Quantification of the C2C12 spreading area for each of the micro-ridge geometries. '#' indicates a statistically significant difference with $P<0.05$ using a one-way ANOVA rank sum test with a Dunn's pairwaise comparison. Cells were stained for actin (green) and nuclei (blue) and the FN was fluorescently labeled (red).

When the depth of the micro-ridges was increased to 40 μm (Fig. 4.12h) we noticed a significant decrease in cell spreading area from 796.69 ± 424.47 μm^2 (n = 65 cells across a minimum of 3 substrates) on the ridge tops to 329.95 ± 177.89 μm^2 on the trench bottoms (n = 132 cells across a minimum of 3 substrates). Altogether, with increasing micro-ridge aspect ratio, we observed a marked decrease in cell spreading area.

We have previously shown that FN fibers prepared using SIA become less dense when highly strained (Fig. 3.5b), therefore we also wanted to confirm that a decrease in the overall FN density and available cell adhesion binding sites was not also contributing to the observed decrease in cell spreading. To test this, we PoT printed 50 μm wide FN lines onto flat PDMS that were prepared using decreasing solution concentrations of FN in the microcontact printing step of PoT (Fig. 4.1a). When coating the stamps with a FN solution, we used concentrations of 50 μg/mL, 10 μg/mL, and 5 μg/mL (Fig. 4.13). Prior work in the literature has shown that these coating densities should allow us to achieve a final FN surface densities that are roughly half (10 μg/mL) and a quarter (5 μg/mL) of the high density (50 μg/mL) FN surface density[165] following microcontact printing.

To confirm that the density of FN was actually less following microcontact printing onto PIPAAm, we scanned the FN fibers in the as-patterned state using AFM and measured their surface coverage. Qualitatively, using both the AFM height (Fig. 4.13a-c) and phase (Fig. 4.13d-f) it is clear that there is a decrease in the surface coverage of FN when using different solution concentrations of FN. FN microcontact printed from stamps coated in a FN solution with a concentration of 50 μg/mL resulted in a dense, fibrous, and interconnected network (Fig. 4.13a and d). Previous work (Chapter 2, Fig. 2.5) has shown that the smallest fibrils in this arrangement are on the order of ~3 nm in diameter. Additionally, the height of these interconnected fibrils is ~4 nm. The nanostructure of FN microcontact printed by stamps coated in a 10 μg/mL FN solution maintained a fibrous morphology yet it was noticeably less dense (Fig. 4.12b and e). The fibrils within the nanostructure also appeared to be thicker than the fibrils observed in the high density surface coverage. Moreover, the height of these fibrils within the nanostructure was

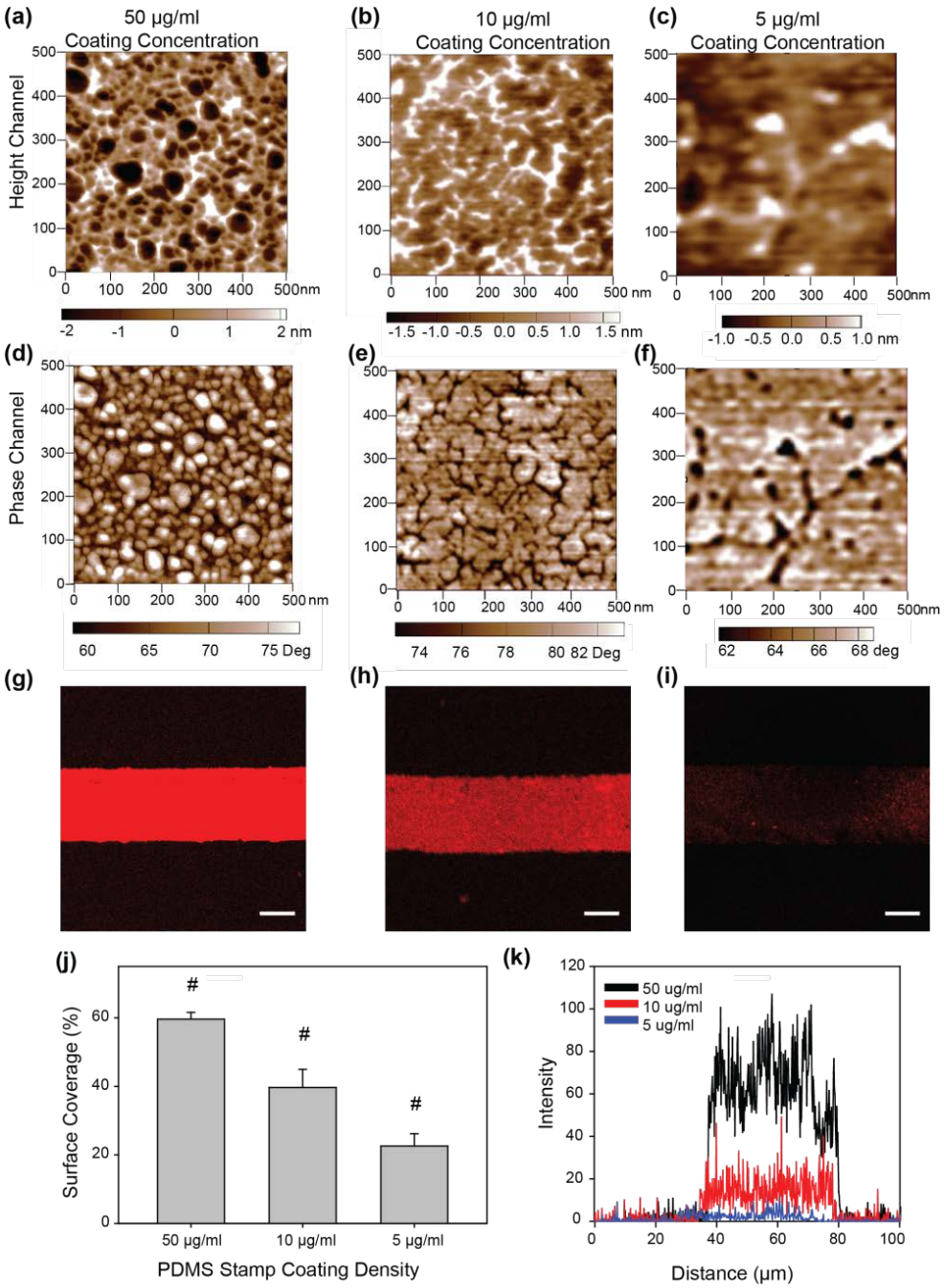

Fig. 4.13. Quantifying the effect of decreasing the concentration of FN in solution on the FN surface density following microcontact printing and PoT. PDMS stamps were coated with FN at concentrations of 50 µg/mL, 10 µg/mL, and 5 µg/mL and microcontact printed onto PIPAAm. (a-c) Representative AFM height channel images of the FN pattern that was prepared using 50 µg/mL, 10 µg/mL, and 5 µg/mL FN concentrations. (d-f) Representative phase signal images provided of the three FN surface densities. The FN patterns were then transferred to flat PDMS surfaces and imaged using confocal microscopy. (g-i) Representative fluorescent images of the FN line patterns prepared usingv50 µg/mL, 10 µg/mL, and 5 µg/mL. The imaging conditions were held constant. (j) Quantification of the surface coverage on PIPAAm by AFM. The symbol # indicates a statistically significant difference with $P<0.001$ using a one-way ANOVA with Tukey's pairwise comparison. (k) Profile plots of the fluorescent FN line patterns prepared using the three different FN solution concentrations. Scale bars are 20 µm.

~3 nm. When the lowest concentration of FN (5 μg/mL) was coated onto a PDMS stamp and microcontact printed onto PIPAAm, we qualitatively observed a further decrease in the FN surface coverage (Fig. 4.13c and f). Compared to the fibrils previously discussed, these fibrils were wider but their height was smaller, on the order of ~2 nm. Interestingly, it appears that the solution concentration of FN may affect how FN dimers become surface adsorbed. Next, to confirm that these fibers could be transferred to a flat PDMS surface via PoT, we fluorescently tagged 40% of the FN in solution with an alexa fluor 546 dye (Fig. 4.13g-i) and then released the FN fibers onto a PDMS substrate. Using a confocal microscope, we imaged each set of FN fibers using the same imaging parameters. We found that the fluorescence intensity lower for each decrease in solution concentration of FN prior to microcontact printing. Because the line widths were maintained, we confirmed that we were able to transfer the FN lines of different surface coverage (density) to the flat PDMS substrates via PoT. Finally, to quantitatively assess to decrease in FN surface coverage we first measured the surface coverage on PIPAAm using AFM at high resolution (Fig. 4.13j). We found that the mean surface coverage was initially 59.63 ± 1.96 % when microcontact printed by stamps coated with a FN solution of 50 μg/mL. When we decreased the concentration of FN in solution to10 μg/mL, we found the surface coverage on PIPAAm following microcontact printing deceased to 39.67 ± 5.31%. Furthermore, using the low concentration, 5 μg/mL FN solution, the surface coverage was 22.57 ± 3.61%. We then measured the mean fluorescence intensity for each FN surface density using ImageJ[142]. When we analyzed the fluorescent images following PoT onto PDMS (Fig. 4.13k), the mean fluorescence intensity was initially 68.12 ± 13.71 for PoT printed FN fibers that had been prepared using a 50 μg/mL FN solution concentration. The mean fluorescence intensity subsequently decreased to 14.22 ± 6.26 and 3.73 ± 2.34 for when 10 μg/mL and 5 μg/mL were used, respectively.

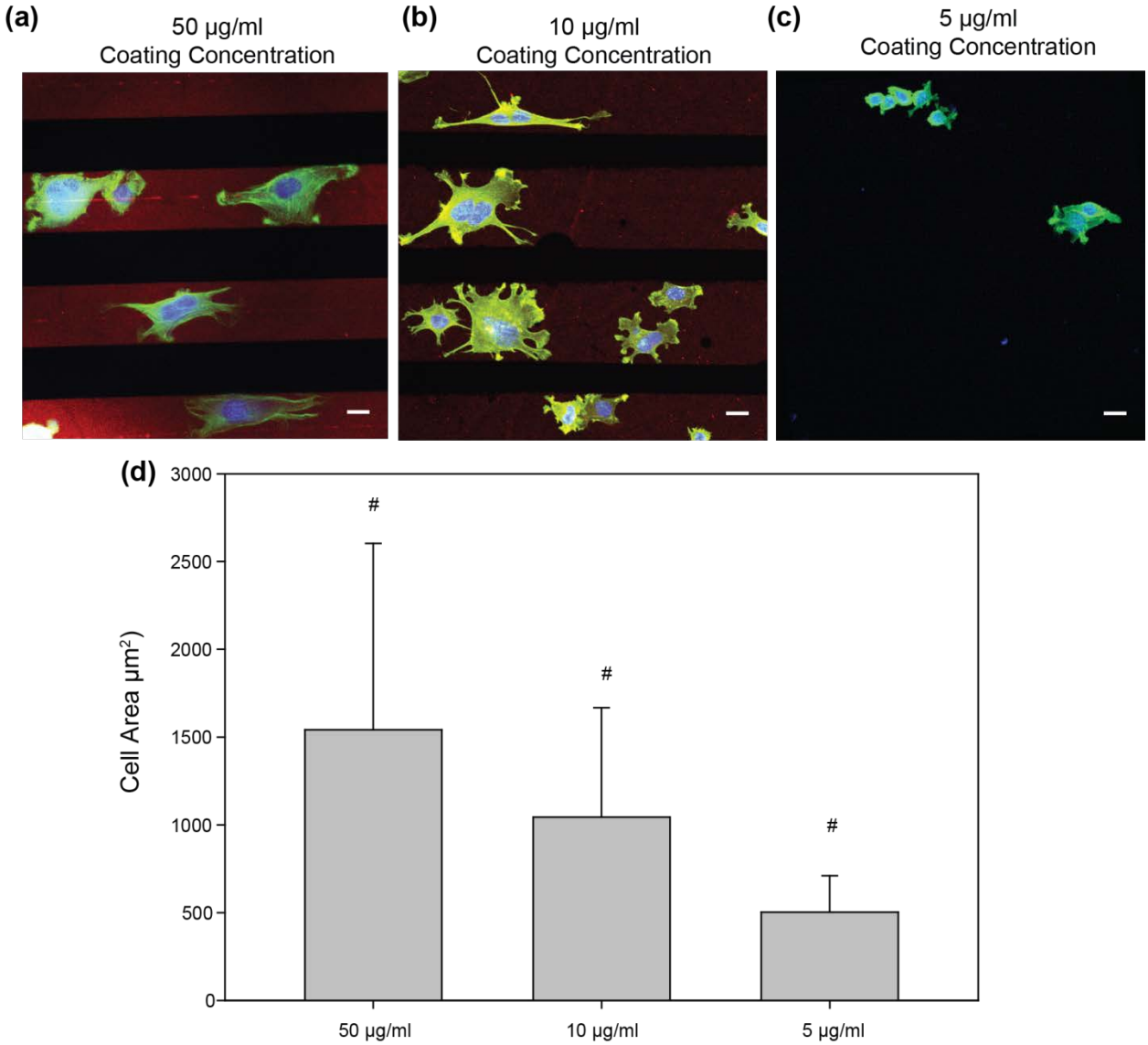

Fig. 4.14 C2C12 spreading area on FN line patterns prepared using different concentrations of FN in solution. Representative images of cells adhered to 50 µm wide FN lines that were prepared using (a) 50 µg/mL (b) 10 µg/mL, and (c) 5 µg/mL FN solution concentrations. (d) The cell areas as a function FN lines prepared using different solution concentrations. # indicates a statistically significant difference with $P < 0.05$ using a one-way ANOVA rank sum test with a Dunn's pairwise comparison. Cells were stained for actin (green) and nuclei (blue) and the FN was fluorescently tagged (red). Scale bars are 20 µm.

Next, we seeded C2C12 cells onto FN lines of different FN density to investigate how decreases in FN density may affect cell spreading. After a 2 hour culture period in serum-free media, we indeed observed density dependent differences in cell spreading area (Fig. 4.14). Cells adhered to high density

FN lines (50 μg/mL coating concentration) had an average spreading area of 1541.33 ± 1061 μm^2 (Fig.4.14a and d, n = 50 cells across 3 separate substrates). C2C12 cells seeded on FN lines that used a 10 μg/mL solution concentration prior to PoT, had a decreased cell spreading area of 1044.01 ± 623.51 μm^2 (Fig. 4.14b and d, n = 96 cells across 3 separate substrates). Finally, on the low density FN lines, several samples did not have any adherent cells following a 2 hour culture period in serum-free media. Of the adherent cells, the average spreading area was 502.31 ± 207.93 μm^2 (Fig. 4.14c and d, n = 7 across a 4 separate substrates). While there was a decrease in C2C12 spreading area as a function of FN density, the decrease was much less than between cells cultured on micro-ridge tops (unstrained FN) and trench bottoms of high aspect ratio micro-ridges (FN strain >100%).

Several studies have demonstrated that FN fibers exhbit mechanosenstive properties in which cryptic cysteine amino acid residues[119], bacterial adhesion sites[42], sites for collagen interactions[41], and the site for $\alpha_5\beta$1integrin receptors[36] are all regulated by strain. Using PoT to strain FN fibers, we wanted to determine whether low aspect ratio (50 and 75 μm wide, 10 μm deep) and high aspect ratio (50 and 75 μm wide, 40 μm deep) would affect the activity of α_5 integrin receptors in C2C12 myoblasts. Based on the micro-ridge geometries, the low aspect ratio micro-ridges would impose strains of ~40% and ~27% whereas the high aspect ratio micro-ridges would impse strains of ~160% and 106% for 50 μm wide and 75 μm micro-ridges, respectively.

We seeded C2C12 cells onto the low and high aspect ratio micro-ridges that were PoT printed with FN sheets and cultured them for 2 hours in serum-free media. Cells that were adhered to the micro-ridge tops (Fig. 4.15a-c) exhibited robust α_5 integrin expression in the form of a fibrous plaque that started at the periphery of the cell and persisted towards the center of the cell. C2C12 cells adhered to the trench bottom of low aspect ratio PDMS micro-ridges (strains <50%, Fig. 4.15d-f) had smaller α_5 integrin plaques that varied more from cell to cell but still managed to be present throughout the cell body.

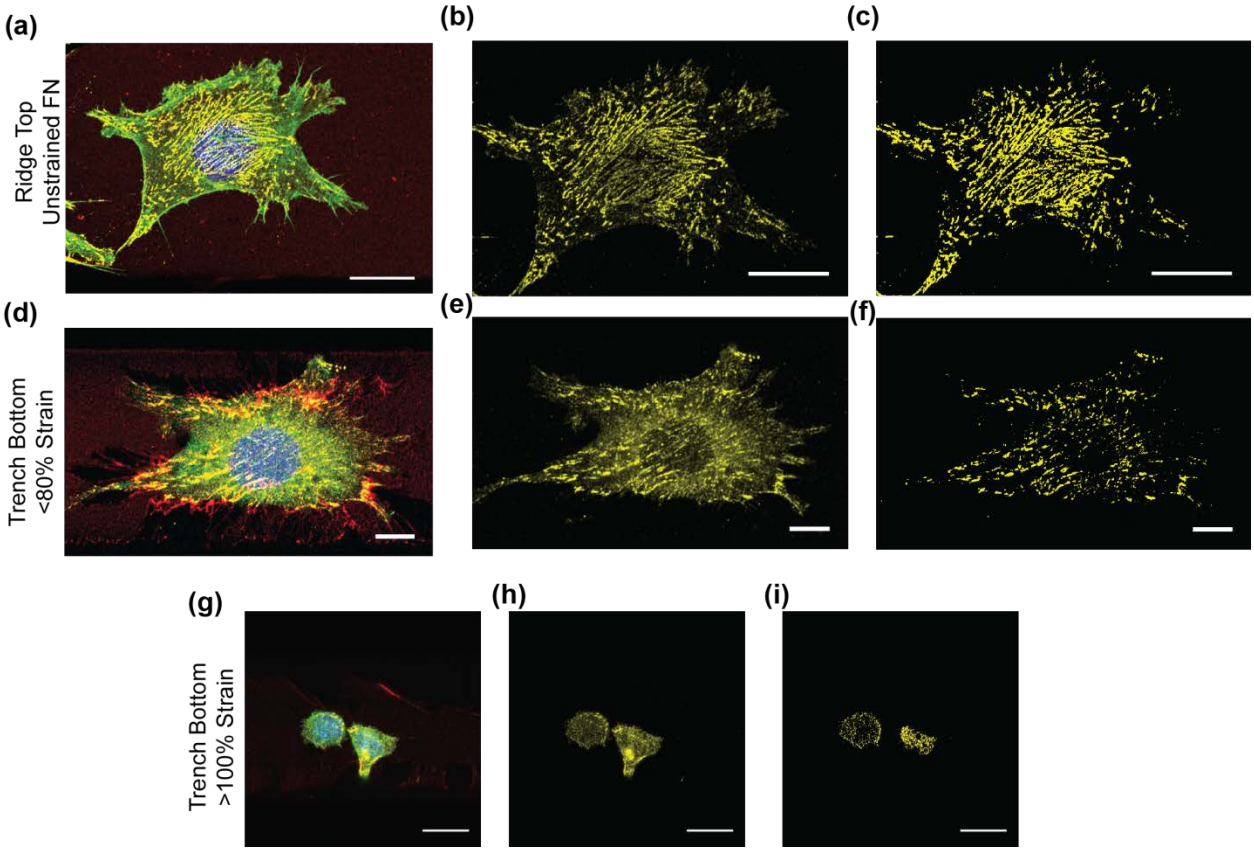

Fig. 4.15 The α_5 integrin expression for cells seeded on low and high aspect ratio micro-ridges. (a) Representative image of a cell adhered to the ridge top. (b) Image of same cell showing only the α_5 integrin fluorescence and (c) the same image following segmentation. (d) A representative image of a cell adhered to trench of low aspect ratio micro-ridges. (e) Image of the same cell in (d) except only the α_5 channel is showing. (f) Image of the α_5 fluorescence channel following segmentation. (g) A representative image of cells adhered to the trench of high aspect ratio micro-ridges. (h) An image showing only the α_5 fluorescence channel and (i) following segmentation. Cells were fluorescently stained for actin (green), nuclei (blue), and α_5 integrin (yellow). The fibronectin was also fluorescently labeled (red). Scale bars are 10 μm.

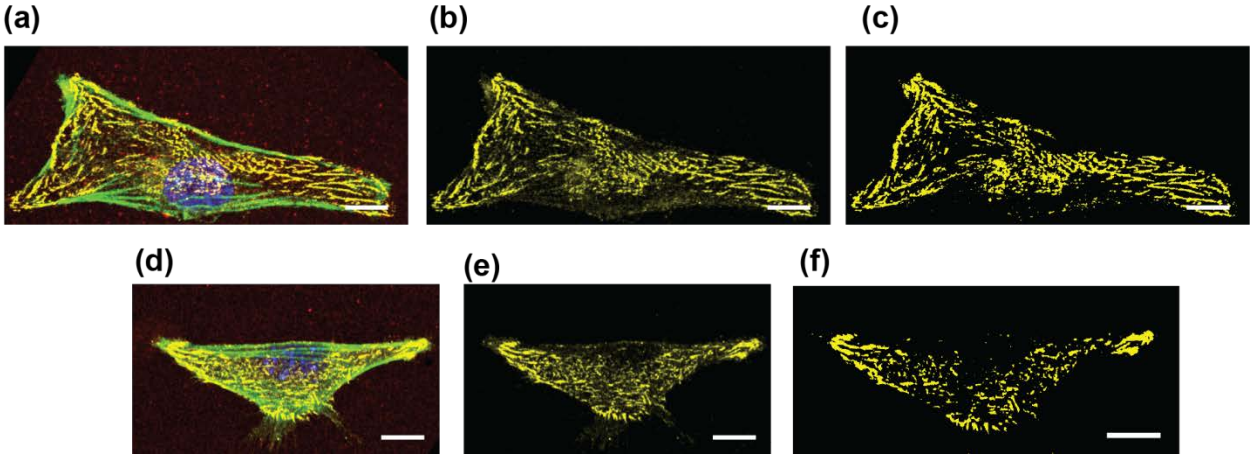

Fig. 4.16 Quantification of the α_5 integrin expression for cells seeded on unstrained FN with different surface coverage. FN at a concentration of 50 μg/mL was used to prepare FN sheets that were then PoT printed onto flat PDMS preserving the as-patterned, unstrained nanostructure. (a) A representative image of a cell adhered to the FN sheet. (b) Image of the same cell showing only the α_5 fluorescence channel and (c) the same cell with the following segmentation to remove background signal. FN at a concentration of 10 μg/mL was then used to prepare PoT printed FN sheets on flat PDMS. (d) a representative image of a cell adhered to the FN sheet. (e) The same cell with showing only the α_5 fluorescent channel. (f) The cell following segmentation to remove background signal. Cells were fluorescently stained for actin (green), nuclei (blue), and α_5 integrin (yellow). The fibronectin was also fluorescently labeled (red). Scale bars are 10 μm.

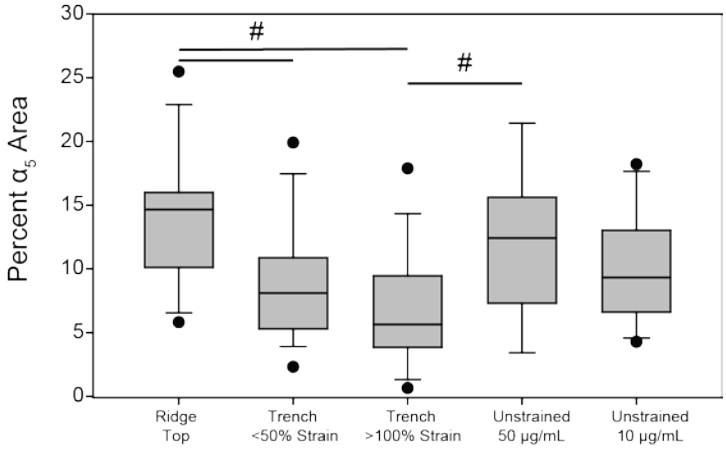

Fig. 4.17. Quantifying the normalized α_5 integrin area for cells seeded on micro-ridges and seeded on FN sheets with different FN density. The normalized α_5 area was quantified for cells adhered to the micro-ridge tops, the trenches of low (<50% strain) and high (>100% strain) aspect ratio micro-ridges, and to unstrained FN sheets prepared using 50 µg/mL and 10 µg/mL solutions of FN. The symbol '#' indicates a statistically significant difference with $P<0.05$ following a one-way ANOVA on ranks with a Dunn's pairwise comparison.

Finally, when seeded on the high aspect ratio micro-ridges that were 50 µm wide, 40 µm deep and 75 µm wide and 40 µm deep (strains>100%, Fig. 4.15g-i), we found that the α_5 integrin expression was mostly punctate and did not form α_5 plaques that were observed in cells adhered to the micro-ridge tops.

To determine the effect of decreasing FN concentration on α_5 integrin expression we also seeded cells onto FN sheets that were prepared using 50 µg/mL and 10 µg/mL solution concentrations of FN (~60% FN surface coverage and ~40% FN surface coverage, respectively) and PoT printed directly onto flat PDMS thereby preserving their unstrained state. After a 2 hour culture in serum-free media, the cells exhibited slight density dependence on α_5 integrin expression. Cells adhered to the FN sheets prepared using a 50 µg/mL solution concentration of FN exhibited robust α_5 adhesion plaques, similar to the cells seeded on the micro-ridge tops (Fig. 4.16a-c). Cells seeded on the lower density FN sheets prepared using a 10 µg/mL solution concentration of FN still maintained had a α_5 integrin expression that varied from cell to cell but was consistently more concentrated on the periphery of the cell (Fig. 4.16-d-f).

To quantify our findings observations of α_5 integrin expression, we measured the α_5 area normalized to the spread area of each cell (Fig. 4.17). This was all performed based off of the α_5

fluorescent channel in confocal images (Fig. 4.15b, e, h and Fig. 4.16b and e) that was then segmented to remove background signal (Fig.15c, f, I and Fig. 4.16c and f). Cells adhered to the micro-ridge tops (Fig. 4.15a-c) had an α_5 area fraction of 13.90 ± 5.53% of the total cell area (Fig. 4.17, n = 26 cells across a minimum of 5 substrates). For cells adhered to the trenches of low aspect ratio micro-ridges (Fig. 4.15d-f, strain <50%) we found that the mean α_5 area relative to the total cell area was 8.58 ± 4.58% (n = 21 cells across a minimum of 5 substrates). Moreover, cells adhered to the trenches of high aspect ratio micro-ridges (Fig. 4.15g-i, >100% strain) the normalized α_5 was 6.72 ± 4.64% (Fig. 4.17, n = 27 cells across a minimum of 5 substrates). Finally, to compare to unstrained FN sheets that were prepared with high (50 μg/mL) and lower (10 μg/mL) concentrations of FN, we found that the normalized α_5 area was 11.95 ± 5.57% and 9.97 ± 4.28%, respectively (Fig. 4.17, n = 11 cells for FN sheets prepared using 50 μg/mL FN solution and n = 28 cells for FN sheets prepared using 10 μg/mL FN solution. Each was across a minimum of 4 substrates). Cells on the micro-ridge tops were found to contain a significantly higher portion of α_5 integrin relative to their cell area than cells seeded on both low aspect ratio (<50% strain) and high aspect ratio (>100% strain) micro-ridges. However, although the mean normalized α_5 area was higher for cells cultured on unstrained FN than on cells cultured on strained FN regardless of density, it was only significantly different between cells cultured on high density, unstrained FN and cells adhered to the trenches of high aspect ratio micro-ridges with strains >100%. While there is a trend that FN strain is reducing the overall α_5 integrin expression, we cannot overlook the contribution of decreased FN density as well and a more comprehensive analysis is needed.

4.5. Discussion

In this study we sought to investigate how FN fiber strain affected C2C12 myoblast adhesion and ultimately, integrin expression. While previous studies have demonstrated that FN fibers assembled in a cell-free system contain intrinsic mechanosensitive properties[36,41,42,53,59,81,82,119], these FN fibers are typically only several micrometers in diameter and therefore unsuitable as cell culture substrates. This is supported by previous work in our lab which demonstrated that C2C12 myoblasts differentiate optimally

on wider FN adhesive areas[170]. As a consequence, the majority of these studies have been limited to studying how FN strain affects the exposure of cryptic sites using small molecules and peptides. Other studies involving modified FN fragments or FN assembled on different surface chemistries have demonstrated that FN conformation can affect properties such as cell adhesion and differentiation[38,39,88,121] yet it is unclear whether a similar effect can be observed in full length FN fibers and in a force-induced manner.

We overcame the limitations inherent to other assembly techniques through the development of a PoT method[161]. Using this approach, we relied on the swelling action of a thermally dissolvable PIPAAm substrate to "push" FN fibers and sheets into geometrically defined PDMS micro-ridges (Fig. 4.1). The FN fibers and sheets maintained their width while being pushed into the micro-ridges making them suitable cell culture substrates. Additionally, the bulk material properties were constant (PDMS) leaving the imposed strain and FN density as the only differences between FN on the ridge tops and FN in the bottom of the trenches.

By increasing the PIPAAm layer thickness to ~40 μm, we were able to pattern very high aspect ratio and /or irregular topographies. Using PDMS micro-ridges as a model substrate we found that we could increase the depth:width aspect ratio up until ~2.4 (Fig. 4.4d). At this aspect ratio we began to observe that there were small gaps in the patterned FN lines. However, we were able to PoT print 37 μm deep and 20 μm wide micro-ridges with continuous FN lines without any break in the patterned FN (Fig. 4.4c and g). We previously demonstrated that the FN fibers are under an inherent prestress when microcontact printed onto PIPAAm and will fully contract by about half the initial length if released directly in solution (Chapter 3, Fig. 3.2). Accounting for this pre-stress by using the fully contracted length as the initial length, we could expect the fibers to be strained upwards of 800%, comparable to what we (Chapter 3, Fig. 3.4) and others have shown through tensile testing experiments with FN fibers[119,125]. Furthermore, we also observed that the FN lines had a decreased density in the trench

bottoms of the high aspect ratio ridges (Fig. 4.4j), which is similar to what we observed in FN fibers that were manually strained (Fig. 3.4).

To obtain a better estimate of the FN fiber strain in the trench bottoms compared to the micro-ridge tops, we employed a recently developed approach to tag the FN fibers with FN-based fiduciary marks (Fig.3.1). In our previous study we used 10 um wide, 10 um spaced fiduciary marks to measure strain, however we wanted a higher resolution measurement so we could determine if there were differences in FN strain depending on whether the FN was adhered to the sidewalls or trench bottom. Therefore, we engineered FN fibers to have 2 um wide, 2 um spaced fiduciary marks. Using this approach we found that strain was typically highest on the bottom of the sidewalls. This provided some explanation as to why the measured strain of the FN fibers in the trench bottom were lower than expected based on the micro-ridge geometry. In some cases, however, we measured a greater strain based on the center-to-center distance of the fiduciary marks of FN fibers in the trench bottoms compared to what was expected. We reason that this could be due to the integration of the fiduciary marks with the underlying FN fiber. If they fiduciary marks are not well integrated with the FN fiber, it is unclear whether they are capable of translocating along the length of the FN fiber. This is evident in some cases where the fiduciary mark width does not change with increasing strain. In total, while there is some mismatch between the expected strain based on the micro-ridge geometry and the measured strain based on the fiduciary marks, the two are generally in good agreement ($r^2 = 0.938$). Based on this, we can reasonably estimate the strain imposed on the FN fibers in the bottom of the trenches based on the micro-ridge geometry.

A major objective of this study was to determine whether FN strain was capable of altering its bioactivity and therefore affecting C2C12 myoblast adhesion. We hypothesized that strain would induce the decoupling of the synergy and RGD sites on the FN $III_{9\text{-}10}$ domains thereby significantly reducing the binding affinity of $\alpha_5\beta_1$ integrin receptors. A recent study has shown that, by limiting cells to use only β_1-class, α_v-class or both classes of integrins can affect a number of adhesive properties of fibroblasts including migration speed and spreading[87]. Specifically, cells able to use only α_v-class integrin receptors

were significantly less spread than cells expressing β_1-class integrins or both α_v-class and β_1-class integrins. Therefore, the first metric we used to measure the C2C12 response to FN strain was cell spreading area. We also wanted to limit cell interactions with the vertical sidewalls as that would complicate the area measurements. In our initial studies involving PoT, we found the primary chick cardiomyocytes adhered to and aligned along FN lines when PoT printed onto micro-ridges. However, when uniformly coated in FN, the cardiomyocytes were observed to align along the topography (Fig. 4.11). With this in mind, we PoT printed 1 cm x 1cm FN sheets to uniformly cover the entire micro-ridge area and avoid interactions between the cells and the sidewalls.

To test how C2C12 spreading area was dependent on whether they were adhered to the ridge tops or trench bottoms, we first used 2 low aspect ratio micro-ridges that were 75 μm and 50 μm wide and 10 μm deep correlating to an expected strain of ~26% and 40% relative to the FN on the micro-ridge tops (Fig. 4.12a and b). On the 75 μm wide micro-ridges, we found no difference in the cell spreading area. One explanation is that on very low aspect ratio topographies (especially 100 μm wide and 200 μm wide micro-ridges) most, if not all, of the FN strain occurs on the vertical sidewalls. This is further supported by experiments using fiduciary marks where the measured strain in the trenches of the 50 μm wide, 10 μm deep micro-ridges was smaller than expected based on the micro-ridge geometry (Fig. 4.10g). Conversely, C2C12 cells adhered to the trenches of micro-ridges that were 50 μm wide did exhibit a decrease in their spreading area although the strains were probably smaller than expected. Altogether, we suspect that the strain of the FN in the trenches of the 75 μm wide, 10 μm deep micro-ridges was likely negligible due to the strain occurring on the sidewalls whereas the 50 μm wide micro-ridges were narrow enough to impose a large enough strain to influence a difference in cell spreading area. By further increasing the depth of the micro-ridges to ~40 μm (Fig. 4.12c and d), we observed an even larger decrease in cell spreading area (Fig. 4.12k).

Since we have previously observed that applied strain decreases the density of constituent FN fibrils (Fig. 3.4 and Fig. 3.5b) we wanted to determine the contribution of FN density to the observed

decreases in cell spreading (Fig. 4.14). We tested this by PoT printing FN lines of different density onto flat PDMS where the FN would not be strained as when it is PoT printed onto micro-ridges. While we found that there was a density-dependence on cell spreading area, it was not as sharp of a decline as we observed with cells in the trenches. For example, using AFM we found that the surface coverage of the FN lines prepared by FN solution concentrations of 50 μg/mL and 10 μg/mL was ~59% and 39%, respectively. The average cell area on unstrained FN with a density of 39% (10 μg/mL solution FN conconcentation) was about 68% of the area of cells grown on high density FN (59% surface coverage). By comparison, cells adhered to the trench bottom of micro-ridges that were 50 μm wide and 40 μm deep had an average spread area of about 35% relative to cells adhered to the micro-ridge top. If we account for an inherent 2-fold prestrain, the total strain of the FN in the trench bottom would be on the order of ~380%. Based upon our AFM data of uniaxially strained FN fibers (Fig. 3.5) we could expect a FN surface coverage of ~33%, similar to that of the FN lines prepared using 10 μg/ml FN solution concentration to coat the PDMS stamps (Fig. 4.13j). In addition, because all of the fibronectin is comprised of 40% that are conjugated to an Alexa Fluor 546 fluorophore, we can use fluorescence intensity as a metric to further estimate FN density. When we PoT printed FN lines that were derived from FN solution concentrations of 50 μg/mL and 10 μg/mL, the fluorescence intensity decreased from 68.12 to 14.22. Thus, the fluorescence intensity of the lower FN density was ~20.87% than in the higher density FN lines (Fig. 4.13k). When FN sheets were PoT printed onto 75 μm wide, 40 μm deep micro-ridges, the fluorescence intensity decreased from 44.49 to 9.16, representing about 20.6% of the fluorescence intensity of the ridge tops (data not shown). Therefore, while there is likely large contribution from simply a decrease in FN density, we reason that other factors such as FN strain may also be contributing to the observed cell spreading behavior. We will discuss approaches to decouple FN density with FN strain in the future directions section (Chapter 5).

We also aimed to quantify the degree in which $\alpha_5\beta_1$ integrin interactions were altered in our PoT system. We have previously shown that in even highly strained FN fibers, there is a highly variable

nanostructure (Fig. 3.6) therefore it is unlikely we would achieve a complete elimination of $\alpha_5\beta_1$-FN interactions. C2C12 cells on the ridge top had the highest overall expression of α_5 integrin where it was associated with robust fibrillar plaques that started at the periphery of the cell and were persistent throughout the cell (Fig. 4.15a-c). Contrary to cells on the ridge tops, the α_5 expression of cells adhered to the trenches on both the low (<50% strain) and high aspect ratio micro-ridges (>100% strain) was markedly reduced (Fig. 4.15 d-i). Especially in the case of cells adhered to the trenches of high aspect ratio micro-ridges, the α_5 expression was mostly punctate. When we quantified the α_5 expression normalized to cell area we found that it was highest on the micro-ridge tops (13.90 ± 5.33%) and it progressively decreased in cells adhered to the trench bottom of low (8.58 ± 4.58%) and high (6.72 ± 4.64%, Fig. 4.17).

Similar to its effect on cell spreading area, we also found that a simple decrease in FN density had a contribution to the observed decrease in α_5 expression as well (Fig. 4.16). The α_5 integrin expression was not statistically different for cells cultured on FN sheets with different FN densities and in both cases, the mean α_5 expression was higher than that of cells cultured on strained FN in the trenches of both low (<50% strain) and high (>100% strain) aspect ratio micro-ridges (Fig. 4.17). While this may imply a trend, there were only statistically significant differences between the α_5 integrin expression in cells adhered to high density, unstrained FN sheets and cells adhered to the trenches of high aspect ratio (>100% strain) micro-ridges. Therefore we cannot rule out that FN density contributes to the observed decrease in the normalized α_5 area. We acknowledge that a more complete quantification of the integrin expression is needed to further validate our findings especially in order to decouple integrin expression from differences in FN density. However, more comprehensive analysis methods to measure protein and/or gene expression are difficult since there are two distinct populations of cells within a single substrate. Additionally, confirming that the conformation of the constituent FN molecules has changed in a manner similar to our analysis in Chapter 3 is difficult due to the geometric constraints of the sidewalls.

Approaches to remedy these technical boundaries are discussed in the Future Directions section (Chapter 5).

Finally, studies that have affected cell behaviors such as differentiation[38,39] and EMT[169,171] have accomplished this using FN adsorbed to surfaces or FN fragments with specific FN III domains. In these studies, the cells are presented with an arrangement of FN with relatively homogenous conformations and biological activity. Studies using electron microscopy and super-resolution stochastic optical reconstruction microscopy have demonstrated that the morphology and arrangement of FN fibers assembled by cells varies even along the same fiber[94,160]. Thus it is likely cells are presented with FN exhibiting a heterogeneous structure and biological activity. This is similar to what we observed in highly strained FN fibers that were manually stretched (Fig. 3.6.) and may also be the case with FN that has been strained onto the PDMS micro-ridges. Thus, determine whether mechanically-induced conformational changes are sufficient to affect behavior on a cellular level is important for furthering our knowledge of FN mechanobiology.

In summary, we developed a PoT method to enable the transfer of FN and other ECM proteins to a variety of complex and/or irregular substrate topographies. By engineering PDMS micro-ridges with defined spacing and width we were able to control the strain imposed on the FN fibers and sheets in the trenches between micro-ridges. We present evidence that strain-induced conformational changes coupled with strain-induced density changes both promote decreased C2C12 myoblast adhesion and α_5 integrin expression.

CHAPTER 5:

Conclusions and Future Directions

5.1. Conclusion

The major objective of this thesis was to study the mechanosensitive properties of FN, specifically how strain modulates both the structural and biological properties of FN. The work presented within this thesis provides new knowledge to further advance our understanding of FN mechanobiology. More broadly, this work also establishes the development of several methods that will enable future studies investigating how multiple cell types sense and respond to the strained state of FN and other multimodular proteins such as laminin. The development of thorough models of ECM mechanobiology has far reaching applications in biotechnology, tissue engineering, regenerative medicine, and drug development.

In chapter 2, it was shown that FN nanofibers underwent significant changes in length, width, and thickness during the SIA process. Despite these large dimensional changes, the nanofiber volume remained constant suggesting that the FN nanofibers behaved as incompressible materials over these strains. Using AFM at high resolution it was clear that morphological changes within the nanostructure drove the large changes in nanofiber length, width, and thickness. Specifically, FN nanofibers in a pre-release state had a nanostructure that was comprised of an overall isotropic, fibrillar network where the smallest detectable features were small FN fibrils with a width of ~3 nm. These fibrils were similar in size to unfolded FN dimers with secondary protein structure intact. Conversely, FN nanofibers in a post-release state had a nanostructure that was comprised of elliptically shaped nodules that were on the order of several hundred nanometers in major axis length. Furthermore, the FN nanofibers were also found to be insoluble when released in DOC detergent but soluble in SDS. These results suggest that the nanofibers prepared using SIA have sufficient FN-FN interactions to prevent DOC solubility but these interactions are purely non-covalent.

Chapter 3 built on the results of chapter 2 by analyzing the nanostructure of strained FN nanofibers, from fully contracted to highly strained. While previous studies in the literature were limited to observing the nanostructure of FN fibers in a few discrete states, the work presented in chapter 3

demonstrated how SIA can be modified to dynamically track force-induced changes in the FN nanofiber nanostructure. By developing a method to tag the 1 cm long FN nanofibers with FN-based fiduciary marks, it was possible to accurately measure strain, even when the PDMS supports used to strain the nanofibers moved out of the field of view of the microscope. Results demonstrate that the nanostructure of the nanofibers is dependent on strain. In fully contracted FN nanofibers, the nanostructure was comprised of large nodules in an isotropic arrangement. At maximum strain, the nanostructure was composed of an arrangement of highly aligned nodules in a 'beads-on-a-string' arrangement. The nodules ranged in size from ~40 nm in diameter down to ~24 nm in diameter. In these highly strained FN nanofibers there were also short segments without a significant nodular morphology. Altogether, this chapter was able to overcome prior limitations of FN fibers assembled on surfaces through the modification of SIA to investigate the dynamic reorganization of the FN nanofibers structure in response to applied forces.

Studies involving mechanically stretched FN fibers are typically unable to investigate the cell response to FN strain. This is largely because the FN fibers formed are <5 μm in diameter therefore making them not suitable as cell culture substrates. Thus, Chapter 4 had two major objectives. The first was to develop a platform that would: (1) strain FN nanofibers or FN sheets in a well-defined manner, and (2) provide a wide enough area to represent a suitable cell culture substrate. This was accomplished through the development of a PoT method in which a dissolvable PIPAAm layer "pushes" FN nanofibers and FN sheets onto geometrically well-defined PDMS micro-ridges. Through the use of fiduciary marks, it was found that there was a generally good agreement between micro-ridge geometry and FN strain. The next goal was to use this PoT approach to measure the relationship between FN strain and C2C12 myoblast adhesion and α_5 expression. While decreases in FN surface density were found to affect C2C12 adhesion, the response was amplified by cells cultured on strained FN. Furthermore, cells cultured on unstrained FN exhibited robust α_5 integrin-positive adhesion plaques whereas cells cultured on FN under low (<80%) and high (<100%) strain exhibited progressive decreases in α_5 expression.

Collectively, the work presented in this thesis provides evidence for how the conformation of FN dynamically changes in response to applied forces and, ultimately, how these conformational changes can regulate the bioactivity of FN leading to changes in cell behavior. Moreover, the SIA and PoT methods overcome limitations of other synthetic FN fiber assembly techniques which may be further exploited to accelerate our knowledge by which cells dynamically manipulate and respond to their microenvironment.

5.2.0. Future Directions

The methodologies developed and discussed in this thesis have enabled the ability to dynamically track how the properties of FN changes as a function of strain. During the preparation of this thesis, I have conceptualized several research directions that will serve to validate our initial findings and significantly progress our knowledge of the strain-induced activation/deactivation of different binding sites within FN. Most importantly, the future directions presented here are based on the technology and engineering methods developed in this thesis and therefore would not require a significant amount of "man-hours"—at least in theory.

In chapter 3, I discussed how we were able to track the morphology of the nanostructure of FN nanofibers from fully contracted to highly strained. As the strain increased, the nodule size progressively decreased and, at high strains, disappeared over short distances (Fig. 3.6). Using this approach, future work will measure how the different morphological features within the FN nanofibers correlates with the availability of different binding sites for growth factors, other ECM components, and cell receptors. A logical first step would be to test the differential binding affinity of monoclonal antibodies directed towards the heparin binding domain of FN. Chen et al[94] used high resolution scanning electron microscopy to reveal the nanostructure of cell-generated FN fibers. While a single fiber was found to have both nodular and smooth morphologies, only the nodular regions were capably of binding antibodies directed towards the heparin binding domain of FN. Chen et al used gold nanoparticles to identify antibody binding and we could use a modification of this protocol to achieve similar results. Simply: (1) strain FN nanonfibers according to the procedure documented in chapter 3; (2) Obtain a reference high

resolution AFM image; (3) incubate the FN nanofibers with monoclonal antibodies directed towards the heparin binding domain of FN; (4) incubate with secondary antibodies tagged to nanoparticles with well-defined size; and (5) rescan the FN fiber using AFM and compare resulting image to the reference image to determine whether the antibodies localize to specific regions within the FN nanofibers. These experiments will allow us to determine the specificity different ligands to different molecular morphologies of FN. Given that FN has been found to be in a more unfolded state in cancerous tissue[137,174], the approaches developed in chapter 3 could also serve as a test bed for the development of new therapeutics that localize to the unfolded state of FN, ultimately allowing them to accumulate in diseased tissue.

The development of the PoT method from chapter 4 provides exciting opportunities to investigate how strain affects cell-ECM interactions. There are several short- and long-range future directions that will validate the overall effectiveness and utility of the PoT method. For short-term future directions, I believe it is important to completely decouple FN density with FN conformational changes in order to validate our findings that FN strain plays a role in C2C12 spreading area and α_5 integrin expression. There are two ways this can be accomplished. The first is to resolve the nanostructure of the FN in the trenches to confirm that it has adopted a morphology similar to what we have observed in chapter 3. It would then also be possible to measure the surface coverage of FN more accurately. This is technically challenging since the micro-ridges would have to be wide enough for an AFM cantilever to fit inside for AFM imaging. Instead, I propose the use of removable micro-ridges such that they can be applied to a flat PDMS surface (or other material surface), and PoT can be performed. After PoT, the micro-ridges can be removed leaving behind arrays of strained FN on flat PDMS surfaces. The strategy is based on recent work by Ma et al[175] who engineered thin PDMS films with holes. By substituting rectangular slits in lieu of holes, it would be possible to engineer PDMS films that could function as temporary micro-ridges. After removal of the micro-ridges it would be possible to use AFM to analyze the morphology of the nanostructure as well as measure the FN surface coverage.

The second approach to decouple FN density with FN strain is to saturate the trench bottoms with strained FN. By performing PoT onto the same micro-ridges multiple times, I predict it would be possible to increase the FN surface coverage. This can be confirmed using the first approach described, ie. using AFM in combination with removable micro-ridges.

Additionally, it is important to further confirm differences in α_5 expression in a more comprehensive manner. Specifically, it would be beneficial to use qPCR and/or rtPCR to look at changes in gene and protein expression, respectively. In our current PoT method, this would be difficult since there are two distinct populations of cells, namely those adhered to the ridge top on unstrained FN and those adhered to the strained FN in the trenches. To analyze the expression levels of cells in the trenches it is imperative to prevent cell adhesion to the ridge tops. The easiest way to accomplish this is to remove the FN from the ridge-tops by scraping the stamps along a PDMS or polystyrene surface. AN alternate approach is to again use removable micro-ridges and seed the cells onto the strained FN that is left on the flat PDMS following micro-ridge removal.

Finally, while this thesis focused solely on FN using C2C12 cells, there are many other cell-ECM interactions that can be studied using the PoT approach presented here. For example, the SIA and PoT techniques have demonstrated the ability to engineer fibers from a number of ECM proteins in addition to FN including laminin, collagen IV, and fibrinogen. It would be interesting to investigate whether other ECM proteins exhibit mechanosensitive behavior. This thesis also only studied the interactions between FN and C2C12 myoblast cells. Another interesting future study would be to investigate the role of FN strain on epithelial-to-mesenchymal transition (EMT) in lung alveolar cells. It has been proposed that a differential integrin expression through the loss of $\alpha_5\beta_1$ binding affinity to FN triggers EMT[171]. Furthermore, this thesis only investigated the structural and biological properties using pFN. As mentioned in the introduction, another major class of FN is cFN which contains the inclusion of extra FN III domains (EDA, EDB). Investigating whether these extra domains affect the structural and/or

mechanosensitive properties FN may underlie the *in vivo* functions of these domains and why they are upregulated during embryonic development, at sites of inflammation, and in tumors.

In summary, the short and long term future directions discussed herein will provide further validation of the key findings within this thesis as well as enable a more broad investigation of ECM mechanobiology using several ECM components and cell types.

6. References

1 Kass, L., Erler, J. T., Dembo, M. & Weaver, V. M. Mammary epithelial cell: influence of extracellular matrix composition and organization during development and tumorigenesis. *The international journal of biochemistry & cell biology* 39, 1987-1994 (2007).

2 Davidson, L. A., Dzamba, B. D., Keller, R. & DeSimone, D. W. Live imaging of cell protrusive activity, and extracellular matrix assembly and remodeling during morphogenesis in the frog, Xenopus laevis. *Developmental Dynamics* 237, 2684-2692 (2008).

3 Keller, R., Davidson, L. A. & Shook, D. R. How we are shaped: the biomechanics of gastrulation. *Differentiation* 71, 171-205 (2003).

4 Adams, J. C. & Watt, F. M. Regulation of development and differentiation by the extracellular matrix. *DEVELOPMENT-CAMBRIDGE-* 117, 1183-1183 (1993).

5 Krieg, M. *et al.* Tensile forces govern germ-layer organization in zebrafish. *Nature cell biology* 10, 429-436 (2008).

6 Hutson, M. S. *et al.* Forces for morphogenesis investigated with laser microsurgery and quantitative modeling. *Science* 300, 145-149 (2003).

7 Nelson, C. M. & Bissell, M. J. Of extracellular matrix, scaffolds, and signaling: tissue architecture regulates development, homeostasis, and cancer. *Annual review of cell and developmental biology* 22, 287 (2006).

8 Lu, P., Weaver, V. M. & Werb, Z. The extracellular matrix: A dynamic niche in cancer progression. *The Journal of Cell Biology* 196, 395-406, doi:10.1083/jcb.201102147 (2012).

9 Bissell, M., Kenny, P. & Radisky, D. in *Cold Spring Harbor symposia on quantitative biology.* 343-356 (Cold Spring Harbor Laboratory Press).

10 Kim, K. K. *et al.* Alveolar epithelial cell mesenchymal transition develops in vivo during pulmonary fibrosis and is regulated by the extracellular matrix. *Proceedings of the National Academy of Sciences* 103, 13180-13185 (2006).

11 Raghow, R. The role of extracellular matrix in postinflammatory wound healing and fibrosis. *The FASEB Journal* 8, 823-831 (1994).

12 Geiger, B., Bershadsky, A., Pankov, R. & Yamada, K. M. Transmembrane crosstalk between the extracellular matrix and the cytoskeleton. *Nat Rev Mol Cell Biol* 2, 793-805 (2001).

13 Berrier, A. L. & Yamada, K. M. Cell–matrix adhesion. *Journal of Cellular Physiology* 213, 565-573, doi:10.1002/jcp.21237 (2007).

14 Watt, F. M. & Huck, W. T. Role of the extracellular matrix in regulating stem cell fate. *Nature Reviews Molecular Cell Biology* 14, 467-473 (2013).

15 Engler, A. J., Sen, S., Sweeney, H. L. & Discher, D. E. Matrix elasticity directs stem cell lineage specification. *Cell* 126, 677-689 (2006).

16 Discher, D. E., Janmey, P. & Wang, Y.-l. Tissue cells feel and respond to the stiffness of their substrate. *Science* 310, 1139-1143 (2005).

17 Bettinger, C. J., Langer, R. & Borenstein, J. T. Engineering substrate topography at the micro-and nanoscale to control cell function. *Angewandte Chemie International Edition* 48, 5406-5415 (2009).

18 Diehl, K., Foley, J., Nealey, P. & Murphy, C. Nanoscale topography modulates corneal epithelial cell migration. *Journal of Biomedical Materials Research Part A* 75, 603-611 (2005).

19 Vogel, V. & Sheetz, M. Local force and geometry sensing regulate cell functions. *Nat Rev Mol Cell Biol* 7, 265-275 (2006).

20 Chen, C. S., Mrksich, M., Huang, S., Whitesides, G. M. & Ingber, D. E. Micropatterned surfaces for control of cell shape, position, and function. *Biotechnology Progress* 14, 356-363 (1998).

21 Chen, C. S., Mrksich, M., Huang, S., Whitesides, G. M. & Ingber, D. E. Geometric control of cell life and death. *Science* 276, 1425-1428 (1997).

22 Mrksich, M. *et al.* Controlling cell attachment on contoured surfaces with self-assembled monolayers of alkanethiolates on gold. *Proceedings of the National Academy of Sciences* 93, 10775-10778 (1996).

23 Chang, S. S., Guo, W.-h., Kim, Y. & Wang, Y.-l. Guidance of cell migration by substrate dimension. *Biophysical journal* 104, 313-321 (2013).

24 Lo, C.-M., Wang, H.-B., Dembo, M. & Wang, Y.-l. Cell movement is guided by the rigidity of the substrate. *Biophysical journal* 79, 144-152 (2000).

25 Pelham, R. J. & Wang, Y.-l. Cell locomotion and focal adhesions are regulated by substrate flexibility. *Proceedings of the National Academy of Sciences* 94, 13661-13665 (1997).

26 Burdick, J. A. & Vunjak-Novakovic, G. Engineered microenvironments for controlled stem cell differentiation. *Tissue Engineering Part A* 15, 205-219 (2008).

27 Khetan, S. *et al.* Degradation-mediated cellular traction directs stem cell fate in covalently crosslinked three-dimensional hydrogels. *Nature materials* 12, 458-465 (2013).

28 Martinac, B. Mechanosensitive ion channels: molecules of mechanotransduction. *Journal of Cell Science* 117, 2449-2460 (2004).

29 Morris, C. E. Mechanosensitive ion channels. *Journal of Membrane Biology* 113, 93-107 (1990).

30 Yao, M. *et al.* Mechanical activation of vinculin binding to talin locks talin in an unfolded conformation. *Scientific reports* 4 (2014).

31 Grashoff, C. *et al.* Measuring mechanical tension across vinculin reveals regulation of focal adhesion dynamics. *Nature* 466, 263-266 (2010).

32 Wu, C., Keivenst, V. M., O'Toole, T. E., McDonald, J. A. & Ginsberg, M. H. Integrin activation and cytoskeletal interaction are essential for the assembly of a fibronectin matrix. *Cell* 83, 715-724 (1995).

33 Wierzbicka-Patynowski, I. & Schwarzbauer, J. E. The ins and outs of fibronectin matrix assembly. *Journal of Cell Science* 116, 3269-3276 (2003).

34 Schwarzbauer, J. E. & Sechler, J. L. Fibronectin fibrillogenesis: a paradigm for extracellular matrix assembly. *Current opinion in cell biology* 11, 622-627 (1999).

35 Singh, P., Carraher, C. & Schwarzbauer, J. E. Assembly of fibronectin extracellular matrix. *Annual review of cell and developmental biology* 26, 397 (2010).

36 Krammer, A., Craig, D., Thomas, W. E., Schulten, K. & Vogel, V. A structural model for force regulated integrin binding to fibronectin's RGD-synergy site. *Matrix Biology* 21, 139-147 (2002).

37 García, A. J., Vega, M. a. D. & Boettiger, D. Modulation of cell proliferation and differentiation through substrate-dependent changes in fibronectin conformation. *Molecular biology of the cell* 10, 785-798 (1999).

38 Keselowsky, B. G., Collard, D. M. & García, A. J. Surface chemistry modulates fibronectin conformation and directs integrin binding and specificity to control cell adhesion. *Journal of Biomedical Materials Research Part A* 66, 247-259 (2003).

39 Keselowsky, B. G., Collard, D. M. & García, A. J. Integrin binding specificity regulates biomaterial surface chemistry effects on cell differentiation. *Proceedings of the National Academy of Sciences* 102, 5953-5957 (2005).

40 Lin, F. *et al.* Fibronectin growth factor-binding domains are required for fibroblast survival. *Journal of Investigative Dermatology* 131, 84-98 (2011).

41 Kubow, K. E. *et al.* Mechanical forces regulate the interactions of fibronectin and collagen I in extracellular matrix. *Nat Commun* 6, doi:10.1038/ncomms9026 (2015).

42 Chabria, M., Hertig, S., Smith, M. L. & Vogel, V. Stretching fibronectin fibres disrupts binding of bacterial adhesins by physically destroying an epitope. *Nature communications* 1, 135 (2010).

43 George, E. L., Georges-Labouesse, E. N., Patel-King, R. S., Rayburn, H. & Hynes, R. O. Defects in mesoderm, neural tube and vascular development in mouse embryos lacking fibronectin. *Development* 119, 1079-1091 (1993).

44 Pankov, R. & Yamada, K. M. Fibronectin at a glance. *Journal of Cell Science* 115, 3861-3863 (2002).

45 Gailit, J. & Clark, R. A. Wound repair in the context of extracellular matrix. *Current opinion in cell biology* 6, 717-725 (1994).

46 Lin, F. *et al.* Fibronectin peptides that bind PDGF-BB enhance survival of cells and tissue under stress. *Journal of Investigative Dermatology* 134, 1119-1127 (2014).

47 Sawicka, K. M., Seeliger, M., Musaev, T., Macri, L. K. & Clark, R. A. Fibronectin Interaction and Enhancement of Growth Factors: Importance for Wound Healing. *Advances in Wound Care* (2015).

48 Julier, Z., Martino, M. M., De Titta, A., Jeanbart, L. & Hubbell, J. A. The TLR4 Agonist Fibronectin Extra Domain A is Cryptic, Exposed by Elastase-2; use in a fibrin matrix cancer vaccine. *Scientific reports* 5 (2015).

49 Zerlauth, G. & Wolf, G. Plasma fibronectin as a marker for cancer and other diseases. *The American Journal of Medicine* 77, 685-689, doi:http://dx.doi.org/10.1016/0002-9343(84)90366-8 (1984).

50 Kelsh, R. M., McKeown-Longo, P. J. & Clark, R. A. EDA fibronectin in keloids create a vicious cycle of fibrotic tumor formation. *Journal of Investigative Dermatology* 135, 1714-1718 (2015).

51 Leahy, D. J., Hendrickson, W. A., Aukhil, I. & Erickson, H. P. Structure of a fibronectin type III domain from tenascin phased by MAD analysis of the selenomethionyl protein. *Science* 258, 987-991 (1992).

52 Potts, J. R. & Campbell, I. D. Structure and function of fibronectin modules. *Matrix Biology* 15, 313-320 (1996).

53 Gao, M., Craig, D., Vogel, V. & Schulten, K. Identifying unfolding intermediates of FN-III 10 by steered molecular dynamics. *Journal of molecular biology* 323, 939-950 (2002).

54 Craig, D., Gao, M., Schulten, K. & Vogel, V. Tuning the mechanical stability of fibronectin type III modules through sequence variations. *Structure* 12, 21-30 (2004).

55 Schwarzbauer, J. E. Alternative splicing of fibronectin: three variants, three functions. *Bioessays* 13, 527-533 (1991).

56 Schwarzbauer, J. E. Fibronectin: from gene to protein. *Current opinion in cell biology* 3, 786-791 (1991).

57 Schwarzbauer, J. E., Tamkun, J. W., Lemischka, I. R. & Hynes, R. O. Three different fibronectin mRNAs arise by alternative splicing within the coding region. *Cell* 35, 421-431 (1983).

58 Tamkun, J. W. & Hynes, R. O. Plasma fibronectin is synthesized and secreted by hepatocytes. *Journal of Biological Chemistry* 258, 4641-4647 (1983).

59 Vogel, V. Mechanotransduction involving multimodular proteins: converting force into biochemical signals. *Annu. Rev. Biophys. Biomol. Struct.* 35, 459-488 (2006).

60 Wang, Y. *et al.* Plasma fibronectin supports hemostasis and regulates thrombosis. *The Journal of Clinical Investigation* 124, 4281-4293, doi:10.1172/jci74630 (2014).

61 Tomasini-Johansson, B. & Mosher, D. F. Plasma fibronectin concentration in inbred mouse strains. *Thrombosis and haemostasis* 102, 1278-1280, doi:10.1160/th09-03-0141 (2009).

62 Cho, J. & Mosher, D. Role of fibronectin assembly in platelet thrombus formation. *Journal of Thrombosis and Haemostasis* 4, 1461-1469 (2006).

63 Ni, H. *et al.* Plasma fibronectin promotes thrombus growth and stability in injured arterioles. *Proceedings of the National Academy of Sciences* 100, 2415-2419 (2003).

64 Moretti, F. A. *et al.* A Major Fraction of Fibronectin Present in the Extracellular Matrix of Tissues Is Plasma-derived. *Journal of Biological Chemistry* 282, 28057-28062, doi:10.1074/jbc.M611315200 (2007).

65 Fukuda, T. *et al.* Mice lacking the EDB segment of fibronectin develop normally but exhibit reduced cell growth and fibronectin matrix assembly in vitro. *Cancer research* 62, 5603-5610 (2002).

66 Manabe, R.-i., Oh-e, N., Maeda, T., Fukuda, T. & Sekiguchi, K. Modulation of Cell-adhesive Activity of Fibronectin by the Alternatively Spliced EDA Segment. *The Journal of Cell Biology* 139, 295-307, doi:10.1083/jcb.139.1.295 (1997).

67 Glukhova, M. A., Frid, M. G., Shekhonin, B. V., Balabanov, Y. V. & Koteliansky, V. E. Expression of fibronectin variants in vascular and visceral smooth muscle cells in development. *Developmental Biology* 141, 193-202, doi:http://dx.doi.org/10.1016/0012-1606(90)90114-X (1990).

68 Peters, J. H. & Hynes, R. O. Fibronectin Isoform Distribution in the Mouse I. The Alternatively Spliced EIIIB, EIIIA, and V Segments Show Widespread Codistribution in the Developing Mouse Embryo. *Cell Communication and Adhesion* 4, 103-125 (1996).

69 Astrof, S. *et al.* Direct Test of Potential Roles of EIIIA and EIIIB Alternatively Spliced Segments of Fibronectin in Physiological and Tumor Angiogenesis. *Molecular and Cellular Biology* 24, 8662-8670, doi:10.1128/mcb.24.19.8662-8670.2004 (2004).

70 White, E. S. & Muro, A. F. Fibronectin splice variants: understanding their multiple roles in health and disease using engineered mouse models. *IUBMB life* 63, 538-546 (2011).

71 Muro, A. F. *et al.* Regulated splicing of the fibronectin EDA exon is essential for proper skin wound healing and normal lifespan. *The Journal of Cell Biology* 162, 149-160 (2003).

72 Mostafavi-Pour, Z., Askari, J., Whittard, J. & Humphries, M. Identification of a novel heparin-binding site in the alternatively spliced IIICS region of fibronectin: roles of integrins and proteoglycans in cell adhesion to fibronectin splice variants. *Matrix Biology* 20, 63-73 (2001).

73 Schwarzbauer, J. E., Spencer, C. S. & Wilson, C. L. Selective secretion of alternatively spliced fibronectin variants. *The Journal of Cell Biology* 109, 3445-3453 (1989).

74 Danen, E. H. & Yamada, K. M. Fibronectin, integrins, and growth control. *Journal of Cellular Physiology* 189, 1-13 (2001).

75 Pankov, R. *et al.* Integrin Dynamics and Matrix Assembly Tensin-Dependent Translocation of α5β1 Integrins Promotes Early Fibronectin Fibrillogenesis. *The Journal of Cell Biology* 148, 1075-1090 (2000).

76 Woods, A., Longley, R. L., Tumova, S. & Couchman, J. R. Syndecan-4 Binding to the High Affinity Heparin-Binding Domain of Fibronectin Drives Focal Adhesion Formation in Fibroblasts. *Archives of Biochemistry and Biophysics* 374, 66-72, doi:http://dx.doi.org/10.1006/abbi.1999.1607 (2000).

77 Couchman, J. R. & Woods, A. Syndecan-4 and integrins: combinatorial signaling in cell adhesion. *Journal of Cell Science* 112, 3415-3420 (1999).

78 Martino, M. M. & Hubbell, J. A. The 12th–14th type III repeats of fibronectin function as a highly promiscuous growth factor-binding domain. *The FASEB Journal* 24, 4711-4721 (2010).

79 Wijelath, E. S. *et al.* Heparin-II Domain of Fibronectin Is a Vascular Endothelial Growth Factor-Binding Domain Enhancement of VEGF Biological Activity by a Singular Growth Factor/Matrix Protein Synergism. *Circulation research* 99, 853-860 (2006).

80 Matsuka, Y. V., Medved, L. V., Brew, S. A. & Ingham, K. C. The NH2-terminal fibrin-binding site of fibronectin is formed by interacting fourth and fifth finger domains. Studies with recombinant finger fragments expressed in Escherichia coli. *Journal of Biological Chemistry* 269, 9539-9546 (1994).

81 Li, B., Lin, Z., Mitsi, M., Zhang, Y. & Vogel, V. Heparin-induced conformational changes of fibronectin within the extracellular matrix promote hMSC osteogenic differentiation. *Biomaterials Science* 3, 73-84 (2015).

82 Hubbard, B., Buczek-Thomas, J. A., Nugent, M. A. & Smith, M. L. Heparin-dependent regulation of fibronectin matrix conformation. *Matrix Biology* 34, 124-131 (2014).

83 Leiss, M., Beckmann, K., Girós, A., Costell, M. & Fässler, R. The role of integrin binding sites in fibronectin matrix assembly in vivo. *Current opinion in cell biology* 20, 502-507, doi:http://dx.doi.org/10.1016/j.ceb.2008.06.001 (2008).

84 Mao, Y. & Schwarzbauer, J. E. Accessibility to the Fibronectin Synergy Site in a 3D Matrix Regulates Engagement of α 5β 1 versus α vβ 3 Integrin Receptors. *Cell communication & adhesion* 13, 267-277 (2006).

85 Mao, Y. & Schwarzbauer, J. E. Fibronectin fibrillogenesis, a cell-mediated matrix assembly process. *Matrix Biology* 24, 389-399 (2005).

86 Aota, S.-i., Nomizu, M. & Yamada, K. M. The short amino acid sequence Pro-His-Ser-Arg-Asn in human fibronectin enhances cell-adhesive function. *Journal of Biological Chemistry* 269, 24756-24761 (1994).

87 Schiller, H. B. *et al.* β1- and αv-class integrins cooperate to regulate myosin II during rigidity sensing of fibronectin-based microenvironments. *Nat Cell Biol* 15, 625-636, doi:10.1038/ncb2747

http://www.nature.com/ncb/journal/v15/n6/abs/ncb2747.html#supplementary-information (2013).

88 Petrie, T. A., Capadona, J. R., Reyes, C. D. & García, A. J. Integrin specificity and enhanced cellular activities associated with surfaces presenting a recombinant fibronectin fragment compared to RGD supports. *Biomaterials* 27, 5459-5470, doi:http://dx.doi.org/10.1016/j.biomaterials.2006.06.027 (2006).

89 Woods, A. & Couchman, J. R. Syndecan-4 and focal adhesion function. *Current opinion in cell biology* 13, 578-583 (2001).

90 Echtermeyer, F., Baciu, P. C., Saoncella, S., Ge, Y. & Goetinck, P. F. Syndecan-4 core protein is sufficient for the assembly of focal adhesions and actin stress fibers. *Journal of Cell Science* 112, 3433-3441 (1999).

91 Dovas, A., Yoneda, A. & Couchman, J. R. PKCα-dependent activation of RhoA by syndecan-4 during focal adhesion formation. *Journal of Cell Science* 119, 2837-2846 (2006).

92 Singer, I. I. The fibronexus: a transmembrane association of fibronectin-containing fibers and bundles of 5 nm microfilaments in hamster and human fibroblasts. *Cell* 16, 675-685, doi:http://dx.doi.org/10.1016/0092-8674(79)90040-0 (1979).

93 Chen, L. B., Murray, A., Segal, R. A., Bushnell, A. & Walsh, M. L. Studies on intercellular LETS glycoprotein matrices. *Cell* 14, 377-391, doi:http://dx.doi.org/10.1016/0092-8674(78)90123-X (1978).

94 Chen, Y., Zardi, L. & Peters, D. M. P. High-resolution cryo-scanning electron microscopy study of the macromolecular structure of fibronectin fibrils. *Scanning* 19, 349-355 (1997).

95 Schwarzbauer, J. E. Identification of the fibronectin sequences required for assembly of a fibrillar matrix. *The Journal of Cell Biology* 113, 1463-1473 (1991).

96 Ichihara-Tanaka, K., Maeda, T., Titani, K. & Sekiguchi, K. Matrix assembly of recombinant fibronectin polypeptide consisting of amino-terminal 70 kDa and carboxyl-terminal 37 kDa regions. *FEBS letters* 299, 155-158 (1992).

97 Johnson, K. J., Sage, H., Briscoe, G. & Erickson, H. P. The compact conformation of fibronectin is determined by intramolecular ionic interactions. *Journal of Biological Chemistry* 274, 15473-15479 (1999).

98 Huveneers, S., Truong, H., Fässler, R., Sonnenberg, A. & Danen, E. H. Binding of soluble fibronectin to integrin α5β1–link to focal adhesion redistribution and contractile shape. *Journal of Cell Science* 121, 2452-2462 (2008).

99 McDonald, J. A. *et al*. Fibronectin's cell-adhesive domain and an amino-terminal matrix assembly domain participate in its assembly into fibroblast pericellular matrix. *Journal of Biological Chemistry* 262, 2957-2967 (1987).

100 Fogerty, F. J., Akiyama, S. K., Yamada, K. M. & Mosher, D. F. Inhibition of binding of fibronectin to matrix assembly sites by anti-integrin (alpha 5 beta 1) antibodies. *The Journal of Cell Biology* 111, 699-708 (1990).

101 Sechler, J. L., Corbett, S. A. & Schwarzbauer, J. E. Modulatory roles for integrin activation and the synergy site of fibronectin during matrix assembly. *Molecular biology of the cell* 8, 2563-2573 (1997).

102 Wennerberg, K. *et al.* Beta 1 integrin-dependent and-independent polymerization of fibronectin. *The Journal of Cell Biology* 132, 227-238 (1996).

103 Yang, J. T. *et al.* Overlapping and independent functions of fibronectin receptor integrins in early mesodermal development. *Developmental Biology* 215, 264-277 (1999).

104 Yang, J. T., Rayburn, H. & Hynes, R. O. Embryonic mesodermal defects in alpha 5 integrin-deficient mice. *Development* 119, 1093-1105 (1993).

105 Baneyx, G., Baugh, L. & Vogel, V. Fibronectin extension and unfolding within cell matrix fibrils controlled by cytoskeletal tension. *Proceedings of the National Academy of Sciences* 99, 5139-5143 (2002).

106 Baneyx, G., Baugh, L. & Vogel, V. Coexisting conformations of fibronectin in cell culture imaged using fluorescence resonance energy transfer. *Proceedings of the National Academy of Sciences* 98, 14464-14468 (2001).

107 Baneyx, G. & Vogel, V. Self-assembly of fibronectin into fibrillar networks underneath dipalmitoyl phosphatidylcholine monolayers: role of lipid matrix and tensile forces. *Proceedings of the National Academy of Sciences* 96, 12518-12523 (1999).

108 Halliday, N. L. & Tomasek, J. J. Mechanical properties of the extracellular matrix influence fibronectin fibril assembly in vitro. *Experimental cell research* 217, 109-117 (1995).

109 Zhong, C. *et al.* Rho-mediated contractility exposes a cryptic site in fibronectin and induces fibronectin matrix assembly. *The Journal of Cell Biology* 141, 539-551 (1998).

110 McKeown-Longo, P. J. & Mosher, D. F. Binding of plasma fibronectin to cell layers of human skin fibroblasts. *The Journal of Cell Biology* 97, 466-472 (1983).

111 Chen, H. & Mosher, D. F. Formation of Sodium Dodecyl Sulfate-stable Fibronectin Multimers: FAILURE TO DETECT PRODUCTS OF THIOL-DISULFIDE EXCHANGE IN CYANOGEN BROMIDE OR LIMITED ACID DIGESTS OF STABILIZED MATRIX FIBRONECTIN (*). *Journal of Biological Chemistry* 271, 9084-9089, doi:10.1074/jbc.271.15.9084 (1996).

112 Choi, M. & Hynes, R. Biosynthesis and processing of fibronectin in NIL. 8 hamster cells. *Journal of Biological Chemistry* 254, 12050-12055 (1979).

113 Sakai, K., Fujii, T. & Hayashi, T. Cell-free formation of disulfide-bonded multimer from isolated plasma fibronectin in the presence of a low concentration of SH reagent under a physiological condition. *Journal of biochemistry* 115, 415-421 (1994).

114 Mosher, D. & Johnson, R. In vitro formation of disulfide-bonded fibronectin multimers. *Journal of Biological Chemistry* 258, 6595-6601 (1983).

115 Ulmer, J., Geiger, B. & Spatz, J. P. Force-induced fibronectin fibrillogenesis in vitro. *Soft Matter* 4, 1998-2007 (2008).

116 Kaiser, P. & Spatz, J. P. Differential adhesion of fibroblast and neuroblastoma cells on size-and geometry-controlled nanofibrils of the extracellular matrix. *Soft Matter* 6, 113-119 (2010).

117 Ahmed, Z. & Brown, R. A. Adhesion, alignment, and migration of cultured Schwann cells on ultrathin fibronectin fibres. *Cell motility and the cytoskeleton* 42, 331-343 (1999).

118 Ejim, O. S., Blunn, G. W. & Brown, R. A. Production of artificial-orientated mats and strands from plasma fibronectin: a morphological study. *Biomaterials* 14, 743-748 (1993).

119 Klotzsch, E. *et al.* Fibronectin forms the most extensible biological fibers displaying switchable force-exposed cryptic binding sites. *Proceedings of the National Academy of Sciences* 106, 18267-18272 (2009).

120 Little, W. C., Smith, M. L., Ebneter, U. & Vogel, V. Assay to mechanically tune and optically probe fibrillar fibronectin conformations from fully relaxed to breakage. *Matrix Biology* 27, 451-461 (2008).

121 Salmerón-Sánchez, M. *et al.* Role of material-driven fibronectin fibrillogenesis in cell differentiation. *Biomaterials* 32, 2099-2105 (2011).

122 Nelea, V. & Kaartinen, M. T. Periodic beaded-filament assembly of fibronectin on negatively charged surface. *Journal of structural biology* 170, 50-59 (2010).

123 Feinberg, A. W. & Parker, K. K. Surface-Initiated Assembly of Protein Nanofabrics. *Nano Letters* 10, 2184-2191, doi:10.1021/nl100998p (2010).

124 Szymanski, J. M., Jallerat, Q. & Feinberg, A. W. ECM protein nanofibers and nanostructures engineered using surface-initiated assembly. *Journal of visualized experiments: JoVE* (2014).

125 Deravi, L. F. *et al.* Differential contributions of conformation extension and domain unfolding to properties of fibronectin nanotextiles. *Nano Letters* 12, 5587-5592 (2012).

126 Rief, M., Gautel, M. & Gaub, H. E. in *Elastic Filaments of the Cell* 129-141 (Springer, 2000).

127 Oberhauser, A. F., Badilla-Fernandez, C., Carrion-Vazquez, M. & Fernandez, J. M. The mechanical hierarchies of fibronectin observed with single-molecule AFM. *Journal of molecular biology* 319, 433-447 (2002).

128 Fisher, T. E., Oberhauser, A. F., Carrion-Vazquez, M., Marszalek, P. E. & Fernandez, J. M. The study of protein mechanics with the atomic force microscope. *Trends in biochemical sciences* 24, 379-384 (1999).

129 Pernodet, N. *et al.* Fibronectin fibrillogenesis on sulfonated polystyrene surfaces. *Journal of Biomedical Materials Research Part A* 64, 684-692 (2003).

130 Mnatsakanyan, H. *et al.* Controlled assembly of fibronectin nanofibrils triggered by random copolymer chemistry. *ACS applied materials & interfaces* (2015).

131 Rico, P. *et al.* Substrate-induced assembly of fibronectin into networks: influence of surface chemistry and effect on osteoblast adhesion. *Tissue Engineering Part A* 15, 3271-3281 (2009).

132 Erickson, H. P., Carrell, N. & McDONAGH, J. Fibronectin molecule visualized in electron microscopy: a long, thin, flexible strand. *The Journal of Cell Biology* 91, 673-678 (1981).

133 Erickson, H. P. & Carrell, N. Fibronectin in extended and compact conformations. Electron microscopy and sedimentation analysis. *Journal of Biological Chemistry* 258, 14539-14544 (1983).

134 Dzamba, B. J. & Peters, D. M. Arrangement of cellular fibronectin in noncollagenous fibrils in human fibroblast cultures. *Journal of Cell Science* 100, 605-612 (1991).

135 Ohashi, T., Kiehart, D. P. & Erickson, H. P. Dynamics and elasticity of the fibronectin matrix in living cell culture visualized by fibronectin–green fluorescent protein. *Proceedings of the National Academy of Sciences* 96, 2153-2158 (1999).

136 Smith, M. L. *et al.* Force-induced unfolding of fibronectin in the extracellular matrix of living cells. *PLoS Biol* 5, e268 (2007).

137 Wang, K. *et al.* Stiffening and unfolding of early deposited-fibronectin increase proangiogenic factor secretion by breast cancer-associated stromal cells. *Biomaterials* 54, 63-71 (2015).

138 Mouw, J. K., Ou, G. & Weaver, V. M. Extracellular matrix assembly: a multiscale deconstruction. *Nat Rev Mol Cell Biol* 15, 771-785, doi:10.1038/nrm3902 (2014).

139 Hynes, R. O. The Extracellular Matrix: Not Just Pretty Fibrils. *Science* 326, 1216-1219, doi:10.1126/science.1176009 (2009).

140 Grinnell, F., Billingham, R. E. & Burgess, L. Distribution of Fibronectin During Wound Healing in Vivo. *J Investig Dermatol* 76, 181-189 (1981).

141 Sabatier, L. *et al.* Fibrillin assembly requires fibronectin. *Molecular biology of the cell* 20, 846-858 (2009).

142 Schneider, C. A., Rasband, W. S. & Eliceiri, K. W. NIH Image to ImageJ: 25 years of image analysis. *Nat Methods* 9, 671-675 (2012).

143 Mosher, D. F. Assembly of fibronectin into extracellular matrix. *Current Opinion in Structural Biology* 3, 214-222, doi:http://dx.doi.org/10.1016/S0959-440X(05)80155-1 (1993).

144 Weber, K. & Osborn, M. The Reliability of Molecular Weight Determinations by Dodecyl Sulfate-Polyacrylamide Gel Electrophoresis. *Journal of Biological Chemistry* 244, 4406-4412 (1969).

145 Cleveland, D. W., Fischer, S. G., Kirschner, M. W. & Laemmli, U. K. Peptide mapping by limited proteolysis in sodium dodecyl sulfate and analysis by gel electrophoresis. *Journal of Biological Chemistry* 252, 1102-1106 (1977).

146 Uehara, N. & Ogawa, M. Interaction of Poly(N-isopropylacrylamide) with Sodium Dodecyl Sulfate below the Critical Aggregation Concentration. *Langmuir* 30, 6367-6372, doi:10.1021/la500900n (2014).

147 Zhu, P. W. Effects of Sodium Dodecyl Sulfate on Structures of Poly(N-isopropylacrylamide) at the Particle Surface. *The Journal of Physical Chemistry B* 119, 359-371, doi:10.1021/jp510350w (2015).

148 Schild, H. G. & Tirrell, D. A. Interaction of poly(N-isopropylacrylamide) with sodium n-alkyl sulfates in aqueous solution. *Langmuir* 7, 665-671, doi:10.1021/la00052a013 (1991).

149 Palchesko, R. N., Szymanski, J. M., Sahu, A. & Feinberg, A. W. Shrink Wrapping Cells in a Defined Extracellular Matrix to Modulate the Chemo-Mechanical Microenvironment. *Cellular and Molecular Bioengineering* 7, 355-368 (2014).

150 Dowling, N. E. *Mechanical behavior of materials: engineering methods for deformation, fracture, and fatigue*. (Prentice hall, 1993).

151 Hariton, I., Gasser, T. & Holzapfel, G. Stress-driven collagen fiber remodeling in arterial walls. *Biomechanics and modeling in mechanobiology* 6, 163-175 (2007).

152 Choi, A. & Zheng, Y. Estimation of Young's modulus and Poisson's ratio of soft tissue from indentation using two different-sized indentors: finite element analysis of the finite deformation effect. *Medical and Biological Engineering and Computing* 43, 258-264 (2005).

153 Zhang, M., Zheng, Y. & Mak, A. F. Estimating the effective Young's modulus of soft tissues from indentation tests—nonlinear finite element analysis of effects of friction and large deformation. *Medical engineering & physics* 19, 512-517 (1997).

154 Sacks, M. S. & Sun, W. Multiaxial Mechanical Behavior of Biological Materials. *Annual Review of Biomedical Engineering* 5, 251-284, doi:doi:10.1146/annurev.bioeng.5.011303.120714 (2003).

155 Brown, A. E. X., Litvinov, R. I., Discher, D. E., Purohit, P. K. & Weisel, J. W. Multiscale Mechanics of Fibrin Polymer: Gel Stretching with Protein Unfolding and Loss of Water. *Science (New York, N.Y.)* 325, 741-744, doi:10.1126/science.1172484 (2009).

156 Sjöberg, B., Eriksson, M., Österlund, E., Pap, S. & Österlund, K. Solution structure of human plasma fibronectin as a function of NaCl concentration determined by small-angle X-ray scattering. *European Biophysics Journal* 17, 5-11 (1989).

157 Langenbach, K. J. & Sottile, J. Identification of Protein-disulfide Isomerase Activity in Fibronectin. *Journal of Biological Chemistry* 274, 7032-7038, doi:10.1074/jbc.274.11.7032 (1999).

158 Barry, E. & Mosher, D. Factor XIIIa-mediated cross-linking of fibronectin in fibroblast cell layers. Cross-linking of cellular and plasma fibronectin and of amino-terminal fibronectin fragments. *Journal of Biological Chemistry* 264, 4179-4185 (1989).

159 Mitsi, M. *et al.* The ultrastructure of fibronectin fibers pulled from a protein monolayer at the air-liquid interface and the mechanism of the sheet-to-fiber transition. *Biomaterials* 36, 66-79, doi:http://dx.doi.org/10.1016/j.biomaterials.2014.08.012 (2015).

160 Fruh, S. M., Schoen, I., Ries, J. & Vogel, V. Molecular architecture of native fibronectin fibrils. *Nat Commun* 6, doi:10.1038/ncomms8275 (2015).

161 Sun, Y., Jallerat, Q., Szymanski, J. M. & Feinberg, A. W. Conformal nanopatterning of extracellular matrix proteins onto topographically complex surfaces. *Nature methods* 12, 134-136 (2015).

162 Netti, P. A., Berk, D. A., Swartz, M. A., Grodzinsky, A. J. & Jain, R. K. Role of extracellular matrix assembly in interstitial transport in solid tumors. *Cancer research* 60, 2497-2503 (2000).

163 Daley, W. P. & Yamada, K. M. in *Extracellular Matrix in Development* 75-104 (Springer Berlin Heidelberg, 2013).

164 Yamada, K. M. & Olden, K. Fibronectins—adhesive glycoproteins of cell surface and blood. (1978).

165 Toworfe, G. K., Composto, R. J., Adams, C. S., Shapiro, I. M. & Ducheyne, P. Fibronectin adsorption on surface-activated poly (dimethylsiloxane) and its effect on cellular function. *Journal of Biomedical Materials Research Part A* 71, 449-461 (2004).

166 Burdick, J. A. & Anseth, K. S. Photoencapsulation of osteoblasts in injectable RGD-modified PEG hydrogels for bone tissue engineering. *Biomaterials* 23, 4315-4323 (2002).

167 Shin, H., Jo, S. & Mikos, A. G. Biomimetic materials for tissue engineering. *Biomaterials* 24, 4353-4364 (2003).

168 Barker, T. H. The role of ECM proteins and protein fragments in guiding cell behavior in regenerative medicine. *Biomaterials* 32, 4211-4214, doi:http://dx.doi.org/10.1016/j.biomaterials.2011.02.027 (2011).

169 Brown, A. C., Rowe, J. A. & Barker, T. H. Guiding epithelial cell phenotypes with engineered integrin-specific recombinant fibronectin fragments. *Tissue Engineering Part A* 17, 139-150 (2010).

170 Sun, Y., Duffy, R., Lee, A. & Feinberg, A. W. Optimizing the structure and contractility of engineered skeletal muscle thin films. *Acta Biomaterialia* 9, 7885-7894, doi:http://dx.doi.org/10.1016/j.actbio.2013.04.036 (2013).

171 Markowski, M. C., Brown, A. C. & Barker, T. H. Directing epithelial to mesenchymal transition through engineered microenvironments displaying orthogonal adhesive and mechanical cues. *Journal of Biomedical Materials Research Part A* 100, 2119-2127 (2012).

172 Palchesko, R. N., Zhang, L., Sun, Y. & Feinberg, A. W. Development of Polydimethylsiloxane Substrates with Tunable Elastic Modulus to Study Cell Mechanobiology in Muscle and Nerve. *PLoS ONE* 7, 1-13 (2012).

173 Palchesko, R. N., Zhang, L., Sun, Y. & Feinberg, A. W. Development of Polydimethylsiloxane Substrates with Tunable Elastic Modulus to Study Cell Mechanobiology in Muscle and Nerve. *PLoS ONE* 7, e51499, doi:10.1371/journal.pone.0051499 (2012).

174 Wang, K., Seo, B. R., Fischbach, C. & Gourdon, D. Fibronectin Mechanobiology Regulates Tumorigenesis. *Cellular and Molecular Bioengineering*, 1-11 (2015).

175 Ma, Z. *et al.* Self-organizing human cardiac microchambers mediated by geometric confinement. *Nat Commun* 6, doi:10.1038/ncomms8413 (2015).

176 Rust, M. J., Bates, M. & Zhuang, X. Sub-diffraction-limit imaging by stochastic optical reconstruction microscopy (STORM). *Nat Meth* 3, 793-796, doi:http://www.nature.com/nmeth/journal/v3/n10/suppinfo/nmeth929_S1.html (2006).

177 Betzig, E. *et al.* Imaging intracellular fluorescent proteins at nanometer resolution. *Science* 313, 1642-1645 (2006).

178 Bates, M., Huang, B., Dempsey, G. T. & Zhuang, X. Multicolor super-resolution imaging with photo-switchable fluorescent probes. *Science* 317, 1749-1753 (2007).

179 Xu, K., Zhong, G. & Zhuang, X. Actin, Spectrin, and Associated Proteins Form a Periodic Cytoskeletal Structure in Axons. *Science* 339, 452-456, doi:10.1126/science.1232251 (2013).

180 Kanchanawong, P. *et al.* Nanoscale architecture of integrin-based cell adhesions. *Nature* 468, 580-584, doi:http://www.nature.com/nature/journal/v468/n7323/abs/nature09621.html#supplementary-information (2010).

181 Szymborska, A. *et al.* Nuclear pore scaffold structure analyzed by super-resolution microscopy and particle averaging. *Science* 341, 655-658 (2013).

182 Klotzsch, E. *et al*. Conformational distribution of surface-adsorbed fibronectin molecules explored by single molecule localization microscopy. *Biomaterials Science* 2, 883-892 (2014).

183 Dempsey, G. T., Vaughan, J. C., Chen, K. H., Bates, M. & Zhuang, X. Evaluation of fluorophores for optimal performance in localization-based super-resolution imaging. *Nature methods* 8, 1027-1036 (2011).

184 Schneider, C. A., Rasband, W. S. & Eliceiri, K. W. NIH Image to ImageJ: 25 years of image analysis. *Nature methods* 9, 671-675 (2012).

APPENDIX:

Dual Modality Investigation of the Fibronectin Nanostructure Using Stochastic Optical Reconstruction Microscopy and Atomic Force Microscopy

A.1. Introduction

The development of super resolution imaging approaches[176-178], has allowed researchers to investigate biological materials at scales that are well below the spatial resolution limits of light microscopy techniques. In addition to using super resolution microscopy to study actin networks[177,179], focal adhesions[180], and nuclear pores[181], these imaging techniques have also recently been used to investigate the conformations of surface-adsorbed[182] and cell-generated FN fibers[160]. These studies have enabled researchers to understand how FN may adopt different conformations when adsorbing onto surfaces with different hydrophobicity as well as how FN dimers may be arranged into larger FN fibers.

One of the recently developed super-resolution techniques, termed stochastic optical reconstruction microscopy (STORM), involves the use of photoswitchable fluorophores to sequentially image and localize individual fluorophores to achieve a lateral resolution of 20 nm[176,178,183]. In STORM imaging, a high intensity laser is first used to send the fluorophores into a dark state. Over time, a small number fluorophores will spontaneously return from the dark state and fluorescence before being sent back to the dark state, creating a "blinking" phenomenon. High precision Gaussian fitting of each blink allows the XY position of the fluorophore to be mapped and, after acquiring a series of images, an image can be created with resolution below the diffraction limit of light can be created.

One of the most important aspects of STORM imaging is the fluorophore selection. There are several key parameters that must be considered (see the review by Dempsey GT et al, *Nature Methods*, 2011) especially if multiple fluorophores are to be used. Briefly, the two major properties to consider are the number of photons per switching event and the on-off duty cycle (fraction of time spent in the 'on' state). In general, a high number of photons per switching event and a low on-off duty cycle are desirable for precise localization of the fluorophores. Table A.1., adapted from Dempsey et al, compares these important properties for 26 commonly used fluorophores in two different STORM imaging buffers[183].

Super-resolution microscopy techniques have only been applied to FN in discrete states when adsorbed onto different material surfaces and at specific time points during cell culture. Therefore we

wanted to use STORM microscopy on FN nanofibers prepared using SIA to determine how strain affects the separation of the four cysteine amino acid residues found in the FN III_7 and FN III_{15} domains (two per each FN monomer). Additionally, by correlating STORM images with AFM topographical images, we wanted to determine whether morphological features observed in the AFM images correlate to FN with more unfolded or contracted conformations. This appendix section will introduce the working protocol to use STORM in combination with atomic force microscopy (AFM) on FN nanofibers prepared using surface-initiated assembly (SIA) as well as highlight some preliminary results.

A.2. Materials and Methods

A.2.1. FN Nanofiber Fabrication

FN nanofibers were prepared by slight modification of methods discussed previously (Chapters 2 and 3). First, poly(dimethylsiloxane) (PDMS) stamps patterned with 1 cm long and 50 μm wide, raised rectangles were fabricated by first spincoating glass wafers with SPR 220.3 positive photoresist (Microchem). The photoresist was then exposed to UV light through a photomask and developed using MF-319 developer (Microchem). A negative of the patterned photoresist wafer was formed by casting PDMS prepolymer (Sylgard 184, Dow Corning) over it and curing it in an oven at 65° C for 4 hours. The cured PDMS was then peeled off the glass wafer and 1 cm^2 stamps were cut out.

For experiments involving strained FN nanofibers and STORM imaging, there were two critical components. The first was to conjugate a small percentage (10%) of the FN to Alexa Fluor 647 fluorophores (Life Technologies) and the second was to tag the nanofibers with fluorescent, FN-based fiduciary marks. Therefore, to prepare FN nanofibers that contained Alexa Fluor 647-conjugated FN with Alexa Fluor 488-conjugated fiduciary marks, PDMS stamps with 10 μm wide, 1 cm long raised features were first cleaned by sonication in a 50% ethanol solution for 30 minutes. Following sonication, the stamps were dried under a stream of nitrogen and then incubated with FN from human plasma (BD Biosciences) for 60 minutes at a concentration of 50 μg/mL in distilled water. 40% of the FN was conjugated to an Alexa Fluor 488 dye (Life Technologies) following manufacturer's instructions. The Alexa 488 was used because there is little spectral overlap with the Alexa Fluor 647 dye. After incubation, the stamps were washed, dried under a stream of nitrogen and then brought into conformal contact with poly(N-isopropylacrylamide) (PIPAAm) coated coverslips for 15 minutes (Fig. 3.1a). The PIPAAm coated coverslips were prepared by spincoating a 10% PIPAAm (Polysciences Inc.) in 1-butanol (w/v) solution. Upon removal of the stamps, the fidelity of the transfer of the 10 μm wide FN lines to the PIPAAm coated coverslips was inspected using phase contrast microscopy.

Following microcontact printing, a second PDMS stamp with 50 μm wide and 1 cm long raised features was coated with a 50 μg/mL solution of FN dissolved in distilled water (Fig. 3.1b). This solution contained a small percentage (10%) of FN that was conjugated to Alexa Fluor 647 fluorophores. The stamp was then washed to remove excess FN, dried under a stream of nitrogen and subsequently brought into conformal contact orthogonal to the PIPAAm coated coverslip containing the 10 μm wide FN lines (Fig. 3.1c). With the stamp still in conformal contact, the PIPAAm was hydrated with warm, 40° C, distilled water and allowed to cool below the LCST of PIPAAm thereby releasing the fluorescently labeled, 10 μm wide FN lines off of the PIPAAm onto the PDMS stamp which was pre coated with FN. The stamp was then removed, washed in distilled water, dried under a stream of nitrogen and then brought into conformal contact with a new PIPAAm coated coverslip for 10 minutes to create arrays of 1 cm x 50 μm Alexa Fluor 647-conjugated FN lines with 10 μm wide and 10 μm spaced fiduciary marks that were conjugated with Alexa Fluor 488 fluorophores (Fig. 3.1d). It is important to note that the PIPAAm-coated coverslips in this final step must be prepared using #1.5 coverslips, instead of the normal #1.0 coverslips. The N-STORM microscope has been optimized for coverslips with a thickness of 0.17 mm, which is also the thickness of the #1.5 coverslips.

A.2.2. Fibronectin Nanofiber Straining Experiments

To strain FN nanofibers, we first microcontact printed 1 cm long and 50 μm wide lines of Alexa Fluor 647-conugated FN that was also tagged with fiduciary marks as described above. Next, we prepared PDMS pads by casting PDMS prepolymer over a glass slide and curing it in an oven set to 65° C for 4 hours. Once cured we cut out 2 PDMS rectangles that were ~1 cm long and ~5 mm wide and placed them at opposite ends on top of the FN nanofibers on PIPAAm. We then attached the PDMS pads to a pair of micromanipulators by applying a small drop of high strength epoxy (Devcon) to the top of the pads, bringing the manipulator tips in contact with the epoxy, and allowing the epoxy to harden for at least 30 minutes (Fig. 3.2a). Once dry, we triggered the thermal dissolution of PIPAAm by hydration and

subsequent cooling below the LCST of PIPAAm which led to the assembly and release of the nanofibers off of the PIPAAm and onto the PDMS pads. This resulted in FN fibers that were tethered at each end to a PDMS pad and freely suspended in between. The FN nanofibers were strained by moving the micromanipulators in opposite directions (Fig. 3.2.b) and subsequently immobilized back onto the coverslip once a given strain was reached. To calculate strain, we used the center-to-center fiduciary mark distance of a released and fully contracted FN nanofiber as the initial length and the center-to-center fiduciary mark distance of the strained FN nanofibers as the final length. Strain experiments were performed on top of an inverted epifluorescent microscope (Eclipse Ti, Nikon Instruments) with mounted micromanipulators (Transferman NK2, Eppendorf).

A.2.3. Engineering Custom Petri Dishes for STORM Imaging

The microscope objective used for STORM imaging has a limited working distance (~12 μm). Therefore custom petri dishes were made to allow the microscope objective to image solely through the glass coverslip containing the immobilized FN nanofibers while also permitting the use of a STORM imaging buffer solution (Fig. A.1). First, a hole was created in the bottom of 35 mm petri dishes using a drill press. An alternate technique is to heat up a quarter and place it on the bottom of the petri dish. The hot quarter will eventually melt through the petri dish creating a quarter-sized hole. Once a hole has been created, the glass coverslip containing the immobilized FN nanofibers can be placed over the hole in the bottom of the petri dish such that the feature side of the coverslip faces towards the lid of the petri dish. Finally, a seal is created by dabbing a small amount of PDMS prepolymer around the edges of the coverslip and then allowing the PDMS to cure overnight at 37° C. After STORM imaging, the coverslip can be removed from the petri dish by carefully cutting the PDMS seal with a razor.

A.2.3. Preparation of STORM Imaging Buffer

The STORM imaging buffer was prepared by combining GLOX, MEA, and Buffer B solutions. The solutions were prepared as following (per instructions from Nikon):

1. **Buffer A**: 10 mM Tris (pH 8.0) + 50 mM NaCl
2. **Buffer B**: 50 mM Tris (pH 8.0) + 10 mM NaCl + 10% (w/v) Glucose
3. **GLOX solution (250 µL)**: 14 mg Glucose Oxidase from Aspergillus Niger (≥ 10.000 units/g solid, Sigma, catalog # G2133-250KU) + 50 µL Catalase at a concentration of 17 mg/mL (from bovine liver, ≥ 10,000 units/mg protein, Sigma, catalog #C40-100MG) + 200 µL Buffer A. Vortex to dissolve glucose oxidase. Spin down at 14,000 rpm. Use only supernatant and store at 4° C for up to 2 weeks.
4. **1M MEA (1 mL)**: 77 mg Cysteamine (Sigma, catalog #30070-50G) + 1.0 mL 0.25 N HCl. Store at 4° C for up to 1 month.

Prior to STORM imaging, the imaging buffer was prepared by adding 7 µL GLOX and 70 µL 1M MEA solutions to 620 µL Buffer B in a 1.5 mL Eppendorf tube. The solution was vortexed to gently mix the different components. Once mixed, the imaging buffer is effective for up to several hours before needing to be replaced. Thus, if imaging experiments last longer than several hours, new solution is made by mixing more of the stock GLOX, MEA, and Buffer B solutions.

A.2.4. Imaging FN Nanofibers Using STORM

STORM imaging was performed on an N-STORM Super-Resolution Microscope System (Nikon) with a 100x (NA = 1.49) oil immersion objective. For STORM experiments, 45,000 images were acquired at a frame rate of 100 fps using an iXon Ultra 897 EM-CCD camera (Andor). A complete workflow for STORM imaging will be discussed in the following section.

A.2.5. Imaging FN Nanofibers Using AFM

Following STORM imaging, the coverslips were rinsed three times in distilled water and then dried in an oven set to 37° C. Once dried, the coverslip was removed from the petri dish by *carefully* cutting the PDMS seal with a razor blade. Once removed from the petri dishes, the coverslips were loaded onto the stage of the AFM (MFP3D-Bio, Asylum Research) and the same FN nanofibers that were imaged using STORM were scanned using AFM.

To FN nanofibers were scanned in air using AC mode with AC160TS-R3 cantilevers (Olympus Corporation). Low resolution scans were first obtained to confirm that each nanofiber corresponded to one that was imaged using STORM. The low resolution images had a scan size of ~40 μm x 40 μm with a points and lines of 1024 x 1024. Once it was confirmed that a given low resolution image correlated with a STORM image, high resolution AFM scans were obtained. The high resolution AFM scans were obtained of key landmark features. The high resolution scans typically had a scan size of 10 μm x 10 μm with a points and lines of 2048 x 2048.

A.2.6. Overlaying AFM and STORM Images

To overlay AFM and STORM images, correlating AFM and STORM images were first loaded into imageJ[184]. The images were resized, rotated, and in some cases, cropped to ensure that both images had the same scale and were oriented correctly. They were then exported in Adobe Illustrator (Adobe Systems) where the STORM image was made semi-transparent and then subsequently overlaid onto the AFM image. Using distinguishable features as a guide, the STORM image was moved relative to the AFM image until a reasonable overlay was achieved.

A.2.7. Nikon N-STORM Imaging Workflow

The Nikon N-STORM in located in the lab of Prof. Ge Yang (Mellon Institute, Room 280) and he should be contacted directly to discuss training for new users. While the protocol described below

provides an introductory guide, new users will be required to become trained by one of the super-users of the system. It is important to note that the N-STORM operates very similarly to the Nikon Eclipse in the Feinberg lab which should quicken the total training time. Additionally, there is a lot of overlap in terms of microscope operation and use of the Nikon Elements software environment.

I. Starting the N-Storm System

1. Turn on the 3 switches on the top shelf to the left of the microscope. Specifically, the switches located on the box entitled "Lambda 10-3," the Nikon Box to the right of the Lambda Box, and the switch behind the large laser box.
2. Turn on the microscope. The switch is located on the right hand side of the microscope at the base.
3. Turn the laser key to and then press the 4 buttons corresponding to each laser line.
4. In the left port of the microscope, confirm that the "3D-STORM" filter is out (unless 3D-STORM will be used). Additionally, make sure the STORM filter is "in."
5. Confirm that all of the ND filters are in the "out" position except for the λ/4 filter.
6. If it is desirable to use regular widefield fluorescence, turn on the X-Cite fluorescence excitation source.
7. Launch the Nikon Elements Acquisition software and select the option "Andor w/N-STORM."

II. Beam Focusing and Sample Loading

1. Hit the "Beam Focus" button in the Nikon Elements software. Gently move the condenser of the microscope backwards and observe the laser spot on the ceiling.
2. On the left of the microscope, there are two knobs. Turn the left, silver knob counterclockwise to loosen it. Slide the other knob left and right until the laser spot on

the ceiling becomes a fine point. Once this happens, rotate the left knob clockwise to tighten it.

3. Make sure the objective is in its lowest position then add a drop of immersion oil to the objective.
4. Load the sample onto the stage. Hit the "PFS" button on the base of the microscope to activate the perfect focus. Slowly bring the objective up until the oil contacts the coverslip and then continue to slowly raise the objective until the PFS recognizes the coverslip (it will beep). Note: Once PFS is activated, you must use the focus wheel on the PFS box as the one on the microscope base becomes deactivated.
5. Prepare the STORM imaging buffer as described above. Briefly, add 7 μL GLOX and 70 μL MEA solutions to 620 μL Buffer B. Vortex the solutions and then pipette the imaging buffer onto the sample mounted on the microscope stage.
6. Put the lid on the petri dish and use the clamps on the microscope stage to hold the dish in place.

III. STORM Imaging

1. Find a region of interest. To do this, turn the 647 laser power to 1% and hit the "STORM" button. Using the joystick, move the sample around adjusting the focus on the PFS box if necessary.
2. Once a region of interest has been identified, the TIRF angle needs to be adjusted. In the TIRF panel, adjust the slider until the signal of the image is brightest.
3. Set the image name, folder to save in, and the number of frames (should typically be anywhere between 30,000 and 60,000).
4. Turn the laser power to 100% to send the fluorophores to the dark state.
5. Hit the "Run Now" button.

6. After STORM imaging, analysis can be run following the protocol on the desktop of the N-STOM computer.

A.3. Representative Results

Since there is a limited working distance for the 100x objective on the N-STORM microscope (~12 μm), custom petri dishes were first created to ensure that the immobilized FN nanofibers could be imaged on the N-STORM system (Fig. A.1). This was accomplished by first drilling a hole in the bottom of a 35 mm petri dish using a drill press. On the bottom of the petri dish, a small amount of PDMS prepolymer was dabbed around the created hole and a coverslip containing immbolized FN nanofibers

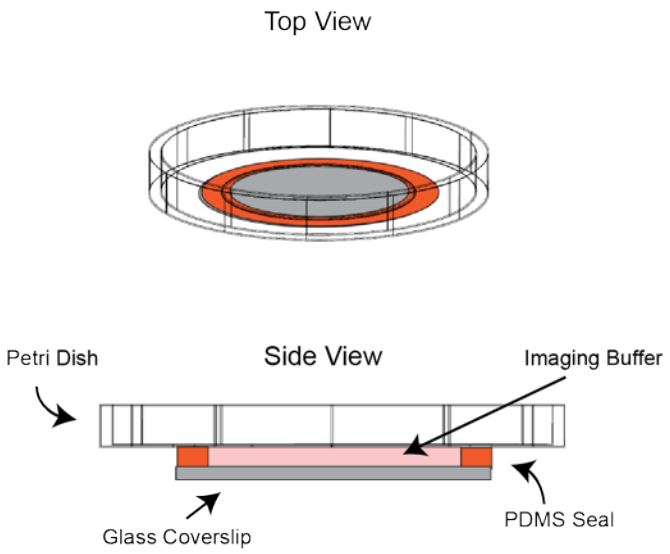

Fig. A.1. Preparation of glass bottom petri dishes for STORM imaging. A drill press was used to drill a hole in the bottom of 35 mm petri dishes. A glass coverslip containing immobilized FN nanofibers was placed over the hole and sealed with PDMS. Following STORM imaging, the coverslip could be removed by cutting away the PDMS seal.

was placed over the hole and in contact with the PDMS. The PDMS was allowed to cure in a 37° C oven overnight resulting in a tight seal.

Next, FN nanofibers were strained as discussed in Chapter 3 and immobilized onto #1.5 glass coverslips. These FN nanofibers had a small amount (10%) that was labeled with an Alexa Fluor 647 fluorophore. The Alexa Fluor 647 fluorophore was chosen because it has a high number of photons per

Dye	Excitation maximum (nm)[a]	Emission maximum (nm)[a]	Extinction (M^{-1} cm^{-1})[b]	Quantum yield[c]	Detected photons per switching event		Equilibrium on-off duty cycle (400–600 s)		Survival fraction after illumination for 400 s		Number of switching cycles (mean)	
					MEA	βME	MEA	βME	MEA	βME	MEA	βME
Blue-absorbing												
Atto 488	501	523	90,000	0.8	1,341	1,110	0.00065	0.0022	0.98	0.99	11	49
Alexa Fluor 488	495	519	71,000	0.92	1,193	427	0.00055	0.0017	0.94	1	16	139
Atto 520	516	538	110,000	0.9	1,231	868	0.0015	0.00061	0.92	0.86	9	17
Fluorescein	494	518	70,000	0.79	1,493	776	0.00032	0.00034	0.51	0.83	4	15
FITC	494	518	70,000	0.8	639	1,086	0.00041	0.00031	0.75	0.9	17	16
Cy2	489	506	150,000	0.12	6,241	4,583	0.00012	0.00045	0.12	0.19	0.4	0.7
Yellow-absorbing												
Cy3B	559	570	130,000	0.67	1,365	2,057	0.0003	0.0004	1	0.89	8	5
Alexa Fluor 568	578	603	91,300	0.69	2,826	1,686	0.00058	0.0027	0.58	0.99	7	52
TAMRA	546	575	90,430	0.2	4,884	2,025	0.0017	0.0049	0.85	0.99	10	59
Cy3	550	570	150,000	0.15	11,022	8,158	0.0001	0.0003	0.17	0.55	0.5	1.6
Cy3.5	581	596	150,000	0.15	4,968	8,028	0.0017	0.0005	0.89	0.61	5.7	3.3
Atto 565	563	592	120,000	0.9	19,714	13,294	0.00058	0.00037	0.17	0.26	4	5
Red-absorbing												
Alexa Fluor 647	650	665	239,000	0.33	3,823	5,202	0.0005	0.0012	0.83	0.73	14	26
Cy5	649	670	250,000	0.28	4,254	5,873	0.0004	0.0007	0.75	0.83	10	17
Atto 647	645	669	120,000	0.2	1,526	944	0.0021	0.0016	0.46	0.84	10	24
Atto 647N	644	669	150,000	0.65	3,254	4,433	0.0012	0.0035	0.24	0.65	9	39
Dyomics 654	654	675	220,000	–	3,653	3,014	0.0011	0.0018	0.79	0.64	20	19
Atto 655	663	684	125,000	0.3	1,105	657	0.0006	0.0011	0.65	0.78	17	22
Atto 680	680	700	125,000	0.3	1,656	987	0.0019	0.0024	0.65	0.91	8	27
Cy5.5	675	694	250,000	0.28	5,831	6,337	0.0069	0.0073	0.87	0.85	16	25
NIR-absorbing												
DyLight 750	752	778	220,000	–	712	749	0.0006	0.0002	0.55	0.58	5	6
Cy7	747	776	200,000	0.28	852	997	0.0003	0.0004	0.48	0.49	5	2.6
Alexa Fluor 750	749	775	240,000	0.12	437	703	0.00006	0.0001	0.36	0.68	1.5	6
Atto 740	740	764	120,000	0.1	779	463	0.00047	0.0014	0.31	0.96	3	14
Alexa Fluor 790	785	810	260,000	–	591	740	0.00049	0.0014	0.54	0.62	5	2.7
IRDye 800 CW	778	794	240,000	–	2,753	2,540	0.0018	0.038	0.6	1	3	127

Excitation wavelength, dichroic mirrors and emission filters used for characterization and imaging for each spectral range were 488 nm, T495LP (Chroma) and ET535/50m (Chroma) for blue-absorbing dyes; 561 nm, Di01-R561 (Semrock) and FF01-617/73-25 (Semrock) for yellow-absorbing dyes; 647 nm, Z660DCXRU (Chroma) and ET700/75m (Chroma) for red-absorbing dyes; 752 nm, Q770DCXR (Chroma) and HQ800/60m (Chroma) for NIR-absorbing dyes, respectively. Dye-switching properties are reported in the presence of GLOX and 10 mM MEA as well as GLOX and 140 mM βME.
[a]Excitation and emission peak wavelengths from dye spectra. [b]Extinction coefficients from the dye manufacturers. [c]Quantum yields from either the dye manufacturer when known or from the McNamara 2007 fluorophore data tables. –, quantum yield values not available from dye manufacturer or McNamara data tables.

Table A.1. Summary of key fluorophore properties for 26 different commonly used fluorophores. The key properties to consider when selecting a fluorophore for STORM imaging are the photons per switching event and on-off duty cycle in the imaging buffer used (MEA is used in the study discussed here). Other properties such as survival fraction after illumination and number of switching cycles should be considered as well but a slightly less critical than the formerly discussed properties. Adapted from Dempsey GT et al, 2011[183].

switching event and a low on-off duty cycle (Table A.1.), two key parameters for STORM imaging and the precise localization of the fluorophores[183]. The following AFM and STORM images are from the same FN nanofiber that was strained to 377%. First, to confirm that the FN nanofiber imaged using STORM and then on the AFM was the same fiber, we compared the morphology of the fiduciary mark in both images (Fig. A.2a and b). Often, with the application of strain, the fiduciary marks typically adopt

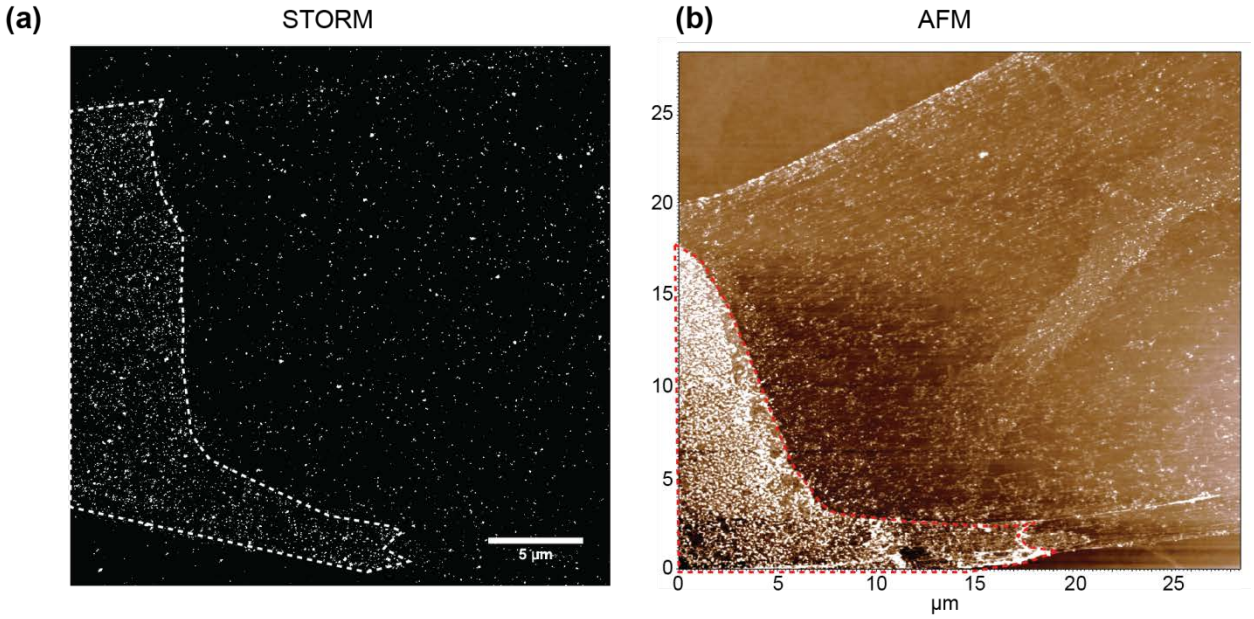

Fig. A.2. Comparing the morphology of the fiduciary mark to confirm the same FN nanofiber was imaged with both modalities. A low resolution (a) STORM image and (b) AFM image. The morphology of the fiduciary mark, where there is a long point at the bottom of the nanofiber, confirms that the same FN nanofiber was imaged for each modality. Scale bar for (a) is 5 µm.

unique and recognizable conformations that can be used to identify a specific FN nanofiber. In Fig. A.2, The fiduciary mark has a narrow point on the bottom of the FN nanofiber suggesting that the STORM and AFM images correspond to the same FN nanofiber.

Once we confirmed that the FN nanofiber from the AFM and STORM images was the same, we attempted to overlay the two channels. This was accomplished by first aligning the fiduciary mark of each region (Fig. A.3a-c). Once there was a general alignment between the two overlaid images, it was possible to first identify small regions that had distinguishable features and then to sequentially increase the resolution of the STORM and AFM images from ~30 µm x 30 µm to 10 µm x 10 µm (Fig. A.4). At this resolution, it was possible to observe patterns within the nanostructure of the FN nanofibers in the AFM images. Particular attention was placed on linear FN strands in the AFM images as they were comprised of nodules that routinely decreased in size. They also formed segments that would obtain a smooth morphology instead of a nodular one which might indicate the FN molecules have at least partially unfolded. When overlaying the STORM image, we first focused on overlaying key landmark

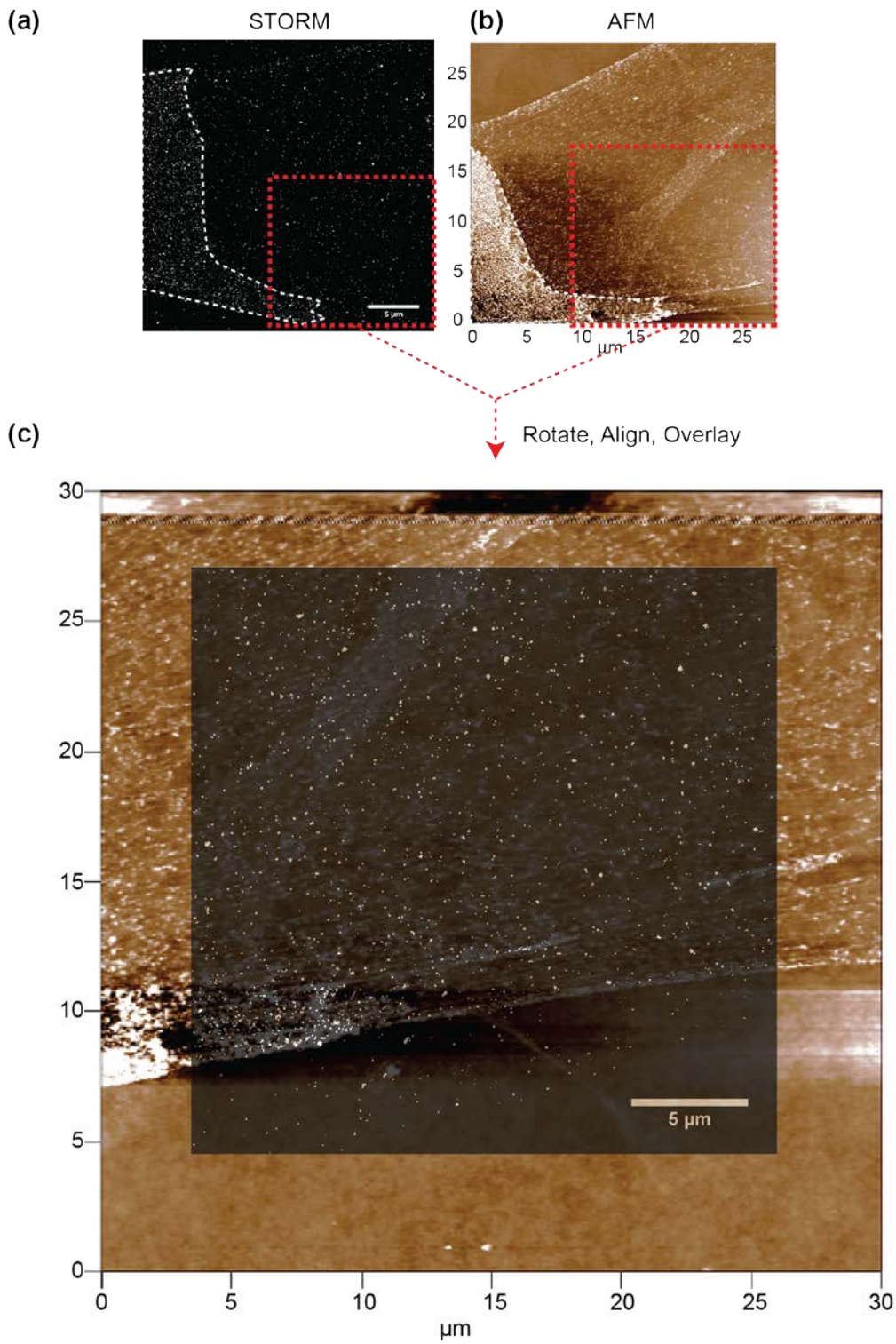

Fig. A.3. Overlaying STORM and AFM images at low resolution. A correlating (a) STORM and (b) AFM image were (c) overlaid using the morphology of the fiduciary mark as a guide. The STORM image had to first be rotated and shifted to enable good agreement between the two images. Scale bar in (a) is 5 µm.

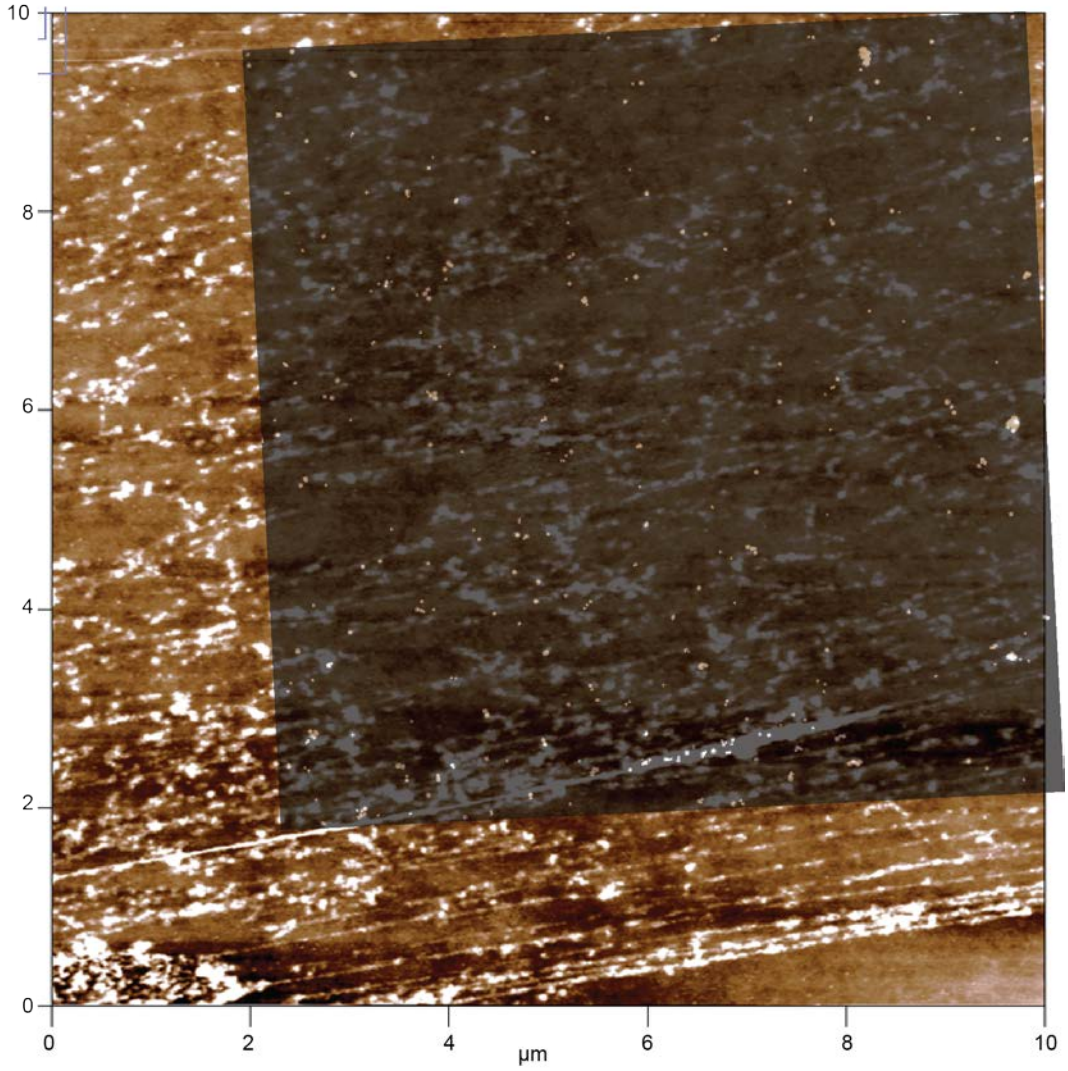

Fig. A.4. Overlaid AFM and STORM images at increased resolution. The scan size of the AFM image was decreased to 10 µm x 10 µm. At this scale, it is possible to identify key features within the nanostructure of the FN nanofiber. These features enable the STORM image to be overlaid with high precision.

features, such as linear, dense collection of fluorophores in the STORM image with the thick, linear bundle in the AFM image.

Once there was a general agreement between these key landmark features, we then examined the overlaid STORM image to see if there were collections of fluorophores that corresponded to regions of the FN fibrils that may be unfolded based on the AFM height signal.

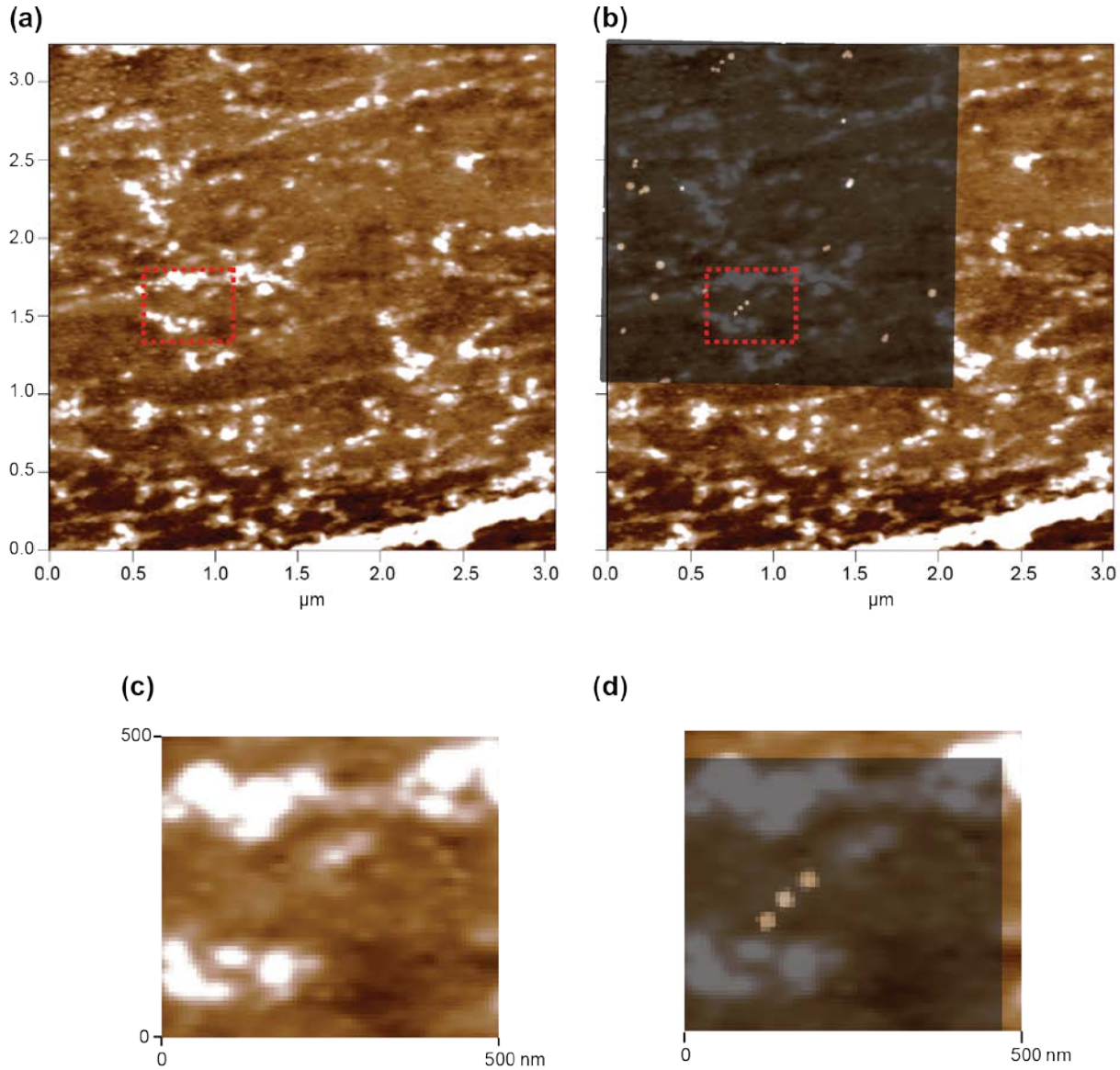

Fig. A.5. High resolution AFM and STORM image correlation. The resolution of the AFM images was further increased by decreasing the scan area to (a) A 3 µm x 3 µm. Using key features in the AFM image and the lower resolution STORM images as a guide, (b) a high resolution STORM image was overlaid onto the AFM image. Following an optical of the highlighted regions in (a) and (b) shows region between two nodules in the (c) AFM image. When the (d) STORM image is overlaid, it is clear that at linear arrangement of fluorophores runs in between the two nodules suggesting the presence of a FN dimer with an approximate end-to-end distance of 117 nm.

We identified one region and further increased the resolution of both the AFM and STORM images down to ~3 µm x 3 µm (Fig. A.5a and b). The images were optically zoomed to highlight a 500 nm x 500 nm region illustrating a linear arrangement of 3 fluorophores the correlate to a small segment between two nodules (Fig. A5 c and d). the end-to-end distance of the fluorophores was 117 nm, approximately the

length of a single FN dimer in an unfolded state without the loss of secondary structure[132,133]. It is uncertain if there was potentially further unfolding of the FN dimer because the fourth available cysteine residue was either not conjugated to a fluorophore, the fluorophore failed to appropriately 'blink,' or two fluorophores were within the 20 nm resolution limit of STORM. Further work is needed to systematically measure the end-to-end distances of arrangements of fluorophores that span between nodules in the AFM image. This will allow us to determine whether the FN dimers are unfolding beyond a contour length of 120-150 nm, which is the approximate length of a single unfolded FN dimer without the loss of any secondary protein structure.

In summary, the FN nanofiber straining approach discussed in Chapter 3 can be modified to support STORM super-resolution imaging. Only a small fraction of FN was labeled with an Alexa Fluor 647 fluorophore to increase the certainty that a cluster of fluorophores correlated to the same FN dimer. Further, while the use of fiduciary marks provide an accurate measurement of FN nanofiber strain, because each fiduciary mark also serves as a mechanism to begin aligning correlating AFM and STORM images. By sequentially increasing the resolution of both the STORM and AFM images, based on key landmark features, we were able to assign a linear arrangement of fluorophores to a segment between two nodules that is barely perceivable using AFM. Based on the end-to-end distance of the fluorophores, we can conclude that the FN dimer is at least in an unfolded state without the loss of secondary structure. This work provides a methodology and preliminary data that AFM and STORM super-resolution microscopy can be used in tandem to further elucidate how FN dimers, assembled within a fiber, respond to applied forces. Future work using this multi-modality approach will provide new insight into the development of mechanistic models of FN mechanobiology.